

Performance of a Single-Aisle Aircraft with Auxiliary Propulsion and Power Unit

Klaas Burger

March 22, 2022

This page is intentionally left blank

Performance of a Single-Aisle Aircraft with Auxiliary Propulsion and Power Unit

by

Klaas Burger

March 22, 2022

Master of Science Thesis Aerospace Engineering
Delft University of Technology

Student number:	4471245		
Project duration:	April 13, 2021 – March 31, 2022		
Supervisor:	Dr. ir. R. (Roelof) Vos		
Committee:	Dr. ir. R. (Roelof) Vos	Chair	
	Dr. ir. A. (Arvind) Gangoli Rao	Examiner	
	F. (Feijia) Yin PhD	Examiner	

Final version

A digital version is available from `repository.tudelft.nl`

Cover image source: J. Woroniecki. Airplane Above the Clouds Travel. 2020. URL
<https://pixabay.com/photos/airplane-above-the-clouds-travel-5298452/>, accessed
23-06-2021.

Preface

This MSc. Thesis marks the end of a six-and-a-half year period of studying at TU Delft. A period in which I have completed both my Bachelor and with this thesis my Master degree in aerospace engineering. It has been an amazing, exciting and challenging time in which I have learned more than I could ever have hoped for. Besides studying I have also been able to develop myself and learn a lot about the industry. I am excited to start my career as an aerospace engineer in one month time.

I would like to thank all the TU Delft who have helped me throughout the years. In particular, I would also like to thank my thesis supervisor Dr. ir. Roelof Vos for his help and input during my thesis, and APPU researcher Dr. ing. Alexander Heidebrecht for his help and the many interesting discussions on A321appu. Furthermore, I want to thank my thesis committee members Dr. ir. Arvind Gangoli Rao and Feijia Yin PhD for critically examining my work. Finally, I would like to thank my friends, family and my girlfriend for their support during my thesis work, and for the hours they have spent proofreading my work.

I wish the best of luck to those continuing on the APPU-project!

Klaas Burger
14th of March 2022, Delft

Summary

The aviation industry is responsible for 5% of anthropogenic radiative forcing, which causes climate change. In addition, the industry has been growing at a steady rate of 5% per year for decades and is expected to keep growing over the coming decades. As a result there is a need for solutions that reduce the environmental impact of flying in the short term. To that end the A321appu is introduced. This next-generation version of the Airbus A321neo will feature a fuselage boundary layer ingesting propulsor powered by hydrogen combustion, named the Auxiliary Propulsion and Power Unit (APPU), in the place of the conventional APU. After a promising first order assessment of the concept, this study provides a comprehensive conceptual performance assessment of the aircraft.

This study uses an automated conceptual aircraft design tool to model the effects of implementing an APPU into an Airbus A321neo-based reference aircraft. The reference aircraft is modified by implementing a cryogenic liquid hydrogen storage tank, a cryogenic fuel system, and a third hydrogen-combusting turboshaft engine into the unchanged tailcone of the reference aircraft. To allow for this installation the horizontal stabiliser is moved onto the vertical stabiliser in a cruciform empennage configuration. A 3.44 m diameter 10-bladed fuselage boundary layer ingesting propeller is mounted to the tip of the tailcone.

Implementing an APPU onto the reference aircraft results in a reduction in mission energy consumption, maximum take-off mass and CO₂-emissions. Water vapour emissions are found to increase, while operational empty mass is largely unaffected. These effects grow stronger with increasing APPU thrust share.

At the highest APPU thrust share, limited by the available space for the cryogenic storage tank in the unmodified tailcone, mission energy consumption is found to decrease by 1.3% over the reference aircraft. The implementation of boundary layer ingestion is found to be responsible for 70% of this reduction. The maximum take-off mass of the modified aircraft reduces by 2% as a result of reduced total fuel mass. CO₂-emissions are found to decrease by 11% and water vapour emissions increase 14%, largely following the inherently different emissions profile of hydrogen when compared to kerosene.

The performance of the APPU-equipped aircraft is concluded to be strongly dependent on the performance of the APPU propulsor, which is found to operate with a 16% higher propulsive efficiency compared to the main engines. A result that is attributed largely to the implementation of boundary layer ingestion in combination with the higher propulsive efficiency found for propellers over turbofans. A lack of relevant propeller reference data in combination with the proven challenge of operating a propeller at high advance ratio and Mach number, result in large uncertainty of the propulsor performance and might jeopardise the otherwise promising performance estimates of the APPU implementation.

In conclusion, the implementation of the APPU does not strongly affect the performance of the aircraft but does result in considerably lower CO₂-emissions coupled increased water vapour emissions. The exact performance of the aircraft is strongly dependent on the detailed design of the APPU and the performance of its propulsor. The structural design of the tailcone including the secondary fuel system, cryogenic fuel tank, and APPU integration will be a considerable design challenge, upon which the weight performance of the APPU-equipped aircraft depends.

Future research should focus on understanding the flow field surrounding the tailcone at high Mach number. This should support a detailed assessment of propulsor performance at high advance ratios in boundary layer ingesting configuration, which is needed to provide greater insight into the performance of an APPU. The propulsor structural design, and its ability to cope with the non-uniform inflow at the tip of the tailcone, is also key to the success of the APPU concept. The presented cryogenic tank insulation performance and the performance of the APPU propulsor are suggested as minimal design requirements for the further development of the APPU.

Contents

Preface	i
Summary	ii
List of Figures	iv
List of Tables	v
Nomenclature	1
1 Introduction	1
2 Literature Review	3
2.1 Liquid Hydrogen as On-board Energy Carrier	3
2.1.1 Hydrogen as an Energy Carrier	3
2.1.2 History of Hydrogen Powered Aviation	5
2.1.3 Hydrogen Combustion	6
2.2 Liquid Hydrogen Storage and Fuel Systems	8
2.2.1 Liquid Hydrogen Fuel Systems	9
2.3 Boundary Layer Ingestion	10
2.4 Propfans	12
3 Methodology	14
3.1 The Aircraft Design Initiator	14
3.2 Class I Hybrid Sizing	15
3.3 Powertrain Modelling	16
3.4 Aircraft Weight Estimation	19
3.4.1 Aircraft Weight Breakdown	19
3.4.2 Operational Empty Weight Estimation	20
3.5 Liquid Hydrogen Storage Tank Sizing	21
3.6 Fuel System Sizing	23
3.7 Propulsion System Performance	23
3.8 Boundary Layer Ingestion Modelling	24
3.9 Design Studies	25
4 Results	27
4.1 Reference Aircraft	27
4.2 The Effect of Adding an APPU	28
4.3 A321appu Design	35
4.4 Propulsor Performance	42
5 Discussion	46
5.1 Discussion of Results	46
5.2 Discussion of Propulsor Performance	48
5.3 Discussion of Aircraft Weight	49
5.4 Discussion of Study Limitations	51
6 Conclusion	52
Bibliography	54
A Reference Aircraft XML Input File	61
B A321appu XML Input File	72

List of Figures

2.1	Aviation energy sources and their relative weight and volume compared to Jet-A	4
2.2	Theoretical flame temperatures of hydrogen at different equivalence ratios	7
2.3	An impression of the micromix prototype combustor designed for the APU GTCP36-300	8
2.4	Schematic of the liquid hydrogen fuel system	10
2.5	Momentum flow through a boundary layer ingesting fuselage fan	11
2.6	Comparison of turboprop and turbofan (represented by the DC-9 Super 80) projected fuel burn and range	13
3.1	Class I Hybrid sizing routine workflow	15
3.2	Serial/Parallel Partial Hybrid powertrain architecture	16
3.3	Dual-fuel powertrain architecture	18
3.4	Class I weight breakdown	20
3.5	Simplified tailcone geometry used for estimating the effect of BLI	25
4.1	Reference aircraft with landing gear struts extended	27
4.2	Reference aircraft front view with landing gear struts extended	28
4.3	A321appu front view with landing gear struts extended	28
4.4	Reference aircraft side view with landing gear struts extended	29
4.5	A321appu side view with landing gear struts extended	29
4.6	Reference aircraft top view with landing gear struts extended	30
4.7	A321appu top view with landing gear struts extended	30
4.8	Normalised MTOM breakdown for different APPU shaft power shares	31
4.9	Normalised OEM breakdown for different APPU shaft power shares	32
4.10	Total energy consumption for the extended maximum range at maximum payload mission for different APPU shaft power shares	33
4.11	Greenhouse gas emissions for different APPU shaft power shares	34
4.12	Gravimetric efficiency of the liquid hydrogen storage tank for different APPU shaft power shares	35
4.13	A321appu with landing gear struts extended	35
4.14	A321appu with 10% APPU shaft power share OEM breakdown	36
4.15	APPU engine mass breakdown for 10% shaft power share	37
4.16	A321appu with 10% APPU shaft power share systems mass breakdown	37
4.17	Close-up of the A321appu tailcone	38
4.18	Two-dimensional layout of the liquid hydrogen storage tank for 10% APPU shaft power share	39
4.19	Scissor plot comparing the A321appu with 10% APPU shaft power share and the reference aircraft	40
4.20	Payload-range diagram for the A321appu and the reference aircraft	40
4.21	Mission energy saving with respect to the reference aircraft	41
4.22	Propulsive efficiency of the propulsors for different APPU shaft power shares	43
4.23	APPU propulsor inflow velocity profile	43
4.24	Sensitivity of total energy consumption to a change in propulsive efficiency	44
4.25	Sensitivity of aircraft to a change in propulsive efficiency	45

List of Tables

2.1	The characteristics of hydrogen compared to Jet-A kerosene	5
3.1	Powertrain control variables for different hybrid powertrain architectures	17
3.2	Top level aircraft requirements	26
4.1	Aircraft parameters for the APPU-equipped aircraft with 10% APPU shaft power share	42

Nomenclature

Symbols

A	Surface area	$[m^2]$
AR	Aspect ratio of the main wing	[-]
b	Main wing span	[m]
c.g.	Centre of gravity	[-]
C_D	Drag coefficient	[-]
C_{D0}	Zero-lift drag coefficient	[-]
D	Diameter	[m]
e	Safety factor	[-]
h_{lg}	Latent heat of vaporisation	[K]
k	Correction factor	[-]
k_{ins}	Thermal conductivity of the insulation material	[W/mK]
L	Length	[m]
l	Length	[m]
m	Mass	[kg]
m	Mass flow	[kg/s]
N	Number	[-]
P	Power	[W]
P	Pressure	[bar] or [Pa]
Q_w	Heat inflow into the tank	[W]
r	Radius	[m]
S	Surface area	$[m^2]$
T	Temperature	[K]
T	Thrust	[N]
T_c	Thrust coefficient	[-]
t	Thickness	[mm]
u	Velocity	[m/s]
U	Velocity	[m/s]
V	Volume	$[m^3]$
v	Velocity	[m/s]
W	Weight	[N]
W_{mix}	Work done on the fluid to reduce stratification	[J]
x	Position along the fuselage	[m]
y	Vertical coordinate	[m]

Greek letters

δ_{99}	Boundary layer thickness	[m]
η	Efficiency	[-]
ρ	Density	$[kg/m^3]$
σ	Stress	[MPa]
Φ	Supplied power ratio	[-]
ϕ	Energy derivative	[-]
ϕ	Shaft power ratio	[-]
ψ	Powertrain de-coupling parameter	[-]

Subscripts

amb	Ambient	[-]
bat	Battery	[-]

BLI	Boundary layer ingestion	[-]
E	Energy	[-]
Estorage	Energy storage	[-]
EM	Electric machine	[-]
e	Electric	[-]
e	Engines	[-]
edge	At the edge of the boundary layer	[-]
f	Fuel	[-]
fs	Fuel system	[-]
fuel	Fuel	[-]
fus	Fuselage	[-]
Fuselage	Fuselage	[-]
g	Gaseous phase	[-]
grav	Gravimetric	[-]
gb	Gearbox	[-]
gt	Gas turbine	[-]
H	Horizontal stabiliser	[-]
in	Inflow	[-]
ins	Insulation	[-]
iso	Isolated	[-]
LH2	Liquid hydrogen	[-]
l	Liquid phase	[-]
liner	Liner	[-]
out	Outflow	[-]
p	Propulsive	[-]
p	Propulsor	[-]
prop	Propulsive	[-]
PL	Payload	[-]
S	Shaft	[-]
Shaft	Shaft	[-]
S1	Primary shaft	[-]
S2	Secondary shaft	[-]
TC	Tailcone	[-]
TO	Take-off	[-]
t	Tank	[-]
vent	For venting	[-]
wing	Wing	[-]
1	Primary	[-]
2	Secondary	[-]
∞	Freestream	[-]

Superscripts

ref	Reference	[-]
'	Full aircraft minus wing and powertrain	[-]
*	Aircraft minus parts with <5% change	[-]

Chemical notations

CO	Carbon monoxide	[-]
CO ₂	Carbon dioxide	[-]
C _x H _x	Hydrocarbons	[-]
H ₂	Dihydrogen	[-]
H ₂ O	Water	[-]
LH2	Liquid hydrogen	[-]
LNG	Liquid natural gas	[-]
NO _x	Nitrous oxides	[-]
O ₂	Dioxygen	[-]

1

Introduction

Aviation is at the centre of our modern society. In 2019 over 4.5 billion passengers took the skies on regularly scheduled flight¹. Moreover, the aviation industry contributes roughly \$3.5 trillion to the global GDP and sustains over 87 million jobs worldwide [1]. As the sector has connected us and brought us closer than ever, it has seen an sustained year-over-year growth of 5% [2, 3]. Both Airbus [1] and Boeing [4] predict this trend to continue, with expected yearly growth of around 4% from 2023 onward.

The on-going Covid-19 pandemic has resulted in the air-travel industry facing an unprecedented crisis. Following a record year in 2019, passenger numbers in 2020 dropped by 2.7 billion and resulted in a 66% decline in Revenue Passengers Kilometres (RPKs). However, though the industry is expected to see reduced passenger numbers and lower overall growth for a number of years, it is forecast to return to pre-pandemic levels around 2024 [1, 3, 5]. By 2040 it is believed that the pandemic will have resulted in a 2-year lag of the industry behind the pre-pandemic market predictions.

As a direct result, both Airbus [1] and Boeing [4] expect overall new aircraft sales leading up to 2040 to reach around 40,000 units in total. Around 75% of all new deliveries will fall in the single-aisle category, with a typical range up to 3,000 NM. A further 14% of new aircraft deliveries will fall into the medium market segment, served by both single-aisle and wide-body aircraft with a typical range up to 5,000 NM. The Airbus A321 falls between the small single-aisle and the medium categories of aircraft, and is therefore ideally positioned to benefit from the recovery and subsequent growth of the air-travel market.

In stark contrast to the optimistic news on aviation market forecasts, are the growing environmental concerns surrounding the industry's seemingly unstoppable growth. Recent studies by Lee et al. [6, 7] conclude that aviation is responsible for around 5% of anthropogenic radiative forcing, which causes global warming and climate change. The continued growth of the industry means that this number is expected to worsen if the industry refrains from drastic action to reduce its environmental impact.

To this end, ACARE [8] has defined a comprehensive set of goals for the industry in 2050. Compared to a typical aircraft delivered in 2000, new aircraft in 2050 should achieve a 50% reduction in CO₂ emissions and a 90% reduction in NO_x-emissions. Moreover, all ground operations should be 100% emission-free. Further ambitions have been presented by [9], who strive for carbon-neutral growth of the industry from 2020 onward and an overall reduction in CO₂-emissions of 50% by 2050. The goals are envisioned to be achieved through a combination of technological breakthroughs, more efficient operations, and new aviation fuels. In the end, these should allow the industry to sustain its growth while reducing its environmental impact. Reaching these goals calls for ambitious new designs and technical solutions to be developed and deployed in the next years.

The A321appu is introduced to provide an answer to this call. This next-generation version of the Airbus A321neo features a liquid hydrogen-powered boundary layer ingesting propulsive fan in the place of the more conventional Auxiliary Power Unit (APU). The modification, named the Auxiliary Power and Propulsion Unit (APPU), was first introduced in a Bachelor Design Synthesis Exercise at the Aerospace Engineering faculty of the Delft University of Technology by Acevedo et al. [10] in 2020. The project studied the implementation of

¹ICAO <https://www.icao.int/annual-report-2019/Pages/the-world-of-air-transport-in-2019.aspx>, accessed 04-05-2021

an APPU on a next-generation version of the Airbus A320neo and concluded a promising 20% reduction in overall CO₂-emissions and up to 50% reduction in local emissions.

The idea of using liquid hydrogen as an onboard energy carrier is not new. In fact it has been considered a promising high-energy fuel since the 1940's. Recent studies concluded that it has great potential in reducing the environmental impact of flying if implemented correctly [11, 12]. Moreover, the application of fuselage boundary layer ingesting propfans has also been studied before. Their application has proven promising in reducing the overall energy consumption of the aircraft, as presented in for example the CENTRELINE project [13]. However, the application of a fuselage boundary layer ingesting propfan in combination with hydrogen combustion in a retrofit design of an existing modern airliner has not been studied before.

In response to the urgent need for aircraft designs that lower the environmental impact of the aviation industry, the APPU project sets out to bring these concepts out of the research phase and implement them onto a next-generation version of a commercially viable airliner that could hit the market by as early as 2035. In this way the project aims to provide a substantial contribution towards achieving the aviation industry's environmental ambitions, and speed up the large-scale deployment of hydrogen-powered flight.

Following the promising first findings by Acevedo et al. [10], the project calls for a more detailed first-order performance estimation of the aircraft concept. This study aims to satisfy that need and provide a conceptual design of the aircraft as well as a high level performance estimation. This study therefore aims to answer the following question:

What reduction in greenhouse gas emissions can be achieved by implementing a fuselage boundary layer ingesting propulsive fan powered by a hydrogen combusting APPU into a hereto optimised version of the Airbus A321neo?

In order to properly answer this question, it has been dissected into four sub-questions that focus on various aspects of the design changes and their effect on the aircraft performance. They are presented below.

1. What is the effect of using a fuselage boundary layer ingesting propulsor to generate this amount of thrust on the total energy consumption of the aircraft?
2. What is the effect of using hydrogen combustion to generate this amount of the thrust on the greenhouse gas emissions of the aircraft?
3. What is the effect of implementing a fuselage boundary layer ingesting hydrogen combusting APPU on the overall aircraft design?
4. What is the maximum achievable reduction in greenhouse gas emissions respective to the reference aircraft by implementing a fuselage boundary layer ingesting hydrogen combusting APPU?

This report will first present a comprehensive literature review in Chapter 2. This literature review will provide the theoretical basis for the study and is a condensed version of the full literature study presented by Burger [14], which accompanies this report. Chapter 3 describes the methodology through which this study has been conducted, in detail. The results of the study are presented in Chapter 4 and they are subsequently discussed in Chapter 5. The latter also provides an overview of the limitations of the study. Chapter 6 provides answers to the various sub-questions and synthesises these into a comprehensive answer to the main research question. This chapter also provides suggestions and recommendations for future research into the APPU concept.

2

Literature Review

This chapter presents an overview of the scientific landscape surrounding the APPU project and provides a theoretical basis for the study. A more elaborate overview of the scientific literature applicable to this study was presented earlier in the accompanying literature study by Burger [14].

This literature review is split into four sections that cover the most relevant aspects of the study. The use of liquid hydrogen as an on-board energy carrier in aviation is covered in Section 2.1. The on-board storage of liquid hydrogen and the required secondary fuel system are discussed in Section 2.2. Section 2.3 explores the theoretical principle behind boundary layer ingestion as well as its implementation and expected performance. Finally, Section 2.4 discusses the implementation of propfan engines.

2.1. Liquid Hydrogen as On-board Energy Carrier

For many years liquid hydrogen has been considered a promising energy carrier by the aviation industry. In fact, the first ever demonstration of a turbojet engine designed for aviation ran on hydrogen and was designed by Dr. Hans von Ohain at the Heinkel Aircraft Company in Germany in 1937 [15]. After this first implementation of hydrogen on an aero-engine, the United States Airforce further developed the use of liquid hydrogen during the 1950's as it was considered the ultimate high energy fuel. The development in these years focused on designing aircraft that could fly higher, faster and further through the use of liquid hydrogen. During the same period liquid hydrogen was also being researched to be used as rocket propellant in the American space program [16]. The aviation industry's interest in liquid hydrogen rose again during the 1970's and 1980's as crude oil reserves diminished and fuel prices surged. For the first time liquid hydrogen was considered as a replacement of kerosene on commercial flights [17]. In recent decades the use of hydrogen as an aviation energy carrier has seen renewed interest in response to the industry's ambition to reduce its environmental impact [11, 12, 18, 19]. This is further highlighted by Airbus' push to develop a range of hydrogen powered aircraft [20].

All three of these development phases highlight one of the multiple distinct advantages to using liquid hydrogen as an aviation fuel; its high gravimetric energy density, its abundance, and its potential to reduce the emission of greenhouse gasses. Each of these aspects will be explored in greater detail below.

2.1.1. Hydrogen as an Energy Carrier

In recent decades liquid hydrogen has been considered a promising new energy carrier for aviation in an attempt to reduce greenhouse gas emissions from aircraft operations. The reasoning behind this is multifold. First of all, liquid hydrogen can be produced from water by electrolysis using renewable energy. The subsequent energy extraction on-board the aircraft would yield mostly the emission of water vapour and, when hydrogen combustion is used, an amount of NO_x [21]. In theory this means that liquid hydrogen can be a very clean and sustainable energy carrier, with very little emissions in the production process and merely the emission of water vapour, which can be a potent greenhouse gas at high altitude in itself, and NO_x as a result of energy extraction on-board of the aircraft [18]. In fact, Clarkin [22] concludes that when hydrogen is produced using renewables, "net carbon emissions could be reduced to near zero".

Secondly, liquid hydrogen has a high specific energy density, meaning that a large amount of energy can be extracted from 1 kg of liquid hydrogen. In fact, as can be observed from Figure 2.1 by Gangoli Rao et al. [11], the relative weight of hydrogen as an energy carrier is the lowest of all potential aviation energy sources analysed, with its specific energy density around three times higher than the specific energy density of Jet-A kerosene [17, 23]. This means that for the same mission energy requirement, the total mass of fuel can be reduced by two-thirds [24].

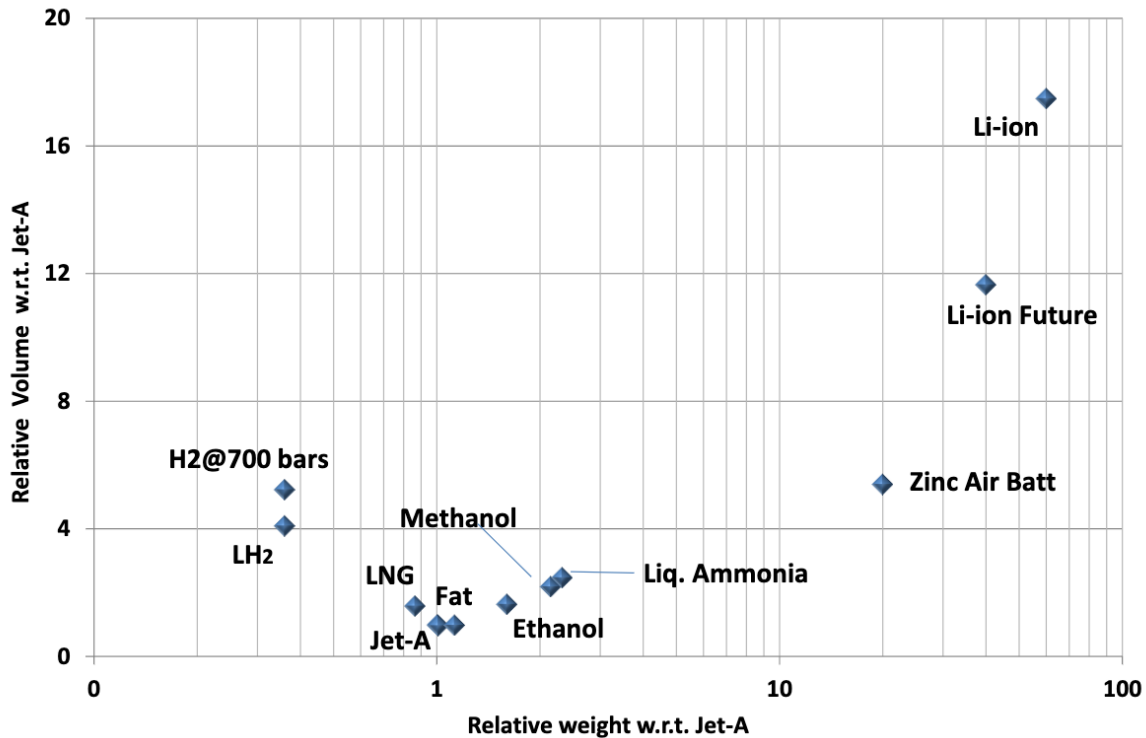


Figure 2.1: Aviation energy sources and their relative weight and volume compared to Jet-A [11]

Furthermore, hydrogen is abundantly available. In fact hydrogen is the most abundant element, although it is often bonded with other elements in, for example, water (H_2O) or hydrocarbons (C_xH_x) [18]. Pure hydrogen can be, and commonly is, produced from hydrocarbons or by electrolysis of water. Producing hydrogen by means of steam reforming of hydrocarbons emits substantial quantities of CO_2 and is still reliant on the availability of fossil fuels [22]. On the other hand, electrolysis of water splits the molecule into oxygen and hydrogen using electricity. This process thus requires a steady supply of water and electricity. When the electricity is provided by means of renewable energy sources, the greenhouse gas emissions of the production of hydrogen will be almost zero, the process will merely emit oxygen [22].

The fact that the production and liquefaction of hydrogen merely requires a steady supply of water and (green) electricity means that hydrogen production can be realised in almost every country around the world, giving these countries greater independence from fossil fuel producing states [17, 21]. Additionally, Gangoli Rao et al. [11] conclude that the total amount of hydrogen currently produced on a yearly basis is similar to the quantity of jet fuel consumed, hinting at the fact that producing the amount of hydrogen required to sustain global aviation is within the realm of possibility.

From Figure 2.1 it is also evident that hydrogen, both in liquid and gaseous form, has a considerably lower volumetric energy density than conventional aviation fuels. In fact liquid hydrogen requires roughly four times the amount of volume for the same amount of energy as Jet-A kerosene [11, 23]. This results in one of the main challenges in introducing hydrogen as the aviation fuel of the future; the required volume for the on-board storage of the fuel.

In the current state of the art, hydrogen is commonly stored in its liquid form or in its gaseous form at a pressure of around 700 bars. The basic characteristics of hydrogen in both forms are presented and compared to the characteristics of Jet-A kerosene in Table 2.1 [11, 23]. From the table it can once more be concluded that hydrogen has a specific energy density around 2.8 times higher than Jet-A. However, it can also be concluded that the volumetric energy density of hydrogen, even in its compressed or liquid form, is much lower than that of Jet-A. For storing the same quantity of energy, liquid hydrogen would require around 4 times the amount of volume compared to Jet-A, and storing hydrogen at 700 bars requires almost 7 times the amount of storage volume.

Table 2.1 also indicates that in order to store hydrogen in its liquid form, its temperature should be kept below -253°C . If the temperature rises above this threshold, the hydrogen will start to evaporate. A more in-depth discussion on the storage of liquid hydrogen is presented in Section 2.2.

Table 2.1: The characteristics of hydrogen compared to Jet-A kerosene [11, 23]

	Jet-A @ 1atm	Liquid hydrogen @ 1atm	Hydrogen @ 700bar
Specific energy density [MJ/kg]	43	120	120
Volumetric energy density [MJ/l]	34.4	8.5	5.0
Density [kg/m^3]	800	71	42
Boiling point [$^{\circ}\text{C}$]	176	-253	-

2.1.2. History of Hydrogen Powered Aviation

The history of hydrogen-powered aviation is rich and started with the very first demonstration of an aviation turbojet engine that ran on gaseous hydrogen in 1937 [15]. The first ever successful partial hydrogen-powered flight was performed on the 13th of February 1957 at the NACA-Lewis Flight Propulsion Laboratory in Cleveland, using a twin-engined B-57B bomber that had one its engines converted to run on hydrogen. One of the two Curtiss Wright J-65 turbojet engines was switched over from kerosene to hydrogen mid-flight, thereby proving that hydrogen-powered aviation was possible [16].

Following the successful hydrogen-powered test flight of the B-57B, multiple new research projects into the aeronautical application of liquid hydrogen were started by the United States Airforce. Most notable was project Suntan, a liquid hydrogen-powered replacement of the CIA's U2 spy plane that was destined to fly higher, faster and further than its predecessor. The aircraft was under development by Lockheed Martin from 1956 until the project's cancellation in 1958. The technological developments and test facilities were later used in the development of the space program [16].

The 1970's and 1980's saw a considerable step in the development of commercial hydrogen-powered aircraft, with a large number of publications on the detailed design and performance assessment of fully liquid hydrogen-powered commercial aircraft [17, 25–28]. These publications were summarised by Brewer [29], which still provides a wealth of relevant information on the detailed design of these aircraft. Besides these publications, the USSR performed a series of successful test flights, using a modified Tupolev TU-154 three-engined single-aisle passenger aircraft, in 1988 and 1989. The aircraft, named the TU-155, had one of its NK-88 turbofan engines modified to run on both liquid hydrogen and LNG. The engine was outfitted with a new heat exchanger, new turbopump and a modified combustion chamber. The aircraft also featured an elliptical cryogenic storage tank at the rear of the fuselage. The test campaign involved a considerable number of test flights across the USSR and Europe, and validated the feasibility of partially running a commercial aircraft on liquid hydrogen [30].

The start of a new millennium also saw the start of the CRYOPLANE¹ project. The project was a large-scale design and feasibility study into fully hydrogen-powered commercial aircraft. The final report by Westenberger [31] concluded that, while a lot of the technological development was still required, no technical showstoppers for the implementation of the novel fuel could be identified. The project also concluded that the Operational Empty Weight (OEW) of the aircraft could increase by as much as 23% as a result of the hydrogen conversion. The change in Maximum Take-Off Weight (MTOW) could range from a decrease of 14.8% to an

¹European Commission <https://cordis.europa.eu/project/id/G4RD-CT-2000-00192>, accessed: 10-05-2021

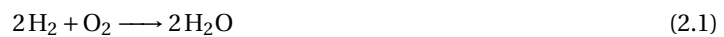
increase of 4.4% depending on specific configuration and mission requirements. The final report continues with the conclusion that hydrogen combusting conventional turbofan engines can be as efficient as their kerosene-fuelled equivalents, while the emission of NO_x can be reduced considerably through the use of micro-mix combustors [32].

Recent years have seen several new implementations of liquid hydrogen-fuelled aviation. In 2012 Boeing launched its unmanned hydrogen-powered high-altitude long-endurance Phantom Eye aircraft [33]. In June 2020 ZeroAvia, a start-up company affiliated with the Cranfield University, performed the first commercial scale electric test flight in the UK on their hydrogen fuel cell electric Piper M-class aircraft. The company is currently preparing its hydrogen-powered aircraft for an entry into service in 2023 [34]. Finally, 2020 saw the announcement of Airbus' range of ZEROe concept aircraft. All three of these aircraft feature liquid-hydrogen combustion propulsion and could enter the market as early as 2035 [20].

2.1.3. Hydrogen Combustion

The APPU is powered through hydrogen combustion in the combustion chamber of a turboshaft engine. This section will briefly discuss the specifics of hydrogen combustion as well as the greenhouse gas emissions that can be expected.

In essence, the combustion of hydrogen is an exothermic oxidation reaction in which hydrogen and oxygen react to form water vapour, as presented in Equation 2.1. From the reaction equation it is clear that hydrogen is not a carbon-based fuel and, as a result, its combustion will be free of carbon-based emissions, such as CO₂, CO, unburned hydrocarbons (UHC) and soot [22]. Additionally, the combustion of hydrogen is free from sulphur based emissions. Both result in a reduction of the environmental impact of flying with respect to kerosene powered flight [7, 35].



The addition of hydrogen combustion would warrant few design changes to conventional kerosene burning turbofan engines [18, 35, 36]. The turbo machinery could remain largely the same and the hydrogen-combusting engines would be as efficient as their kerosene-powered counterparts [31]. The engines would require a new hydrogen-optimised combustion chamber, designed to mitigate the risk of flashback and reduce the formation of NO_x [37].

The formation of large quantities of NO_x, which increases radiative forcing and is directly detrimental to human health when inhaled, is of concern when combusting hydrogen as a result of hydrogen's high flame temperature [6, 7]. NO_x is formed in an endothermic oxidation reaction between oxygen and nitrogen at elevated temperatures in a series of processes described by the Zeldovich mechanism. Zeldovich [38] concluded that considerable amounts of NO_x are produced at temperatures above 1,800 °K in the presence of oxygen and nitrogen according to the reaction presented in Equations 2.2, 2.3 and 2.4. As a result of the presence of both nitrogen (N₂) and oxygen (O₂) in the air, and the elevated temperatures during hydrogen combustion, the formation of NO_x is inevitable.



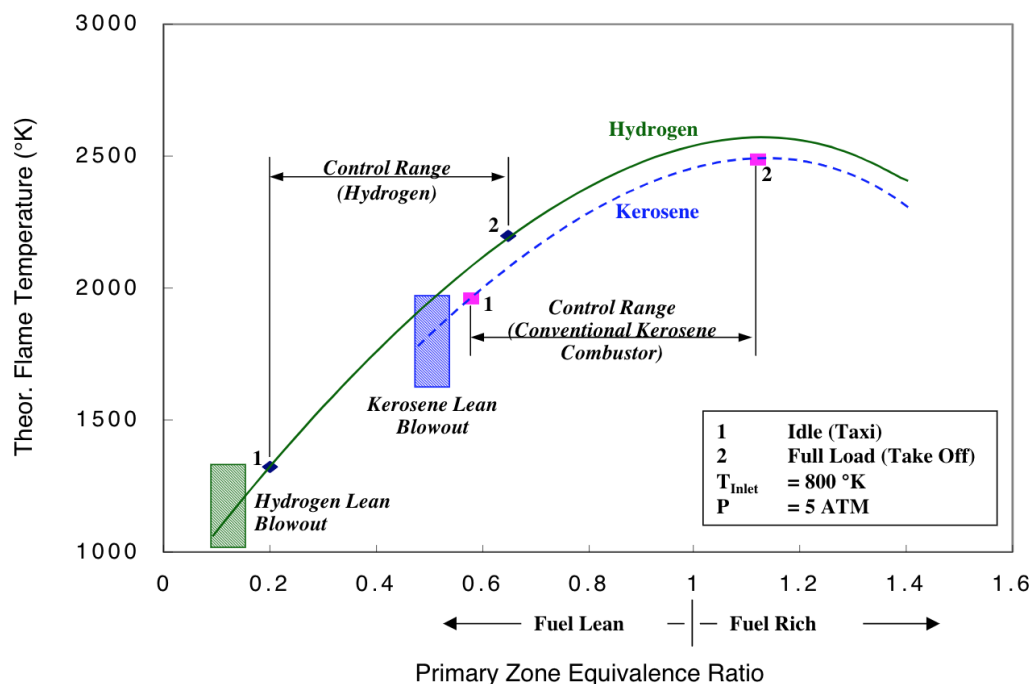


Figure 2.2: Theoretical flame temperatures of hydrogen at different equivalence ratios by Brand et al. [39]

Figure 2.2 compares the flame temperatures of hydrogen and kerosene in a gas turbine combustion chamber for different equivalence ratios. From the figure it is evident that the flame temperature of hydrogen is higher than for kerosene. As a result, the combustion of the hydrogen would lead to higher production of NO_x compared to kerosene combustion at the same equivalence ratio [38]. However, from Figure 2.2 it is also clear that hydrogen can be successfully combusted at lower equivalence ratios and accompanying lower flame temperatures than kerosene. Therefore, burning at very lean equivalence ratios, around 0.3, is an integral part of the design of hydrogen combustors in an effort to reduce NO_x formation [35, 37].

In order to further minimise the formation of NO_x, it is important to ensure that the equivalence ratio is consistently and homogeneously low throughout the combustion chamber. Local high equivalence ratios lead to local hotspots in the combustion chamber that could lead to increased NO_x formation. To prevent this, thorough mixing of fuel and air is required [32, 35, 40, 41].

Another important factor to the production of NO_x is the residence time in the combustion chamber. An increased residence time means that the reaction products are exposed to elevated temperatures for longer, thereby resulting in the Zeldovich mechanism being active for longer leading to higher quantities of NO_x being produced. Hydrogen's increased flame speed compared to kerosene is effective in decreasing the residence time [35, 37].

Using a micromix combustor, as first described by Dahl and Suttrop [32] and presented in Figure 2.3, NO_x emissions are reduced compared kerosene combustors through a combination of very lean combustion with thorough mixing using a large amount of small mixing locations. In recent years the micromix combustor, and its NO_x emission profile in particular, have been researched in detail in numerous studies [42–45]. While all conclude that significant reductions in NO_x emissions can be achieved, no model for estimating the NO_x emissions from a jet engine in real-life operation has been produced, nor is there experimental emission data available from aircraft flight testing. As a result, it is likely that a considerable decrease in NO_x-emissions can be expected for the A321XLR but this reduction cannot be quantified in this study.

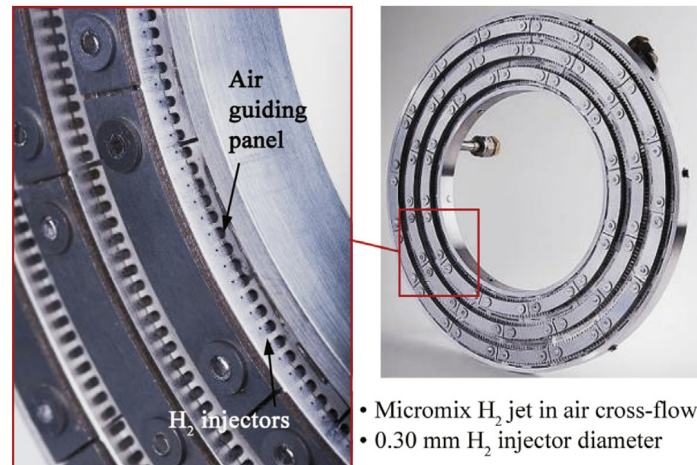


Figure 2.3: An impression of the micromix prototype combustor designed for the APU GTCP36-300 by [46]

Besides a concern for increased NO_x production, hydrogen combustion also suffers from increased flame flashback propensity. This increased risk is the direct result of hydrogen's high flame speed, high reactivity, wide flammability limits and low ignition delay [37, 40]. Flashback occurs when the direction of flame propagation reverses and the flame moves closer to the injector. In extreme cases the flame could enter the premixer and fuel lines, which can result in serious safety risks and damage to the system [47]. It is caused by the presence of an ignitable mixture of fuel and air in the premixer and fuel lines. As a result of hydrogen's high propensity to flashback, igniters, injectors and combustors are designed with the increased risk of flashback in mind [35, 37]. However, a mixture of air and hydrogen will inevitably pose a risk to flashback. Therefore, hydrogen combustors often employ diffusive combustion, a method in which the fuel and air are separated right up to the moment when they are injected into the combustion chamber, where they are immediately mixed and burned. According to Dahl and Suttrop [32] diffusive combustion is "inherently safe against flashback".

Dahl and Suttrop [32] also identify the need to flush and purge the fuel system with an inert gas to prevent a combustible mixture of air and hydrogen from being present in the system. Westenberger [31] suggests to purge the system with nitrogen before and after use.

The combustion of hydrogen emits water vapour and nitrogen oxides (NO_x), and should be free from carbon- and sulphur-based emissions, as well as from unburned hydrocarbons and soot. While the amount of NO_x emitted as a result of the combustion of hydrogen is hard to estimate due to its dependence on combustor design and engine operating conditions, the quantity of water vapour emitted is directly proportional to the amount of hydrogen combusted. Consequently, the emission of water vapour, which can be a potent greenhouse gas at altitude [21], can be reduced by minimising fuel consumption.

The combustion of 1 kg of Jet-A1 kerosene yields about 1.24 kg of H₂O emissions. The combustion of 1 kg of hydrogen on the other hand yields 8.92 kg of water vapour. Adjusting for the respective energy densities of the two fuels, the combustion of hydrogen yields around 258% more water vapour emissions than Jet-A1 kerosene per MJ of energy extracted [11, 21, 23, 48].

2.2. Liquid Hydrogen Storage and Fuel Systems

Storing hydrogen in its liquid form is considered the most advantageous way of using it as an on-board energy carrier [23]. However, from Table 2.1 it is evident that liquid hydrogen has a boiling point of -253°C and thus needs to be stored at cryogenic conditions. The design and performance estimation of a partial liquid hydrogen powered aircraft therefore requires the design and implementation of a cryogenic storage tank [49]. The design of the storage tank is critical to the performance of the aircraft and is often largely responsible for the increase in operational empty mass (OEM) of hydrogen-powered aircraft compared to their conventional kerosene-powered equivalents [17, 19, 26, 31].

Cryogenic storage tanks are characterised by a large temperature difference across the tank wall. Any heat leak from the ambient into the tank will result on the liquid hydrogen warming up and evaporating, or boiling-off. This boil-off causes the pressure in the tank to rise. When insufficient liquid hydrogen is consumed by the engines and the pressure in the tank has risen to the maximum design pressure of the tank, gaseous hydrogen will have to vented from the tank. The releasing of unconsumed hydrogen into the atmosphere effectively constitutes a waste, energy has been consumed to produce liquid hydrogen and that energy is not used in a useful manner, and should therefore be minimised [31, 49]. Consequently, cryogenic storage tanks are fitted with high performance insulation materials.

The main challenge in designing an on-board cryogenic storage tank is achieving both low overall system weight as well as low total heat leak [50]. Most cryogenic storage tanks feature a structural inner liner, designed to contain the internal pressure and cope with other mechanical loads encountered during operation, wrapped by an insulation layer. The selection of the maximum design pressure or venting pressure of the tank is of great importance here [29, 49, 51]. Selecting a low venting pressure might require more frequent venting or additional insulation, while a higher venting pressure leads to a heavier liner and lower overall gravimetric efficiency of the system. Other mechanical loads on the inner liner might be incurred by the fuel weight, aircraft acceleration, fuel sloshing due to turbulence or manoeuvring, and the weight of the tank itself [52].

It is widely recognised that monolithic metals, in particular aluminium, are most suitable for the construction of the inner liner [49, 50]. The future weight saving potential of composites is also emphasised [53]. Verstraete et al. [51] estimate that these weight savings could be as high as 25%. However, the high cost, permeability to hydrogen and low technology readiness level hinder the implementation of composites up to this point [49–51].

Three main types of insulation solutions can be identified. In order of decreasing thermal conductivity they are: foams, aerogels and multi-layer insulation (MLI). Previous studies have largely focused on foams because of their low density, low cost and ease of installation [54]. Aerogels have regularly been discarded as a result of their brittleness and inability to cope with mechanical loads. In more recent works the potential of aerogel blankets has been recognised as a solution to benefit from the very low thermal conductivity of aerogels while circumventing the problems resulting from their brittleness [51, 52, 55, 56]. Finally MLIs, comprising a combination of insulation layers combined with reflective layers of aluminium suspended in a high vacuum, are considered the most effective insulators. However, they have often been omitted as a result of the increased complexity of manufacturing and maintenance, increased structural weight of the tank and the safety risks involved with the extreme boil-off rates when the vacuum is broken [49, 51, 54].

Extensive design studies led Winnefeld et al. [49] to conclude that spherical tanks offer the best weight performance and that cylindrical tanks have better weight performance than elliptical tanks. Moreover, longer tanks have increased insulation weight while more compact tanks suffer from higher structural weight of the inner liner. Finally, they state that the highest storage efficiency is achieved when the tank is tailored for a specific design mission. Prewitz et al. [23] support this by concluding that for optimal performance the tank should be filled as far as possible.

2.2.1. Liquid Hydrogen Fuel Systems

Besides safely and efficiently storing the liquid hydrogen in the cryogenic tank, the hydrogen fuel system is also responsible for delivering the correct amount of gaseous hydrogen at the right pressure to the APPU combustion chamber. The system should also be able to support refuelling, fuel-dumping and the venting of gaseous hydrogen. A schematic of a liquid hydrogen fuel system designed for a sub-sonic commercial passenger aircraft is presented in Figure 2.4 by Brewer and Morris [26]. The system consists of the storage tank, two sets of fuel pumps and heat exchangers. The first set of fuel pumps, called the booster pumps, ensure a steady flow of liquid hydrogen to the high pressure fuel pumps in all flight scenarios. They prevent the liquid hydrogen from evaporating in the fuel lines, which would lead to cavitation at the high pressure fuel pump resulting in an interruption of the fuel supply to the engine and damage to the pump. The heat exchangers ensure that gaseous hydrogen is fed to the engine's combustion chamber.

The cooling capacity of the liquid hydrogen can be used to cool the engine and the cabin air. This synergistic approach to heat management has been shown to allow for considerable gains in the thermal performance of the full system, but is considered beyond the scope of this study [17, 26, 57]. Westenberger [31] reports on a heat exchanger fitted around the engine's jet pipe, which for an Airbus A321 is estimated to weigh around 11 kg and only leads to a small reduction in engine thrust as a result of reduced exhaust flow temperature.

While the exact detailed design and layout of the full liquid hydrogen fuel system is beyond the scope of this study, a method for determining its weight by Onorato [58] is presented in Section 3.6.

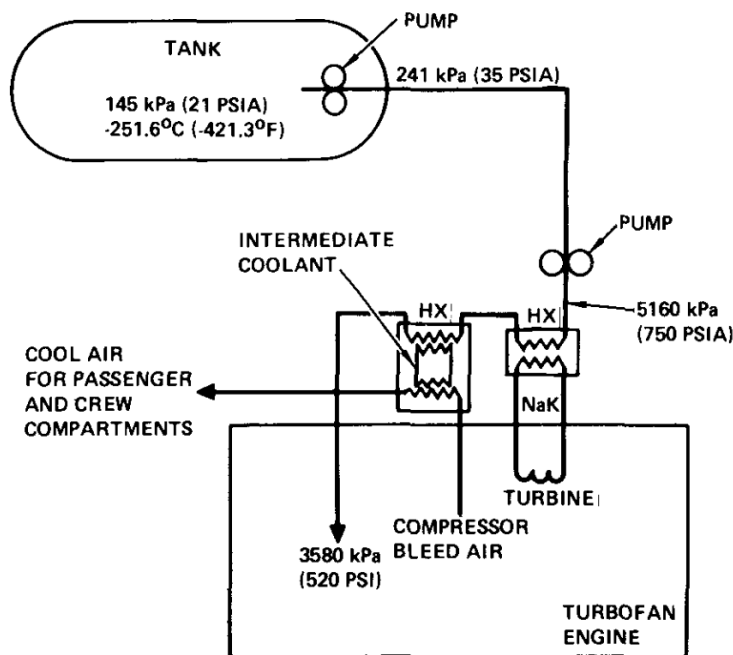


Figure 2.4: Schematic of the liquid hydrogen fuel system designed by Brewer and Morris [26]

2.3. Boundary Layer Ingestion

Boundary layer ingestion propulsion is a propulsion technique in which slower moving boundary layer air is ingested into the propulsor in order to generate thrust [59]. The first theories on boundary layer ingestion (BLI) propulsion were published by Smith and Roberts [60] in 1947, while the first methods to estimate its performance are documented in the work by Smith [59] from 1993. In recent years the technology has seen a renewed interest in a quest to reduce aircraft fuel burn [61–64].

The concept of boundary layer ingestion, and in particular fuselage boundary layer ingestion, will be explained with the help of Figure 2.5 by Seitz and Gologan [65]. Boundary layer ingestion or wake-filling propulsion works by ingesting the slower moving boundary layer air into the propulsor to generate thrust. This has two major benefits; it reduces the momentum deficit from the boundary layer and simultaneously reduces the momentum excess of the jet [66]. Both effects can be identified from Figure 2.5.

In Figure 2.5 A, the boundary layer around the fuselage and a separated propulsor can be distinguished. In the wake that results from this system, it is evident that there is a momentum deficit that has resulted from the fuselage boundary layer, while a momentum excess can be identified behind the propulsor. The momentum deficit from the fuselage, and other components of the aircraft, constitutes an energy loss in the system that is often referred to as viscous and form drag. In total these two drag components account for between 55% and 65% of the total drag of a conventional transport aircraft [65, 67].

The excess momentum resulting from the propulsor is called the jet wake. It leads to mixing of flows as the flow velocities of the wake and the freestream equalise. This process, called jet dissipation, also constitutes a source of energy loss in the system.

When applying BLI, the momentum deficit of the boundary layer, or part thereof, is filled with the momentum excess of the propulsor jet wake, as can be seen in Figure 2.5 B. The boundary layer is thus ingested and its wake is filled, hence the terms boundary layer ingestion and wake filling. This results in both a lower momentum deficit and a lower momentum excess in the wake of the aircraft, and thus reduces the losses and yields a possible reduction in the required propulsive power [65]. Effectively the kinetic energy invested in fuselage wake is used to generate thrust in the propulsor [68].

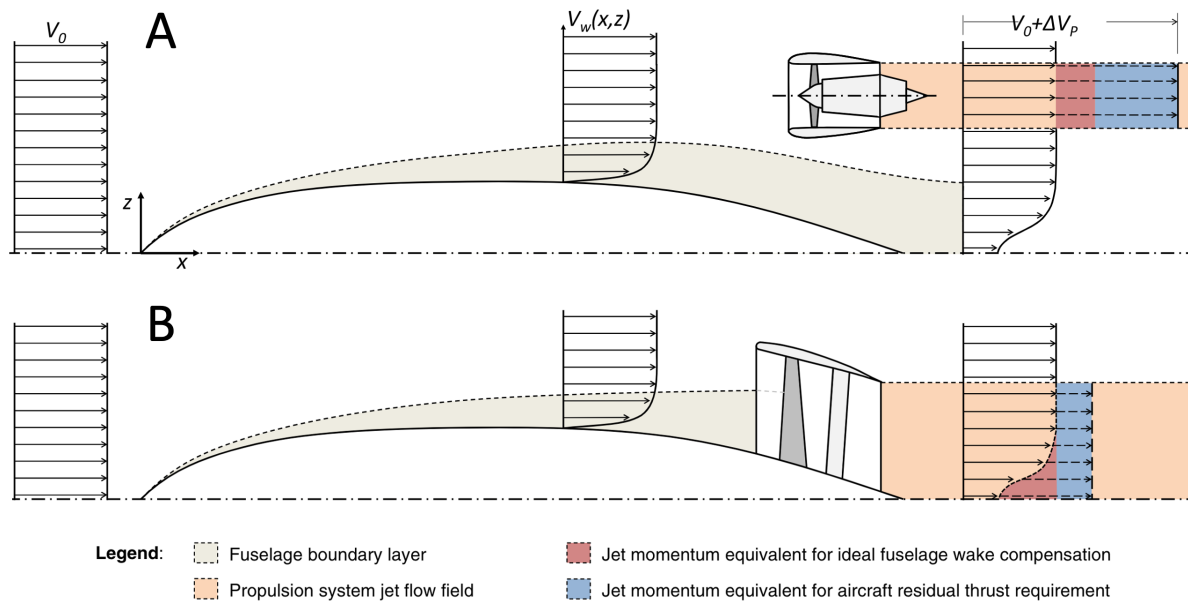


Figure 2.5: Momentum flow through a boundary layer ingesting fuselage fan, adapted from Seitz and Gologan [65]

Hall et al. [66] discern five effects of the implementation of fuselage BLI on an aircraft: reduced jet dissipation losses, reduced wake mixing, reduced engine installation losses, reduced propulsion system efficiency, and altered airframe performance as a result of the aero-propulsive coupling between the propulsor and the airframe.

The reduction in propulsion system efficiency is attributed to increased inlet distortion in BLI propulsors resulting from non-uniform boundary layers. Similar conclusions are drawn by Marien et al. [62], who assume a 3.5% reduction in fan efficiency to account for increased inlet distortion.

Moreover, mounting a propulsor in a fuselage wake-ingesting configuration establishes a strong aero-propulsive coupling, which may alter the performance of the airframe and complicates the accounting of thrust and drag [66, 69]. Lv et al. [68] identified several aerodynamic phenomena that result from the interacting pressure fields between airframe and propulsor. First, the propulsor establishes a region of reduced pressure over the aft-fuselage which reduces the pressure recovery and was found to increase fuselage pressure drag. Moreover, the propulsor suction results in a negative pressure gradient towards the suction side of the propulsor which causes a local thinning of the boundary layer, and induces an increase in viscous drag over the aft part of the fuselage [66]. In total Lv et al. [68] found that fuselage drag increased by 6.1% as a result of the BLI propulsor.

These effects are not considered detrimental to the performance of the full system of airframe and propulsor, as the reduced pressure recovery over the fuselage leads to increased pressure recovery downstream of the propulsor. Moreover, the additional viscous drag leads to more kinetic energy being captured in the boundary layer, which when ingested is (partially) recovered by the propulsor. Overall the performance of the airframe decreases while the performance of the propulsor is enhanced. This complicates the accounting of

thrust and drag and inspired Lv et al. [68] to conclude that targeting the lowest fuselage drag might lead to decreased overall performance. Instead they suggest optimising for minimal effective power consumption of the integrated system of airframe and propulsor. Not considering the two together might lead to a large error in the performance estimation [70].

The potential of BLI configurations to reduce aircraft energy consumption is highlighted in numerous performance analysis studies. While the performance of a BLI equipped aircraft design is very sensitive to the exact configuration and as such results from other studies are not directly applicable to the A321appu, they might give an indication of what can be expected [62]. Hall et al. [66] found an 8.7% reduction in mechanical flow power that is directly attributable to the BLI integration on the D8 concept aircraft. On the very similar NASA D8 concept aircraft, Marien et al. [62] found a 5.6% reduction in block fuel consumption compared to a reference aircraft with conventional podded engine. Samuelsson and Grönstedt [71] reported a net reduction in mission fuel burn between 0.6% and 3.6% for their turbo-electric BLI propulsion configuration. Finally, the CENTRELINE project announced a 4.7% reduction in fuel burn compared to a non-BLI equipped reference aircraft of similar technology level [13].

Though these results are not directly applicable to the APPU configuration they do allude to a considerable reduction in mission energy consumption through the implementation of BLI on the A321appu.

2.4. Propfans

Turboprop have historically been used at lower Mach numbers. However, more recent developments have resulted in high-speed turboprop engines, featuring swept blades and thin supercritical airfoils, often referred to as propfans [72–74]. These engines use a gas generator engine core to power an unducted propeller, which provides the majority of the thrust. The A321appu will feature such an engine to power the aft-fuselage mounted single rotating propeller.

As a result of their increased bypass ratio, propfans benefit from greater propulsive efficiency when compared to turbofan engines. Bypass ratios as high as 30 to 50 can be achieved [75]. These extremely high bypass ratios result in considerably reduced fan pressure ratios and increased propulsive efficiency. Similar bypass ratios lay outside of the realm of turbofan engines due to the excessive nacelle weight and drag that would accompany them. Langmaak et al. [76] thus conclude that removing the nacelle around the fan is the only way to achieve bypass ratios and accompanying propulsive efficiencies this high.

Historically, the use of turboprop engines has often been limited to flight speeds up to Mach 0.6, because of strong efficiency drops at higher velocities. These are the result of strong compressibility effects at the blade tips as they approach local supersonic velocities. Turbofans address these effects by reducing the engine inlet velocity through the engine duct or nacelle [75]. However, due to the inherent unducted nature of a propfan, the inlet velocity is effectively equal to the flight velocity [76]. Consequently, the flight regime above Mach 0.6 has largely remained the domain of turbojet and turbofan engines [75].

In an effort to reduce fuel burn amidst a time of volatile oil prices, NASA set out to develop turboprop engines that could be operated efficiently at a cruise Mach number up to 0.8. These propfans, featuring thin supercritical airfoils and swept blades, were primarily developed in the 1970s and 1980s, with multiple research projects into so called "advanced turboprops" [75, 77, 78]. These studies found a 21% reduction in fuel burn and 10% reduction in direct operating costs for the single-rotating propeller compared to turbofan engines of a similar technology level [78]. Moreover, Figure 2.6 presents a comparison of the projected fuel burn and range for different Mach numbers for a DC-9 Super 80 powered by turbofan engines and by propfans. The figure by Saravanamuttoo [75] is based on a study by Goldsmith and Bowles [79] who found a 25% reduction in fuel burn as a result of the implementation of a propfan optimised for higher Mach numbers. From the figure it is evident that the propfan boasts significantly lower fuel burn and can achieve greater range for the same fuel weight when compared to its turbofan powered counterpart. Furthermore, it is evident that the strong rise in fuel burn occurs roughly around the same Mach number for both engine types. At the cruise Mach number of the Airbus A321, Mach 0.78², the propfan fuel burn is still considerably lower, hinting at potentially large performance benefits when it is implemented on the A321appu.

²Airbus A321 on Jane's all the world's aircraft. <https://customer.janes.com/Janes/Display/jawa0419-jawa>, accessed 4-6-2021

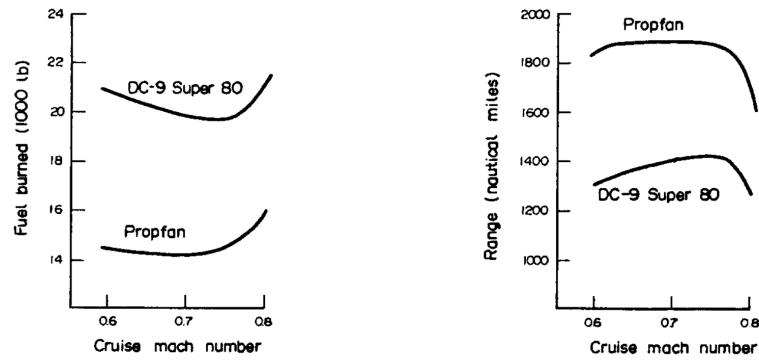


Figure 2.6: Comparison of turboprop and turbofan (represented by the DC-9 Super 80) projected fuel burn and range by Saravanamuttoo [75] based on a study by Goldsmith and Bowles [79]

The size of the propeller is one of the most important design parameters to the propeller efficiency and it is generally set early on in the design process. In general the larger the propeller, the more efficient it will be [73]. However, a larger propeller will result in higher tip speeds leading to the early onset of compressibility effects. Propeller tip speeds should be kept below sonic speeds, they therefore limit the maximum size of a propeller. This becomes more critical when the propeller is operated at higher Mach number and will form a design constraint for A321appu [73].

3

Methodology

This Chapter presents that methodology that is used in this study. It starts by presenting the Aircraft Design Initiator in Section 3.1. The implementation of hybrid aircraft and the modelling of the A321appu powertrain are described in Section 3.2 and Section 3.3, respectively. The Chapter continues with presenting the Class I aircraft weight estimation method that is used in Section 3.4. The method used for the sizing of the liquid hydrogen storage tank is described in Section 3.5, followed by an explanation of the fuel system mass estimation method in Section 3.6. The isolated propulsor performance estimation method is covered in Section 3.7, while the modelling of boundary layer ingestion (BLI) is presented in Section 3.8. Finally, the design studies that are performed are described in Section 3.9.

3.1. The Aircraft Design Initiator

The study is performed using The TU Delft Aircraft Design Initiator, from now on referred to as the Initiator, an automated conceptual aircraft design tool developed at the Faculty of Aerospace Engineering at the Delft University of Technology over the last years [80–83]. The Initiator is capable of generating feasible aircraft designs, based on a limited number of user-specified Top Level Aircraft Requirements (TLARs), that comply with regulation and requirements from European Aviation Safety Agency [84] and the Federal Aviation Regulations (FAR). The conceptual aircraft designs are generated through the automation of iterative conceptual aircraft design routines by Torenbeek [72], Raymer [73], and Roskam [85]. These design routines are augmented by more high-fidelity analysis methods, like the numerical Class II.V EMWET wing weight estimation by Elham et al. [86].

The Matlab-based software tool consists of a series of sizing modules, analysis modules and design modules that each add greater detail to the design. The modules are implemented in three convergence loops of increasing accuracy and detail. The convergence loops converge on the MTOW of the aircraft to a user-specifiable tolerance set to 10^{-3} for the lower fidelity methods and to 10^{-2} for the numerical methods, for this study. The user provides TLARs and additional design settings through a single XML-file.

The Initiator has been used in a great number of aircraft design studies and MSc. Theses at the Faculty of Aerospace Engineering, and its capability has grown over the years to be able to design for example hydrogen-powered aircraft [58], blended-wing-body aircraft [83] and aircraft featuring hybrid-electric distributed propulsion [87, 88].

The Initiator is chosen for this study due to its availability, proven accuracy, and flexibility to accommodate unconventional aircraft configurations. As the Initiator was developed to generate feasible aircraft designs and the exact design objective of existing airliners is often unknown, it is not be able to generate an exact replica of the A321neo [80]. Consequently, in order to draw conclusion on the effect of the implementation of an APPU on an A321neo, an A321neo-based reference aircraft is designed first. This is followed by the design of an aircraft featuring all APPU related modifications, designed to the same TLARs as the reference aircraft. Both aircraft designs are presented in Chapter 4.

3.2. Class I Hybrid Sizing

The Initiator incorporates a Class I sizing routine developed for hybrid electric distributed propulsion (HEDP) aircraft based on the work by De Vries et al. [87]. The sizing routine replaces the more established Class I sizing methods based on weight fractions by Raymer [73], Roskam [85] and Torenbeek [89]. The method allows for the inclusion of a secondary hybrid-electric powertrain, including a battery and electric motors, and can account for the aero-propulsive coupling effects of multiple distributed propulsion concepts.

In order to size HEDP aircraft configurations the method steps away from traditional Class I sizing workflows and incorporates a full mission analysis and component based constraint diagrams. The workflow of this HEDP-enabled Class I sizing routine, also known as the Class I Hybrid method, is presented in Figure 3.1 by De Vries et al. [87]. The more typically used Breguet's range equations have been replaced by a full energy-based mission analysis in order to account for the consumption of two types of fuel, whose depletion does not necessarily result in a reduction of aircraft weight. Moreover, the mission analysis allows for the modelling of energy harvesting and can account for aero-propulsive coupling of several distributed propulsion configurations on the energy consumption of the aircraft. A more detailed explanation on the modelling of BLI will be presented in Section 3.8.

Conventional Class I sizing methods often work with a single constraint diagram in order to size the engines and wing [73, 85, 89]. The Class I Hybrid sizing method can generate up to eight constraint diagrams to size each of the components on the hybrid powertrain. A detailed explanation of the hybrid powertrains and the respective components will be presented in Section 3.3. Each component in the powertrain might be sized by a different constraint, hence multiple design points are obtained. While the user of the method does have the ability to select the design point to be used, this study will use the design point resulting in maximum wing loading and minimum wing size.

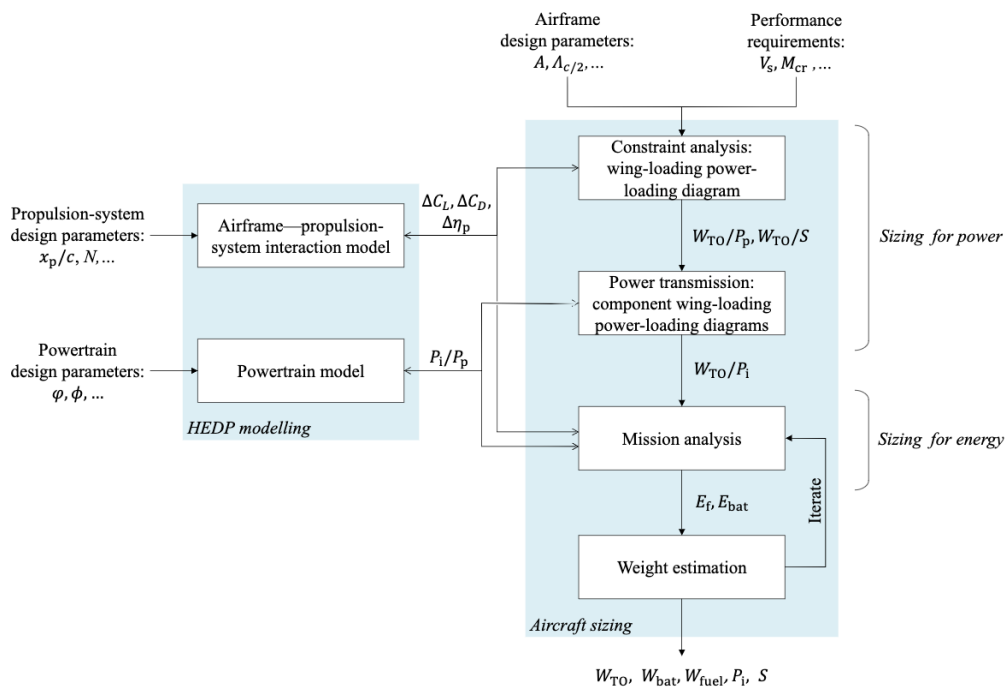


Figure 3.1: Class I Hybrid sizing routine workflow obtained from De Vries et al. [87]

From Figure 3.1 it is evident that the Class I Hybrid sizing routine progresses through a number of steps. First, an overall design point is chosen, taking into account the augmented aircraft performance as a result of distributed propulsion. Next, using the powertrain model, a power loading is computed for each of the powertrain components. The mission analysis uses the powertrain model, component power loadings and the aero-propulsive coupling effects to determine mission energy needs. The mission energy needs are subsequently used to estimate the MTOW and OEW of the aircraft. The mission analysis and aircraft weight

estimation are iterated until the value of MTOW has converged to within the user-specified error margin. Aircraft weights and high-level design parameters, as well as powertrain design parameters are finally outputted to be used in subsequent aircraft design steps.

The Class I Hybrid sizing routine by De Vries et al. [87] is selected for performing the Class I sizing of the A321appu, because it combines the capability of modelling an aircraft with two onboard energy sources with the capability of modelling the effect of several aero-propulsive coupling concepts, including BLI. As a result the method is very well suited to implement and investigate the design changes applied to the A321neo-based reference aircraft in order obtain the A321appu. However, as the method was designed to model hybrid electric powertrains, as is adapted to allow for the modelling of the A321appu. The following sections will elaborate more on the specific implementation and modifications to the Class I Hybrid sizing routine to model the A321appu.

3.3. Powertrain Modelling

The Class I Hybrid sizing method developed by De Vries et al. [87] incorporates nine different hybrid-electric powertrain architectures according to the configurations and nomenclature suggested by Felder [90] and which were subsequently adopted by the National Academy of Sciences [91]. The nine powertrain architectures are in essence all limit cases of the Serial/Parallel Partial Hybrid (SPPH) architecture presented in Figure 3.2, which is adapted from De Vries et al. [87].

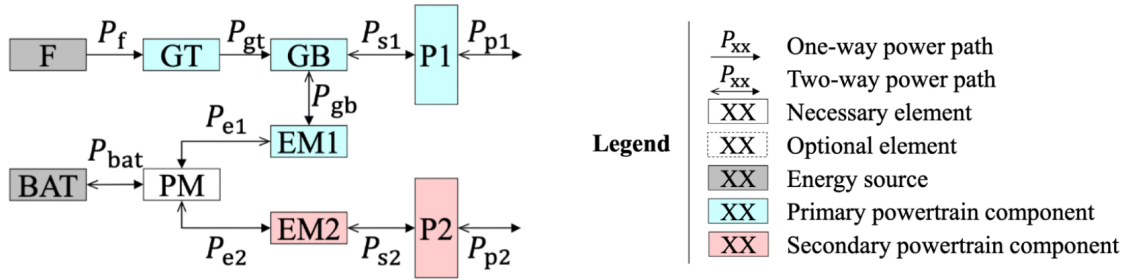


Figure 3.2: Serial/Parallel Partial Hybrid powertrain architecture, adapted from De Vries et al. [87]

De Vries et al. [87] define two powertrain control variables, the shaft power ratio, ϕ , and the supplied power ratio Φ . They are defined by Equations 3.1 and 3.2, respectively. Setting either or both ϕ and Φ to either 0 or 1 results in the various hybrid powertrain architectures as per Table 3.1, which is adapted from De Vries et al. [87].

$$\phi = \frac{P_{s2}}{P_{s2} + P_{s1}} \quad (3.1)$$

$$\Phi = \frac{P_{bat}}{P_{bat} + P_f} \quad (3.2)$$

Table 3.1: Powertrain control variables for different hybrid powertrain architectures, adapted from De Vries et al. [87]. Note that "." indicates any value and "-" indicates the variable is not used for that powertrain architecture.

Configuration	Φ	φ	ψ	N ⁰ DOF
1. Conventional	0	0	-	1
2. Turboelectric	0	1	-	1
3. Serial	.	1	-	2
4. Parallel	.	0	-	2
5. Partial TE	0	.	-	2
6. S/P partial hybrid	.	.	-	3
7. Full-electric 1	1	0	-	1
8. Full-electric 2	1	1	-	1
9. Dual-electric	1	.	-	2
10. Dual-fuel	.	.	0	2

The various power flows through the components of the powertrain and through the various power paths connecting them are found using a power balance across the various powertrain components. The power balance, presented in Equation 3.3, states that the power outputted from a component is equal to power input into the component multiplied by an efficiency factor, which represents the loss over that component. Determining the power balance for each of the components of the SPPH powertrain architecture results in seven power balance equations. For the gas turbine, gearbox, primary propulsor, primary electrical machine, secondary electrical machine, power management and distribution system, and the secondary propulsor. However, a total of ten power paths are identified. Resulting in a 3-degree of freedom system. These degrees of freedom (DOF) can be determined by the design parameters set by the designer for the supplied power ratio, shaft power ratio, gas turbine throttle, propulsive power of the primary or secondary propulsor, or the total propulsive power of the aircraft. When the supplied power ratio, shaft power ratio and total propulsive power are specified, a set of linear equations results that models the powertrain, as presented in Equation 3.4.

$$\sum P_{out} = \eta_i \sum P_{in} \quad (3.3)$$

$$\begin{bmatrix} -\eta_{GT} & 1 & 0 & 0 & 0 & 0 & 0 & 0 & 0 & 0 \\ 0 & -\eta_{GB} & 1 & 1 & 0 & 0 & 0 & 0 & 0 & 0 \\ 0 & 0 & 0 & -\eta_{P1} & 0 & 0 & 0 & 0 & 1 & 0 \\ 0 & 0 & -\eta_{EM1} & 0 & 1 & 0 & 0 & 0 & 0 & 0 \\ 0 & 0 & 0 & 0 & -\eta_{PM} & -\eta_{PM} & 1 & 0 & 0 & 0 \\ 0 & 0 & 0 & 0 & 0 & 0 & -\eta_{EM2} & 1 & 0 & 0 \\ 0 & 0 & 0 & 0 & 0 & 0 & 0 & -\eta_{P2} & 0 & 1 \\ \Phi & 0 & 0 & 0 & 0 & (1-\Phi) & 0 & 0 & 0 & 0 \\ 0 & 0 & 0 & \varphi & 0 & 0 & 0 & (1-\varphi) & 0 & 0 \\ 0 & 0 & 0 & 0 & 0 & 0 & 0 & 0 & 1 & 1 \end{bmatrix} \cdot \begin{bmatrix} P_f \\ P_{gt} \\ P_{gb} \\ P_{s1} \\ P_{e1} \\ P_{bat} \\ P_{e2} \\ P_{s2} \\ P_{p1} \\ P_{p2} \end{bmatrix} = \begin{bmatrix} 0 \\ 0 \\ 0 \\ 0 \\ 0 \\ 0 \\ 0 \\ 0 \\ 0 \\ P_p \end{bmatrix} \quad (3.4)$$

The powertrain of the A321appu is characterised by two independent disconnected powertrains with each an independent energy source. Moreover, both energy sources are consumed and are non-rechargeable during the mission. This means that while the overall methodology described by De Vries et al. [87] might be very well suited to model A321appu, none of the powertrains implemented in the method actually represent the desired configuration. Consequently, a tenth "dual-fuel" disconnected powertrain architecture has been added alongside the existing nine configurations, using the framework explained above. The architecture of the "dual-fuel" powertrain is presented in Figure 3.3.

For modelling the A321appu powertrain, the battery that is part of the secondary powertrain is characterised as a secondary source of energy that provides a certain flow of energy, P_{bat} . During sizing and modelling of the powertrain it is unimportant what this secondary source of energy constitutes. Similarly the secondary electrical machine is merely modelled as a black box that ingests power and with a certain loss factor outputs a power. In the case of the A321appu, the battery represents the liquid hydrogen tank and the secondary electrical machine (EM2) represents the APPU. P_{bat} constitutes a mass flow of liquid hydrogen.

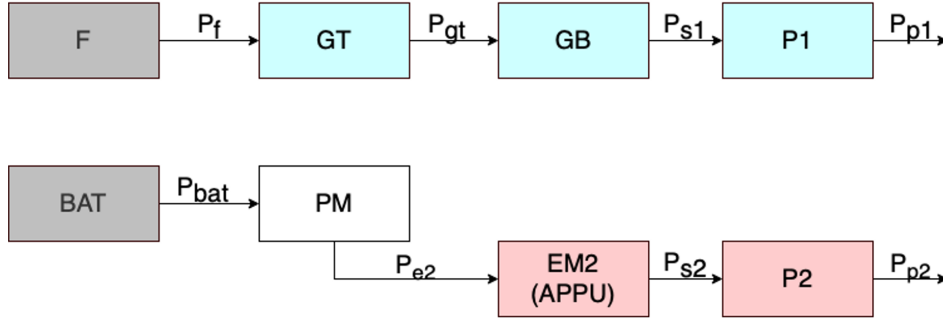


Figure 3.3: Dual-fuel powertrain architecture

In order to be able to reuse the framework of the method by De Vries et al. [87], the new dual-fuel powertrain architecture is also defined as a limit case of the SPPH architecture. To this end, a new powertrain control variable is introduced. This new control variable, ψ , represents the ratio of the power flowing from the gearbox (GB) to the primary electrical machine (EM1), and the sum of the fuel power and battery power, and is defined in Equation 3.5. By setting ψ to 0 the power flowing between the gearbox and the primary electrical machine is set to 0, thereby effectively decoupling the primary and secondary powertrains. In this way, the powertrain presented in Figure 3.3 is obtained from the SPPH-powertrain presented in Figure 3.2.

$$\psi = \frac{P_{gb}}{P_f + P_{bat}} = 0 \quad (3.5)$$

The definition of ψ is chosen so that singularities due to the denominator equating to 0 are mostly avoided. This can only occur when the sum of P_f and P_{bat} is equal to 0, which means either no power is produced or one propulsor is harvesting exactly the amount of energy required to power the other propulsor, or when $P_f = -P_{bat}$. In any of these cases the system is not providing propulsive power to the aircraft. However, this definition of ψ has resulted in an unintuitive parameter that is not usually known to a designer during the conceptual design phase. Consequently, the parameter is only used to decouple the powertrains and has, for the moment, not been added as a possible user input for any of the powertrains.

Implementing ψ in the system of linear equations to solve for the various power paths, results in the system of equations presented in Equation 3.6 for the dual-fuel powertrain, in which the changes with respect to Equation 3.4 are presented in boldface. Moreover, as ψ is always defined to be 0 for the dual-fuel powertrain, the system is effectively a two degree of freedom system. Meaning that the designer has to specify two additional variables. This is also evident from Table 3.1.

$$\begin{bmatrix} -\eta_{GT} & 1 & 0 & 0 & 0 & 0 & 0 & 0 & 0 & 0 \\ 0 & -\eta_{GB} & 1 & 1 & 0 & 0 & 0 & 0 & 0 & 0 \\ 0 & 0 & 0 & -\eta_{P1} & 0 & 0 & 0 & 0 & 1 & 0 \\ 0 & 0 & -\eta_{EM1} & 0 & 1 & 0 & 0 & 0 & 0 & 0 \\ 0 & 0 & 0 & 0 & -\eta_{PM} & -\eta_{PM} & 1 & 0 & 0 & 0 \\ 0 & 0 & 0 & 0 & 0 & 0 & -\eta_{EM2} & 1 & 0 & 0 \\ 0 & 0 & 0 & 0 & 0 & 0 & 0 & -\eta_{P2} & 0 & 1 \\ \Phi & 0 & 0 & 0 & 0 & (1-\Phi) & 0 & 0 & 0 & 0 \\ \boldsymbol{\psi} & 0 & \mathbf{-1} & \mathbf{0} & 0 & \boldsymbol{\psi} & 0 & \mathbf{0} & 0 & 0 \\ 0 & 0 & 0 & 0 & 0 & 0 & 0 & 0 & 1 & 1 \end{bmatrix} \cdot \begin{bmatrix} P_f \\ P_{gt} \\ P_{gb} \\ P_{s1} \\ P_{e1} \\ P_{bat} \\ P_{e2} \\ P_{s2} \\ P_{p1} \\ P_{p2} \end{bmatrix} = \begin{bmatrix} 0 \\ 0 \\ 0 \\ 0 \\ 0 \\ 0 \\ 0 \\ 0 \\ 0 \\ P_p \end{bmatrix} \quad (3.6)$$

When using the dual-fuel powertrain architecture to model the powertrain for the A321appu, the propulsors cannot be used for energy harvesting. This is the result of neither the main engines nor the APPU having the capability to recuperate energy. Moreover, neither of the energy sources are rechargeable during the mission. This behaviour has been ensured by limiting the dual-fuel powertrain to operate at only two of nine possible operating conditions. These two operating conditions ensure that both propulsors are generating thrust and the battery is discharging. Additionally, this limitation further reduces the risk of singularities resulting from the definition of ψ .

Finally, since the secondary powertrain of the A321appu will only feature a single engine, the one engine inoperative (OEI) scenario is only considered with a failure on the primary powertrain. This is the result of a limitation of the method implemented in the Initiator, which cannot model a powertrain without any functioning engines. Moreover, as the APPU is to be a smaller additional engine and is mounted on the aircraft centreline, it will not be the critical engine in a OEI scenario.

3.4. Aircraft Weight Estimation

The first order aircraft weight estimation in the Class I Hybrid sizing method varies considerably from the more conventional Class I weight estimation methods based on weight fractions [87, 92]. A new breakdown of the MTOW and OEW that allows for the modelling of HEDP-aircraft is discussed in subsection 3.4.1. Subsequently, subsection 3.4.2 presents how the OEW is estimated for HEDP-aircraft using conventional reference aircraft and the partial implementation of Class II weight estimation methods. The methods discussed here are implemented in the "Weight estimation" block in Figure 3.1.

3.4.1. Aircraft Weight Breakdown

In a conventional Class I weight estimation the take-off weight (TOW) of the aircraft is often broken down into three components; the fuel weight, the payload weight and operational empty weight (OEW) [89]. Where the payload is often prescribed as a TLAR, the OEW is determined using reference aircraft data, and the fuel weight is computed using the method of fuel fractions in combination with the Breguet range equation. The conventional Class I weight breakdown is presented in Figure 3.4a.

For the modelling of the A321appu an adapted Class I weight breakdown, adapted from the weight breakdown proposed by De Vries et al. [87], is suggested. This weight breakdown is presented in Figure 3.4b and on a high level is divided into the energy weight, the payload weight and OEW. The OEW is defined as the fixed weight of the airframe and aircraft equipment required for the aircraft to perform its mission. Meaning that, in contrast to the proposed breakdown by De Vries et al. [87], the weight of the battery and other energy storage devices such as tanks are considered part of the OEW. The energy weight only includes the variable weight of fuels required for the mission. This revised breakdown allows for the clear distinction between mission variable weight and fixed aircraft weight. In case of a hybrid electric aircraft, the primary fuel will thus fall under the energy weight, while the battery and powertrain weight will be categorised as OEW.

For the A321appu this means that the APPU and the liquid hydrogen tank will be categorised as OEW, while the kerosene and liquid hydrogen will fall under the energy weight group. Take-off weight is then determined by applying Equation 3.7.

$$W_{TO} = OEW + W_{PL} + W_E \quad (3.7)$$

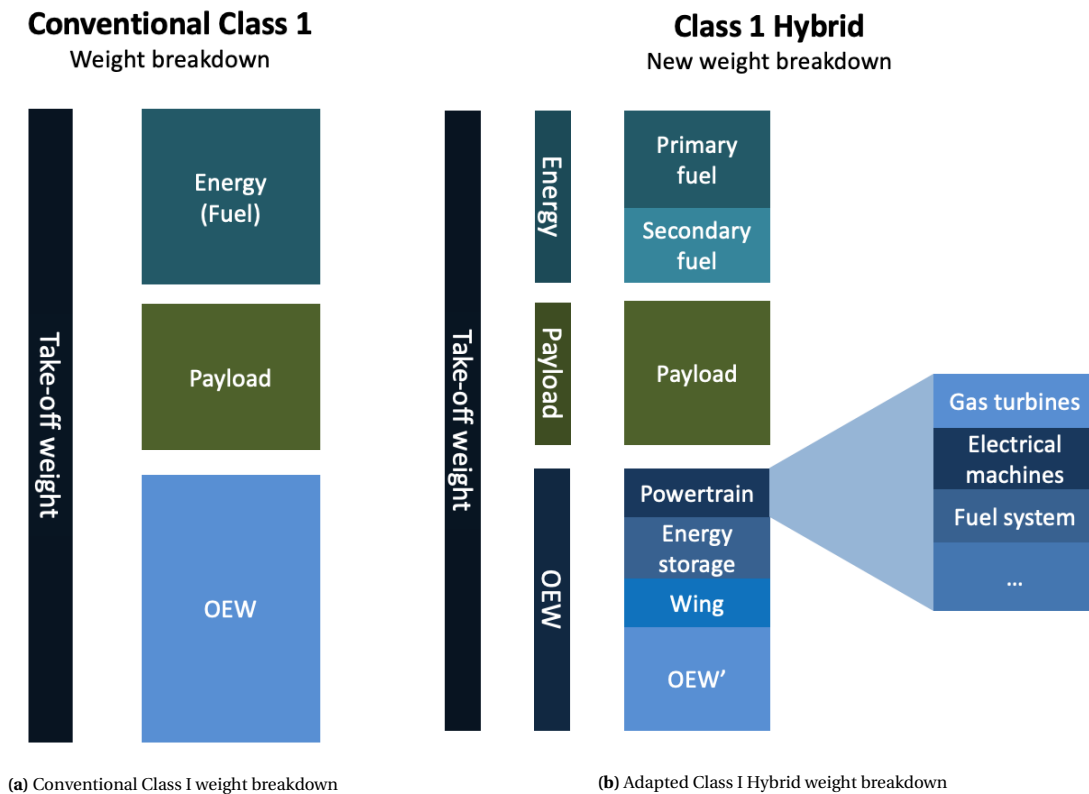


Figure 3.4: Class I weight breakdown, adapted from De Vries et al. [87]

Further changes have been made to the Class I Hybrid sizing routine as suggested by De Vries et al. [87] with regards to the computation of the energy weight using the mission analysis. As the original method was developed solely to design hybrid electric aircraft, the mission analysis only considered decreasing aircraft weight as a result of kerosene consumption. As the consumption of liquid hydrogen also results in a decrease in aircraft weight the missions analysis routine has been adapted to incorporate two sources of fuel being depleted.

Similar to the way in which the consumption of kerosene is derived from the quasi-steady flow of power from the fuel tank, P_f in Figure 3.2, the consumption of liquid hydrogen is computed from the power flow out of the battery, P_{bat} in Figure 3.2. P_{bat} is translated to mass flow of secondary fuel using its gravimetric energy density, $120MJ/kg$ for liquid hydrogen at 1 atm [23]. When an electric secondary powertrain is specified by the designer, the gravimetric energy density is automatically set to 0, and the resulting secondary energy weight will equal 0 kg. The accompanying battery weight will be added to the OEW.

3.4.2. Operational Empty Weight Estimation

As presented in Figure 3.4b the OEW is divided into the weight of the powertrain, energy storage, wing and OEW'. This is in line with the original method by De Vries et al. [87], although the energy storage weight (battery or tank) has been transferred from the energy weight to be part of the OEW.

Conventional Class I methods do not normally include a breakdown of the OEW, and use empirical relations to determine the full OEW based on the TLARs and reference aircraft [89]. However, these empirical relations are not available for hybrid aircraft due to a lack of relevant reference aircraft featuring similar powertrains and aero-propulsive couplings. The specific configuration of the hybrid powertrain might considerably alter the weight of the powertrain, energy storage and the wing, and thereby the OEW.

Consequently, De Vries et al. [87] decided to use the conventional Class I OEW of a conventional reference aircraft with the same TLARs, and refine the weight estimate by recomputing the weight of the powertrain and wing. Meaning that the conventional reference aircraft estimated wing and powertrain weight are subtracted from the OEW to obtain OEW'. Subsequently, the hybrid powertrain weight and recomputed wing weight are

determined based the hybrid aircraft's power- and wing loading, including possible aero-propulsive effects. Next, the energy storage weight is computed based of energy and power requirements obtained from the mission analysis. These three components are finally added to OEW' to obtain the OEW of the hybrid aircraft with possible distributed propulsion, as per Equation 3.8.

$$OEW = OEW' + W_{\text{Powertrain}} + W_{\text{Estorage}} + W_{\text{Wing}} \quad (3.8)$$

The weight of the powertrain can be broken down further to include the weight of each of the components in the powertrain architecture. The weight of the gas turbines is then determined using empirical relations based on a database of turbofan or turboprop engines, dependent on the type of gas turbine to be analysed. The weight of the electrical machines is determined based on a constant power density, which can specified by the designer. The weight of the liquid hydrogen-powered APPU is computed based on the same empirical relations used for the weight estimation of a kerosene-powered turboprop. This simplification is justified by the minor design changes required to convert a kerosene-powered gas turbine to a hydrogen-powered gas turbine [18, 31, 35, 36]. Moreover, the powertrain weight estimation method allows for the easy addition of other engine weight estimation methods in order to accommodate the simulation of engines running on other types of fuel.

The weight estimation of the energy storage is specific to the type of fuel used. The method implemented into the Initiator allows for the easy addition of specific cases and accompanying storage weight estimation methods. The method implemented for the weight estimation of liquid hydrogen tanks is taken from Onorato [58] and will be further elaborated upon in the following section.

The weight of the reference aircraft wing and the re-designed wing including distributed propulsion effect are both determined based on an empirical wing weight estimation method presented by Torenbeek [89] based on the wing loading and the main wing aspect ratio. The re-designed wing the augmented wing loading resulting from the implementation of distributed propulsion is used.

3.5. Liquid Hydrogen Storage Tank Sizing

The sizing of the liquid hydrogen storage tank is implemented in the Class I Hybrid sizing routine and replaces the battery sizing for aircraft featuring liquid hydrogen as a secondary energy carrier. It feeds directly into the "Weight estimation" block of Class I Hybrid workflow diagram presented in Figure 3.1, and is iterated with each iteration of the mission analysis. The tank is sized using the method described by Onorato [58] which is chosen based on its good results, flexibility, and integration into the Initiator. The method is capable of sizing integral and non-integral spherical, cylindrical and conical cryogenic tanks consisting of a thin inner liner and an uniform outer insulation layer. For the A321appu the method is used to design a single non-integral sheared conical tank that is housed in the tailcone of the aircraft behind the rear pressure bulkhead.

The Class I Hybrid mission analysis provides the total liquid hydrogen mass to be stored in the tank, along with the fuel consumption and aircraft flight altitude to the tank sizing module. As the tank is mounted behind the rear pressure bulkhead, the external tank temperature and pressure are determined based on the aircraft altitude using the International Standard Atmosphere (ISA).

The inner tank liner is designed for the stresses incurred by the internal tank pressure. The critical load case is an internal pressure equal to the venting pressure of 2.5 bar at the maximum flight altitude. The liner is sized using Barlow's equation, presented in Equation 3.9, in which $(P_{\text{vent}} - P_{\text{amb}})$ represents the pressure difference across the liner, r_{liner} is the radius of the liner, σ is the maximum allowable stress of the liner material, and e_w is a safety factor set to 0.8. The inner liner is made out of 2019-T851 aluminium alloy, in line with Onorato [58] and Verstraete et al. [51].

$$t_{\text{liner}} = \frac{(P_{\text{vent}} - P_{\text{amb}})r_{\text{liner}}}{\sigma e_w} \quad (3.9)$$

The homogeneous insulation layer is sized using a convergence loop based on the homogeneous thermodynamic model by Lin et al. [93]. In the model the pressure in the tank is modelled using Equation 3.10, assuming both liquid and gaseous phases of hydrogen at uniform temperature equal to the saturation temperature at the internal tank pressure. In the equation ϕ represents the energy derivative defined in Equation 3.11,

and V is the volume of fluid in the tank. Moreover, Q_w represents the rate of heat entering the tank and is determined using Equation 3.12, W_{mix} is the work done on the fluid to reduce stratification, m_g is the mass flow of gaseous hydrogen vented from the tank, m_l is the flow of liquid hydrogen consumed by the engine(s), h_{lg} is the latent heat of vaporisation, ρ_g is the density of the gaseous hydrogen, and ρ_l is the density of the liquid hydrogen. From Equation 3.11 it is evident that the energy derivative is determined based on the mean density between the liquid and gaseous phases of hydrogen in the tank, ρ_{mean} , and the partial derivative of the internal energy, u , to the tank pressure P at the mean density. The method of determining each of these values and derivatives, as well as their specific implementation is presented in detail by Onorato [58].

$$\frac{dP}{dt} = \frac{\phi}{V} \left[Q_w + W_{\text{mix}} - m_g h_{lg} \left(1 + \frac{\rho_g}{\rho_l - \rho_g} \right) - m_l h_{lg} \left(\frac{\rho_g}{\rho_l - \rho_g} \right) \right] \quad (3.10)$$

$$\phi = \frac{1}{\rho_{\text{mean}} \left(\frac{\partial u}{\partial P} \right)_{\rho_{\text{mean}}}} \quad (3.11)$$

The inflow of heat into the tank, Q_w , is estimated using Equation 3.12 for heat conduction across a flat plate of thickness t_{ins} , based on the ambient temperature at altitude, T_{amb} , the temperature of the fuel, T_{fuel} , the outer surface area of the tank, A , and thickness of the insulation material, t_{ins} . The thermal conductivity of the insulation layer, k_{ins} , is determined based on the mean temperature across the insulation between the internal and external tank temperature [58].

$$Q_w = \frac{(T_{\text{amb}} - T_{\text{fuel}}) k_{\text{ins}} A}{t_{\text{ins}}} \quad (3.12)$$

The insulation layer for the A321appu is modelled with a thermal conductivity, k_{ins} , of 0.01 W/mK and a density of 45 kg/m³. These values are chosen as a balance between the values for foams, aerogel blankets, aerogels and multi-layer insulation systems. The chosen thermal conductivity is around 50% lower than those observed for aerogel blankets and foams, while being an order of magnitude higher than those suggested for typical MLIs [49, 51, 55, 94, 95]. The density is in line with current foam and aerogel solutions. The author believes that the chosen values leave ample room for tank insulation innovation before the A321appu's projected entry into service in 2035, without overstretching the capabilities of the sizing method, which was not developed to size MLI systems [58]. The potential of the use of MLI systems has been recognised for years but their implementation has been put-off repeatedly as a result of low technology readiness and the safety risk involved with the breaking of the vacuum [49, 51, 54, 55]. Hence, the balance of insulation properties allows for design and innovation freedom for the A321appu's detailed design, while capturing a rough estimation of the solution's potential performance in the conceptual performance estimation.

The outflow of liquid hydrogen is obtained through the direct consumption of liquid hydrogen by the APPU, obtained from the missions analysis. The venting of gaseous hydrogen when the pressure inside the tank surpasses the venting pressure determines the outflow of gaseous hydrogen. When the pressure in the tank drops below the minimum pressure required to prevent ambient air from entering the tank, the addition of external heat can also be modelled [58].

The tank sizing routine requires the fuselage geometry in order to determine the tank external diameter. However, the fuselage geometry is not available at the first iteration of the Class I Hybrid sizing routine. Consequently, as a first guess a fixed gravimetric efficiency to determine the tank mass is implemented. The gravimetric efficiency is defined as the ratio between the mass of liquid hydrogen stored in the tank to the sum of the mass of the liquid hydrogen stored and the structural mass of the tank, as per Equation 3.13. This gravimetric efficiency is set to 0.72 in line with the work by Winnefeld et al. [49]. In the subsequent sizing iterations the tank is sized using the full tank sizing routine by Onorato [58] as described above.

$$\eta_{\text{grav}} = \frac{m_{\text{LH2}}}{m_{\text{LH2}} + m_{\text{tank}}} \quad (3.13)$$

3.6. Fuel System Sizing

The implementation of the APPU results in an aircraft powered by a combination of two fuels; kerosene and liquid hydrogen. Consequently, the design of the aircraft requires the sizing of two fuel systems.

The mass of the conventional kerosene fuel system is determined using Equation 3.14 by Torenbeek [89]. The relation provides the mass of the fuel system in pounds based on the number of engines on the powertrain, N_e , the number of fuel tanks, N_t , and the total fuel volume, V_f , in US gallons.

$$m_{fs} = 80(N_e + N_t - 1) + 15N_t^{0.5}V_f^{0.333} \quad (3.14)$$

The mass of the cryogenic liquid hydrogen fuel system is determined based on the method by Onorato [58]. The method divides the fuel system mass obtained using Equation 3.14 by a correction factor of 0.5. The correction factor was determined using the detailed design of a liquid hydrogen fuel system by Brewer [29] and was validated using reference data from Silberhorn et al. [96]. A difference of around 2% was found. The total fuel system mass for the aircraft is simply the sum of the masses of the kerosene and the liquid hydrogen fuel systems. This method is implemented because of its simplicity and proven accuracy in estimating the weight of a liquid hydrogen fuel system based on a small number of readily available conceptual design parameters.

3.7. Propulsion System Performance

The performance of the propulsion system is modelled through the efficiency of each of the powertrain components presented in Figure 3.3. The gas turbines, represented by "GT" and "EM2", have a thermal cycle efficiency representing the transmission of power flowing in from the fuel to shaft power. The propulsors of each of the powertrains are modelled using a propulsive efficiency. The primary powertrain will be modelled without a gearbox. Consequently, the efficiency of the gearbox on the primary powertrain is set to 1, thereby effectively bypassing it.

The thermal efficiency of the gas turbine cores is determined using the method presented by Raymer [73] based on the throttle setting of the engine. The thermal performance of the APPU is determined using the same method as that for the kerosene-powered gas turbines, because both types of engine cores feature very similar thermal performance [31]. In addition, both types of gas turbines can make use of nearly the same turbo machinery, which further supports the argument that the core performance can be determined using the same method [18, 35, 36].

The propulsive efficiency for the APPU propulsor is defined as the sum of the propeller efficiency of the isolated propulsor and the change in propulsive efficiency as a result of BLI, as presented in Equation 3.15. The latter will be elaborated upon in Section 3.8, while the former is discussed here.

$$\eta_{\text{propulsive}} = \eta_{\text{propeller,iso}} + \Delta\eta_{\text{propulsive,BLI}} \quad (3.15)$$

It should be noted that the term propulsive efficiency in this study, and in the framework of the Class I Hybrid sizing within the Initiator, refers to the efficiency of the propulsor blocks in Figures 3.2 and 3.3. It is defined as the ratio between shaft power and propulsive power, as presented in Equation 3.16.

$$\eta_{\text{propulsive}} = \frac{P_{\text{prop}}}{P_{\text{shaft}}} \quad (3.16)$$

The A321appu propulsor is modelled after the six-bladed Hamilton-Sundstrand F568 propeller featured on the ATR72 [97]. The original propeller has a diameter of 3.9 m and features highly swept blades. The geometry of one of the propeller blades is implemented in the Initiator using a coordinate file. For use with the APPU, the propulsor is scaled based on the required propulsive power and a representative disk loading. The number of blades is increased to 10, in an effort to improve propeller performance at very high advance ratio [74]. This specific propeller is chosen for its modern design with highly swept blades, making it more suitable for use at higher Mach numbers. Moreover, the original diameter of the propeller is likely to be similar to that required for use with the APPU. The use of a counter-rotating open rotor is discarded following the limited space available in the tailcone and the increased mechanical complexity over a single rotating propeller.

The propeller efficiency of the isolated propulsor is determined based on Actuator Disk Theory using Equation 3.17 [98]. In the equation T_c is the thrust coefficient of the propeller defined as $T_c = T / (\rho v^2 D_p^2)$, where T is the propulsor thrust, v is the free stream flow velocity and D_p is the diameter of the propeller. The correction factor, k_{prop} , is set to 0.88 based on the work of Zamboni [99], who tuned the correction factor using the reference propeller efficiency data for the F568 propeller as presented by Filippone [97].

$$\eta_{\text{propeller,iso}} = k_{\text{prop}} \frac{2}{1 + \sqrt{1 + \frac{8T_c}{\pi}}} \quad (3.17)$$

This method of determining the propulsive efficiency is used as a result of its ability to model the performance of a modern propeller, like the Hamilton-Sundstrand F568, accurately based only on the thrust coefficient [99]. Additionally, no relevant reference data is available for similar propulsors operating at advance ratios close to the cruise operating advance ratio of 5.1 of the APPU propulsor. The effect of the selection of this method on the results is discussed in Section 5.2.

3.8. Boundary Layer Ingestion Modelling

The Initiator incorporates an engineering method that is capable of estimating the first order effects of the implementation of BLI on the propulsive efficiency of the BLI propulsor and on the zero-lift drag of the fuselage. The method is described by De Vries et al. [98] and was developed to support the conceptual design of aircraft, where many geometrical parameters are unknown and computational resources are limited. It is for this reason that the method by De Vries et al. [98] is used for this study above a multitude of other BLI performance estimation methods [69].

Within the Initiator the method is implemented in the Class I Hybrid sizing routine, as part of its distributed propulsion capabilities, and is used to assess the effect of BLI both for the performance constraint diagrams and for the mission analysis. In the method the effect of the fuselage on the inflow of the propulsor is captured as an augmentation of the propulsive efficiency, as per Equation 3.15. The equation presents the total propulsive efficiency, as defined in Section 3.7, as the sum of the isolated propeller efficiency and the increase in propulsive efficiency resulting from the implementation of BLI. The effect of the propulsor on the fuselage pressure field and boundary layer profile is captured in a change of the fuselage zero-lift drag, as described in Equation 3.18 [98]. Secondary effects - the effect of the altered fuselage flow field on the inflow of the propulsor - are neglected. Moreover, the method models the propulsor as an actuator disk with no swirl mounted to the tip of the simplified axisymmetric body as presented in Figure 3.5 [88, 100].

$$C_{D0_{\text{fuselage}}} = C_{D0_{\text{fuselage,iso}}} + \Delta C_{D0_{\text{fuselage,BLI}}} \quad (3.18)$$

The fuselage boundary profile is described by Equation 3.19 based on the experimental work by Della Corte conducted on the setup presented by Lv et al. [101] in the framework of the CENTRELINE project [102]. In Equation 3.19 u is the local flow velocity along the fuselage, U_{edge} is the flow velocity along the fuselage at the edge of the boundary layer, and y is a local coordinate representing the distance to the fuselage skin. The ratio between the boundary edge velocity and the free stream velocity, and the ratio between the boundary layer thickness and fuselage length are determined based on methods from ESDU 78037 [103] and ESDU 79020 [104], respectively.

$$\frac{u}{U_{\text{edge}}} = \frac{0.7848y^4 - 2.1y^3 + 0.9676y^2 + 1.227y + 0.1193}{0.9987} \quad (3.19)$$

The change in propulsive efficiency is determined by modelling the propulsor as an equivalent free-stream actuator disk with augmented equivalent average inflow velocity and equivalent average static pressure as a result of BLI measured at the location of the BLI propulsor. The average equivalent inflow velocity is computed using the boundary layer profile presented in Equation 3.19. The average static pressure is taken as the pressure coefficient on the fuselage at the propulsor location, augmented with the effective velocity increase over the BLI propulsor that is assumed to be isentropically expanded to ambient pressure downstream of the propulsor. The change in propulsive efficiency is then obtained by employing the same method to find the isolated propeller efficiency, as presented previously in Equation 3.17 [88, 98, 100].

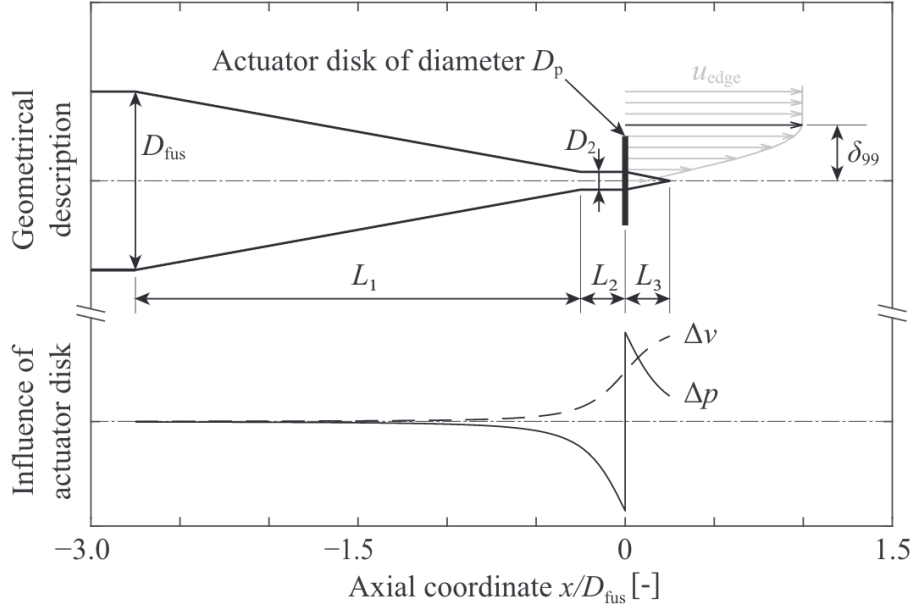


Figure 3.5: Simplified tailcone geometry used for estimating the effect of BLI by Hoogreef et al. [88]

The effect of BLI on the zero-lift drag of the fuselage is further split into two components; a change in skin-friction drag resulting from an altered boundary layer profile and boundary layer edge velocity, and a change in pressure drag originating from reduced pressure recovery over the aft fuselage. The change in skin-friction drag is modelled through an augmentation of the boundary layer edge velocity as a result of the BLI propulsor, while the boundary layer profile and thus the skin friction coefficient are assumed to remain unchanged. The change in pressure drag is computed using a relation by Durand et al. [105] that gives the difference in static pressure between propeller-on and propeller-off conditions. Both terms, for the change in friction drag and the change of pressure drag, can be integrated along the simplified axisymmetric tailcone geometry, as presented in Figure 3.5, to obtain Equation 3.20 [100]. In the equation $c = (D_p/D_{fus})/(2l_{TC})$, D_p is the propulsor diameter, D_{fus} is the fuselage diameter, $T_{c,iso}$ is the thrust coefficient of the isolated propulsor, AR is the aspect ratio of the main wing, b is the span of the main wing, and l_{TC} is the slenderness ratio of the tailcone.

$$\Delta C_{D0} = T_{c,iso} AR \left(\frac{D_{fus}}{b} \right)^2 \left[1 - \sqrt{1+c^2} - c^2 \ln \left(\frac{\sqrt{1+c^2}-1}{c} \right) \right] \quad (3.20)$$

Upon validating the method against the experimental data obtained by Della Corte using the test setup as described by Lv et al. [101], De Vries [100] concludes that the model captures the increase fuselage zero-lift drag well, while the gain the propulsive efficiency underestimated. The discrepancy was found to be larger at lower reference thrust coefficient. The agreement between the model and the experimental data improved at higher thrust settings. Concluding, the model is able to capture the increase in fuselage drag well but the prediction of the change in propulsive efficiency is conservative at low T_c^{ref} [100].

3.9. Design Studies

The methods presented above are implemented into the Initiator as described. Subsequently, the Initiator is used to generate a reference aircraft based on the TLARs presented in Table 3.2. The reference aircraft is a close representation of the Airbus A321neo designed using the same design methods as those used for the A321appu. The A321appu is then be designed based on the reference aircraft, with a number of design changes incurred by the implementation of the APPU. The external geometry of the tailcone remains unchanged in an attempt to model the APPU implementation as a potential retrofit of the A321neo. The Initiator input files are presented in Appendix A and Appendix B for the reference aircraft and the A321appu, respectively. The results of the two design studies, and the differences between the reference aircraft and the A321appu are presented in Chapter 4, and subsequently discussed in Chapter 5.

Table 3.2: Top level aircraft requirements

Requirement	Unit	Value
Range at maximum payload	km	4,630
Maximum payload mass	kg	25,300
Maximum range	km	6,900
Maximum number of passengers	#	202
Cruise Mach number	-	0.78
Maximum operating Mach number	-	0.82
Cruise altitude	m	11,278
Compliance	-	FAR-25
Scrape angle at MTOM	°	12
Maximum take-off run at MTOM ISA sea-level	m	2,330
Maximum landing distance at MLM ISA sea-level	m	1,577
Maximum final approach speed	kts	70
Aerodrome compatibility	-	FAA-IV

4

Results

This chapter presents the results of the design studies that were performed. First, the reference aircraft design is introduced in Section 4.1. Subsequently, the effects of modifying the reference aircraft with an APPU are presented for various shaft power distributions in Section 4.2. Section 4.3 presents the design of APPU configuration resulting in lowest total mission energy consumption. Finally, the performance of the various propulsors fitted to the A321appu and the effect of their performance on performance of the aircraft is shown in Section 4.4.

4.1. Reference Aircraft

The reference aircraft design is shown in Figure 4.1. The aircraft is around 44 m long and has a fuselage diameter of 3.9 m. The total height of the aircraft is roughly 12.5 m. Moreover, the aircraft features two turbofan engines with a bypass ratio of 11 that produce 122 kN of maximum sea level thrust each. The aircraft wing span is 35m and the winglets have a span of 2.4 m. The aircraft has maximum take-off mass (MTOM) of 92.5 tons and an operational empty mass (OEM) of 48.5 tons. More detailed information on the aircraft's weights and performance indicators is presented in Table 4.1.

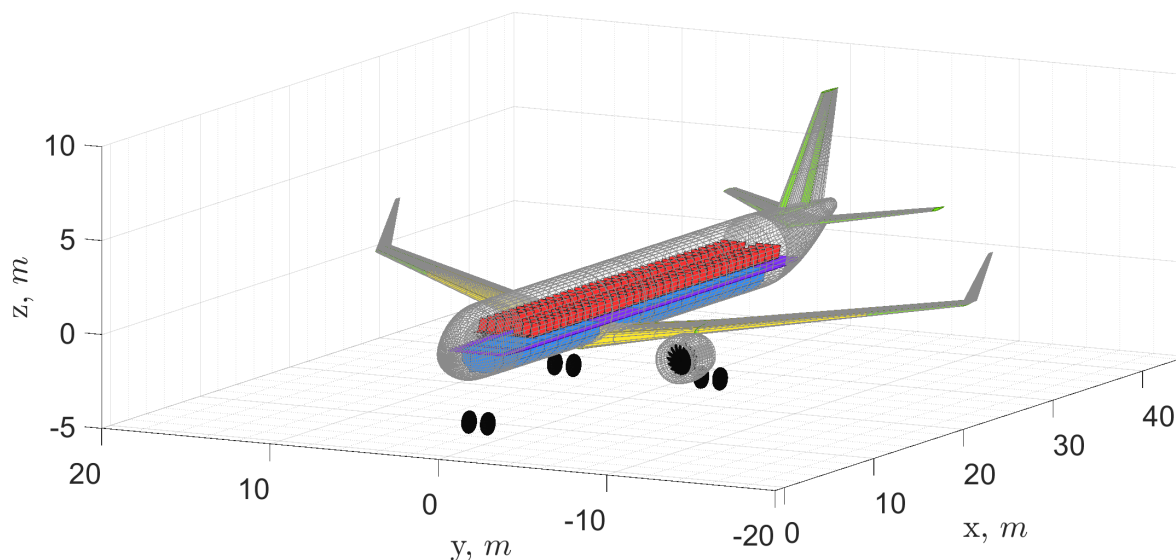


Figure 4.1: Reference aircraft with landing gear struts extended

The aircraft masses are all within 1% of those reported for the A321neo in the Airport Planning Manual [106] and by Janes aircraft database¹. The outer dimensions of the aircraft are all within 10% of those reported.

¹Airbus A321 on Jane's all the world's aircraft. <https://customer.janes.com/Janes/Display/jawa0419-jawa>, accessed 14th of February 2022

4.2. The Effect of Adding an APPU

The modifications made to the reference aircraft are presented in Figures 4.2 to 4.7. The figures present the A321appu with a cryogenic storage tank in the tailcone, and a third engine and propeller mounted in the place of the conventional APU, providing 10% of the total required shaft power. The aircraft also features a cruciform tail configuration with 4° anhedral on the horizontal stabiliser. Moreover, the aircraft has smaller main engines and the same fuselage length and diameter.

From Figure 4.2 and Figure 4.3 it is evident that the horizontal stabiliser has been placed on the vertical stabiliser right above the APPU propulsor. Additionally, it can be seen that the main engines of the APPU-equipped aircraft have shrunk in size compared to the reference aircraft. The figures also highlight the change from positive dihedral on the horizontal stabiliser for reference aircraft to negative dihedral on the A321appu. This change has been made to increase the flutter speed of the horizontal stabiliser and thereby limit the increase in structural mass of the vertical stabiliser [107].

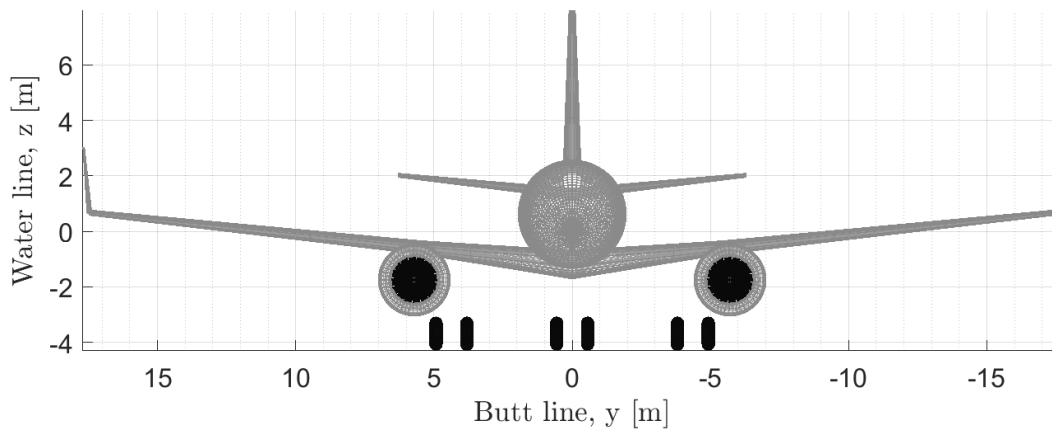


Figure 4.2: Reference aircraft front view with landing gear struts extended

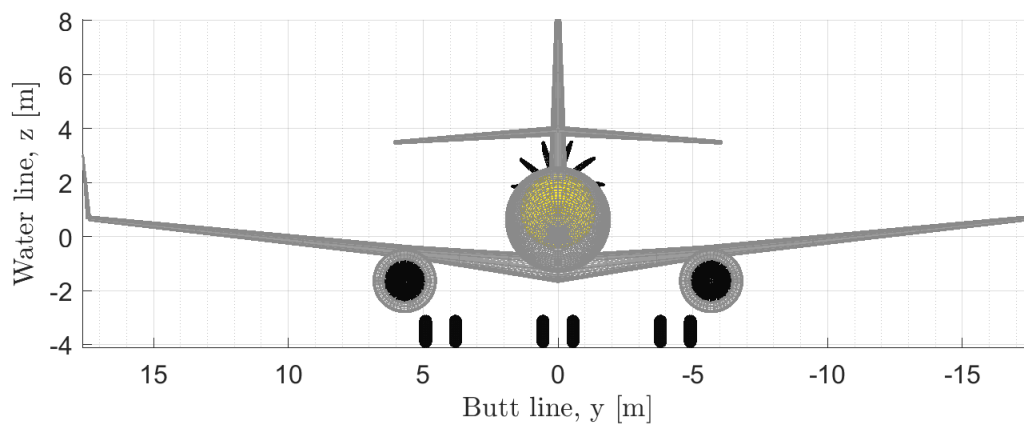


Figure 4.3: A321appu front view with landing gear struts extended

From Figure 4.4 and Figure 4.5 it can be seen that the main wing has shifted rearwards as a result of the introduction of the APPU. Additionally, it is clear that the 12° take-off rotation angle with landing gear struts extended has been maintained. The 3.44 m diameter APPU propeller stays within the tailcone scrape envelope, thereby not limiting the take-off angle compared to the reference aircraft.

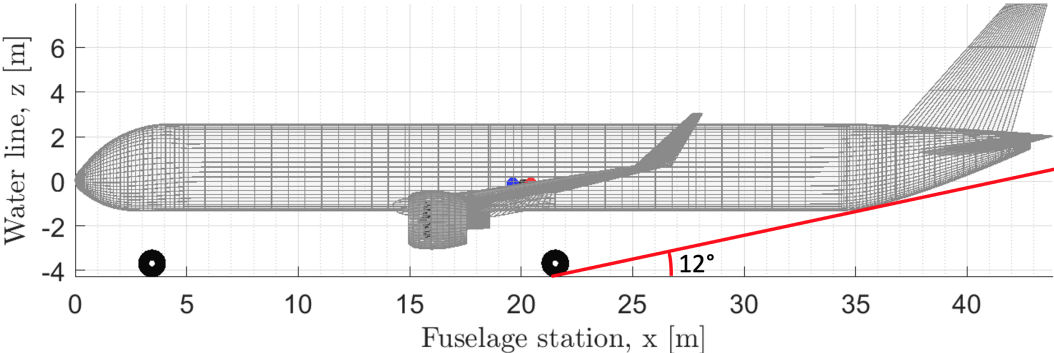


Figure 4.4: Reference aircraft side view with landing gear struts extended

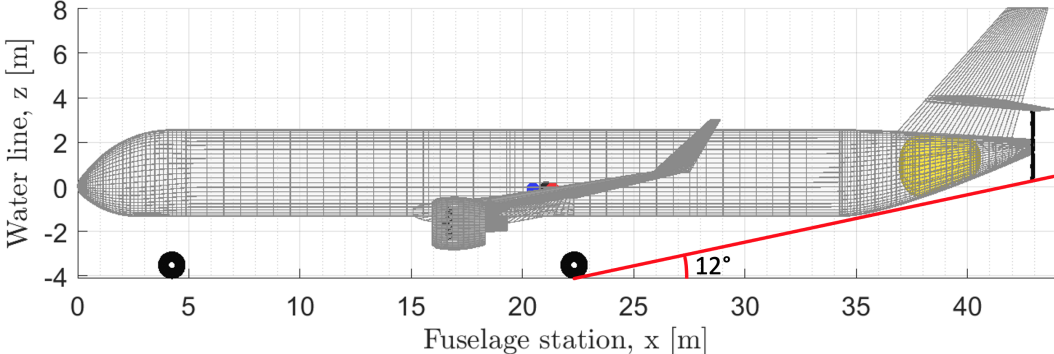


Figure 4.5: A321appu side view with landing gear struts extended

Figures 4.6 and 4.7 present the top view of both aircraft. These figures mostly highlight the similarity between the reference aircraft and APPU-equipped aircraft. The main wing planform has remained largely unchanged and the fuselage is the same across both aircraft. From the figures it is also evident that the main engines have reduced in size considerably.

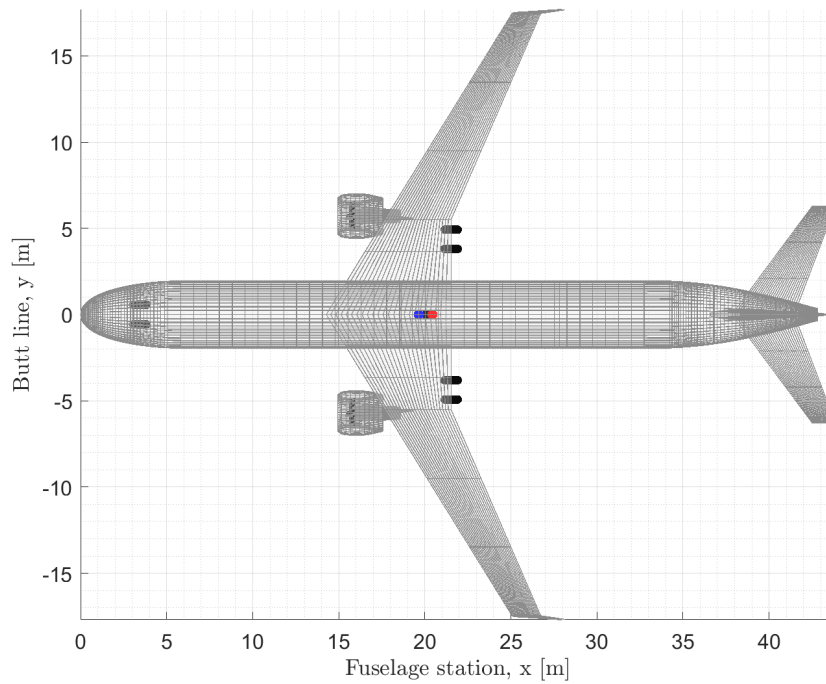


Figure 4.6: Reference aircraft top view with landing gear struts extended

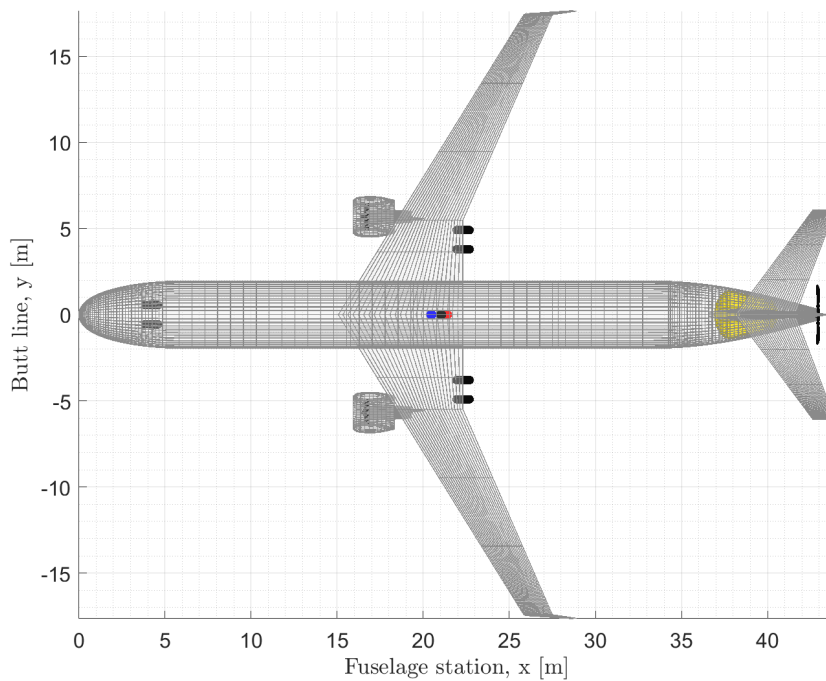


Figure 4.7: A321appu top view with landing gear struts extended

The modifications presented above have been made to the reference aircraft for various APPU shaft power shares, ranging between 2% and 10% throughout all flight phases. For each of these modifications the Initiator redesigned the aircraft using the same methods. Consequently, the modifications are the same for each of the aircraft, however they are applied to a different scale as required to accommodate the APPU. For the aircraft with 2% APPU shaft power share, a spherical liquid hydrogen storage tank is designed to fit within the tailcone. This follows from the the small amount of liquid hydrogen required and the resulting very short conical tank length that would lead to high insulation mass. The 10% maximum shaft power share is limited

by the maximum tank size that fits within the tailcone without modifying its external geometry.

The effect of varying the APPU shaft power share on the MTOM of the aircraft is presented in Figure 4.8. In the figure all masses have been normalised using the MTOM of the reference aircraft, represented by 0% APPU shaft power share. The payload mass is equal to the maximum payload mass as presented in Table 3.2, while the fuel mass equates to the sum of the kerosene and liquid hydrogen mass required to complete the maximum range at maximum payload mission. From the figure it is evident the OEM reduces when an APPU is introduced. The OEM is lowest for the lowest APPU shaft power share and subsequently goes up with increasing shaft power share. It can also be observed that the fuel mass is reduced for the APPU-equipped aircraft compared to the reference aircraft. Overall, these changes result in a lower MTOM for the modified aircraft featuring an APPU, though the aircraft featuring 10% APPU shaft power share is close to the break-even point.

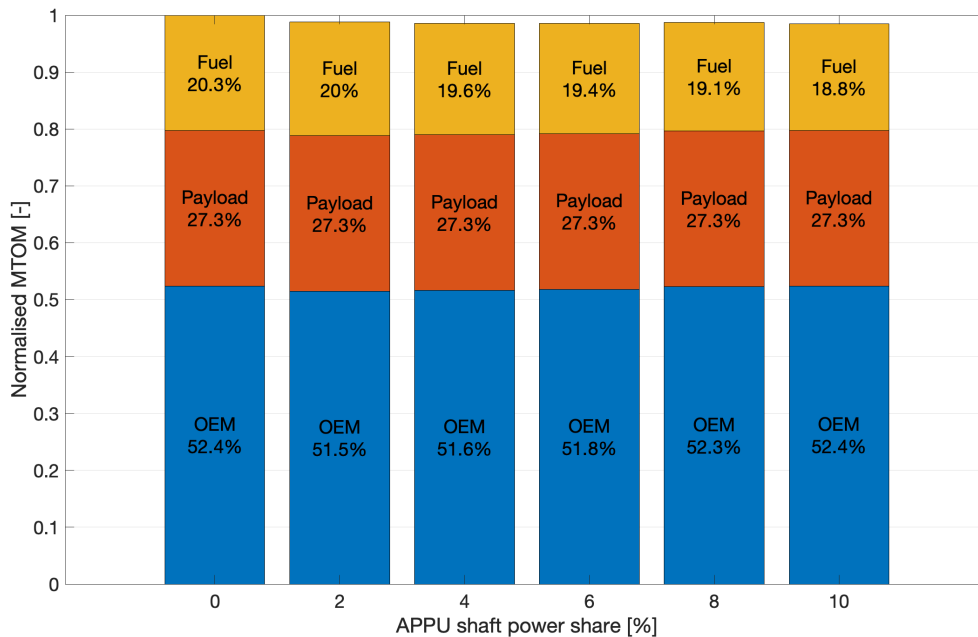


Figure 4.8: Normalised MTOM breakdown for different APPU shaft power shares

Figure 4.9 presents a more detailed breakdown of the normalised OEM, the reference aircraft is represented by 0% APPU shaft power share. In the figure the OEM is broken down into the items that vary in mass by more than 5% as a result of APPU implementation, and the components that show smaller variance with APPU shaft power share. Those components are combined in OEM* and presented in blue at the bottom of Figure 4.9. Note that these components comprise roughly 82% of the OEM. The figure re-emphasises the reduction in OEM when implementing an APPU, reaching a minimum at 2% shaft power share. Moreover, at 10% shaft power share the OEM is nearly equal to that of the reference aircraft. The figure also presents a reduction in horizontal stabiliser mass, an increase in vertical stabiliser mass, and a growing reduction in main engine mass. These are followed by an increasing APPU engine mass, cryogenic storage tank mass and fuel system mass. Furthermore, the removal of the APU results in a considerable reduction in OEM and outweighs the APPU up to 6% shaft power share. This is likely the result of an overestimation of APU mass and will be discussed in greater detail in Section 5.3. Overall the reference aircraft features the highest total engine mass - the sum off main engines, APPU, and APU - of all aircraft presented.

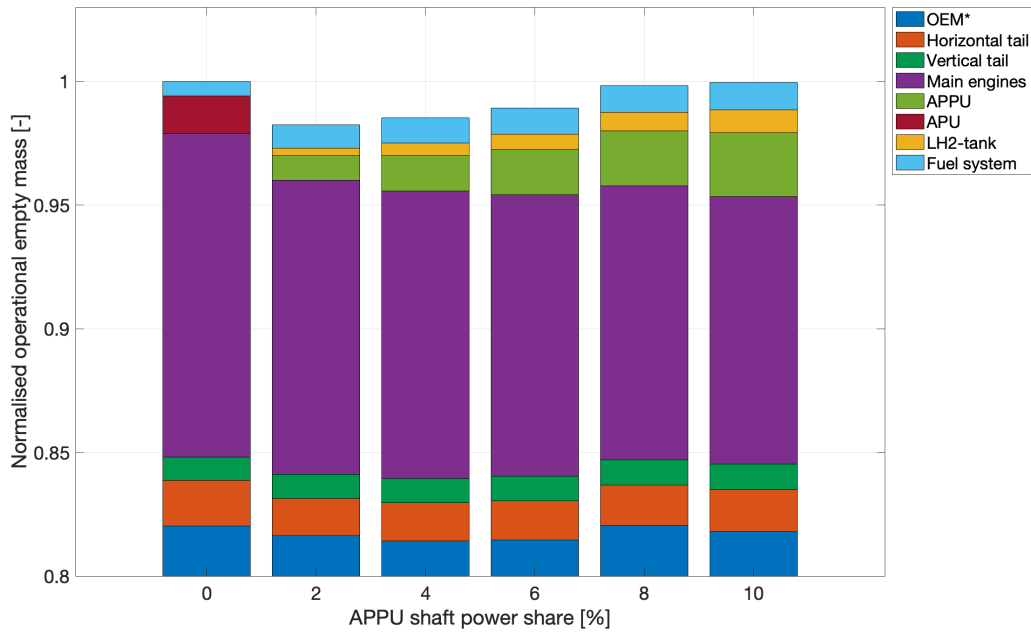


Figure 4.9: Normalised OEM breakdown for different APPU shaft power shares

The conversion of the mission fuel masses with their respective energy densities, as presented in Table 2.1, results in the total mission energy consumption, which for the extended maximum range at maximum payload mission is presented in Figure 4.10 for different APPU shaft power shares. The figure includes the total energy consumption for the aircraft with and without the use of the BLI model. A linear trendline has been fitted to the two data sets. The non-BLI data ($RMSE = 15 \times 10^{-4}$, $N = 5$) shows greater variance than the BLI data ($RMSE = 73 \times 10^{-5}$, $N = 5$), but both show decreasing energy consumption with increasing APPU shaft power share. Moreover, both lines show a reduction in energy consumption with respect to the reference aircraft.

The difference between the two trendlines provides insight in the predicted effect of BLI implementation on the A321appu. The line representing the BLI-enabled aircraft shows a roughly three times stronger reduction in energy consumption compared to the non-BLI line. For most of the shaft power share domain presented, the BLI-enabled aircraft features lower mission energy consumption, with the largest difference occurring at 10% shaft power share and roughly 0.9% lower energy consumption for the BLI-enabled aircraft. Finally, it can be seen that the lowest energy consumption presented results in about 1.3% reduction in total mission energy with respect to the reference aircraft. The trendline presents lower energy consumption for the non-BLI aircraft up to a shaft power share of 1.1%, while the data points show an increase in energy consumption due to BLI up to 2% shaft power share.

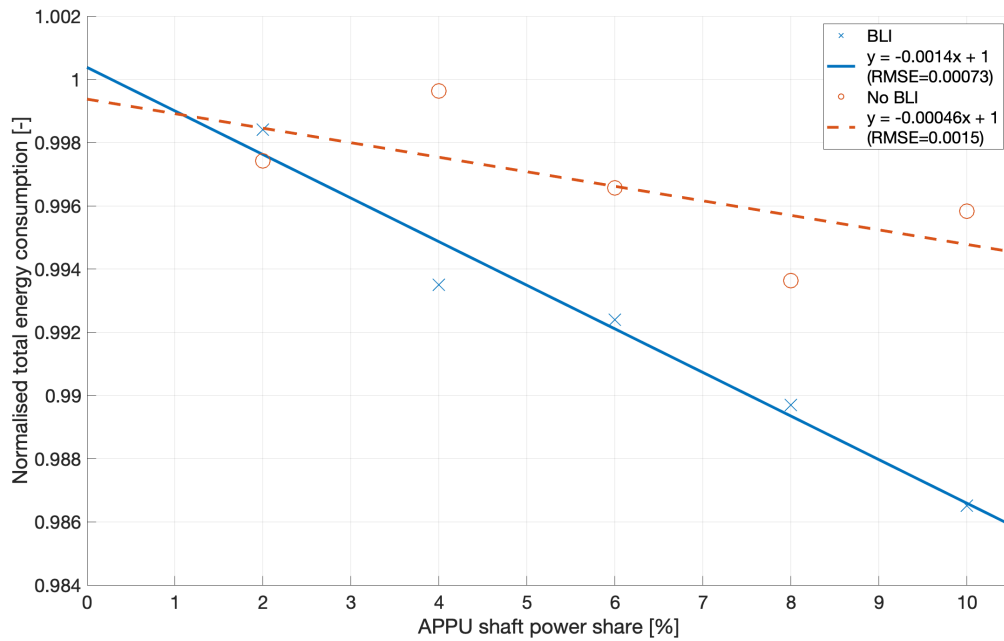


Figure 4.10: Total energy consumption for the extended maximum range at maximum payload mission for different APPU shaft power shares

When converting the mission required liquid hydrogen and kerosene masses into the equivalent greenhouse gas emissions resulting from their combustion, the results presented in Figure 4.11 are obtained. For these results a conversion factor of 3.0 kg/kg kerosene and 0.0 kg/kg of liquid hydrogen have been used for the CO₂-emissions, and 1.24 kg/kg of kerosene and 8.92 kg/kg of liquid hydrogen have used for the emission of H₂O [21, 23, 48]. The resulting CO₂-emissions can be seen to decrease almost linearly ($RMSE = 11 \times 10^{-4}$, $N = 5$) with increasing APPU shaft power share. At 10% power share, the emission of CO₂ is estimated to be reduced by 11% with respect to the reference aircraft on the same mission. In contrast, the emission of water vapour increases almost linearly ($RMSE = 11 \times 10^{-4}$, $N = 5$) with APPU shaft power share, resulting in a maximum of almost 14% increased H₂O-emissions at 10% power share.

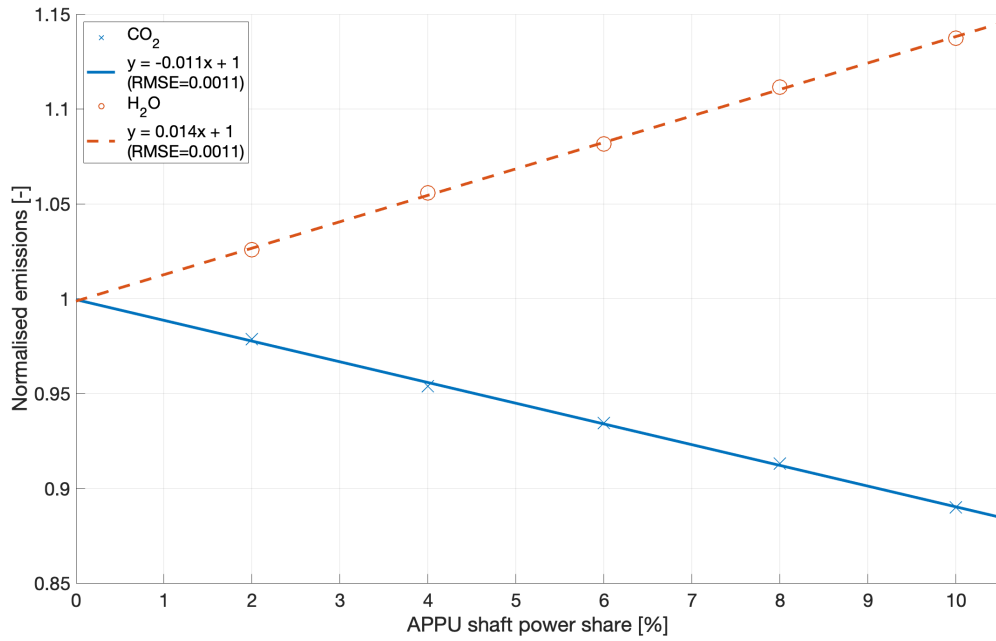


Figure 4.11: Greenhouse gas emissions for different APPU shaft power shares

Finally, Figure 4.12 presents the gravimetric efficiency of the liquid hydrogen storage tank for the different APPU shaft power shares. The gravimetric efficiency of the tank is defined as the ratio of liquid hydrogen mass stored in the tank, over the mass of the liquid hydrogen and the tank itself, as per Equation 3.13 [49]. It can be seen that the efficiency of the tank increases up to a maximum around 9%. Here it must be noted the tank for 2% shaft power share is modelled as a sphere placed into the tailcone while the other tanks are modelled as sheared cones following the contour of the aft fuselage. Increasing the APPU shaft power share requires more liquid hydrogen and thus results in a tank with larger volume while the fuselage diameter is constant. Hence, longer and increasingly pointy tanks are obtained for increasing shaft power share. Overall, the efficiency changes between roughly 48% and roughly 60%.

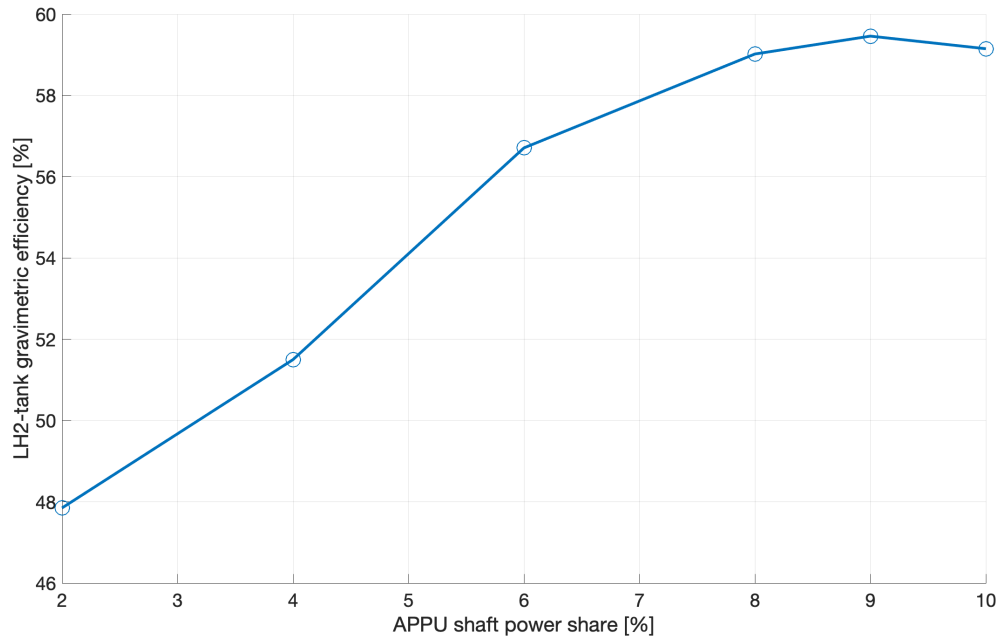


Figure 4.12: Gravimetric efficiency of the liquid hydrogen storage tank for different APPU shaft power shares

From the results presented above it can be concluded that increasing the APPU shaft power share between 2% and 10% reduces the MTOM and increases OEM, while both have reduced with respect to the reference aircraft. Moreover, it is observed that higher APPU shaft power share results in lower mission energy consumption, lower CO₂-emissions and higher H₂O-emissions for the maximum range at maximum payload mission. The addition of BLI results in a further reduction in energy consumption. Consequently, Section 4.3 presents the design of the A321appu with 10% APPU shaft power share and BLI.

4.3. A321appu Design

The design of the A321appu with the APPU providing 10% of the total required shaft power in each of the flight phases is presented in Figure 4.13 and Figures 4.3, 4.5, and 4.7. The aircraft features a 10-bladed 3.44 m diameter propulsive fan, a shifted wing, and a cruciform empennage configuration.

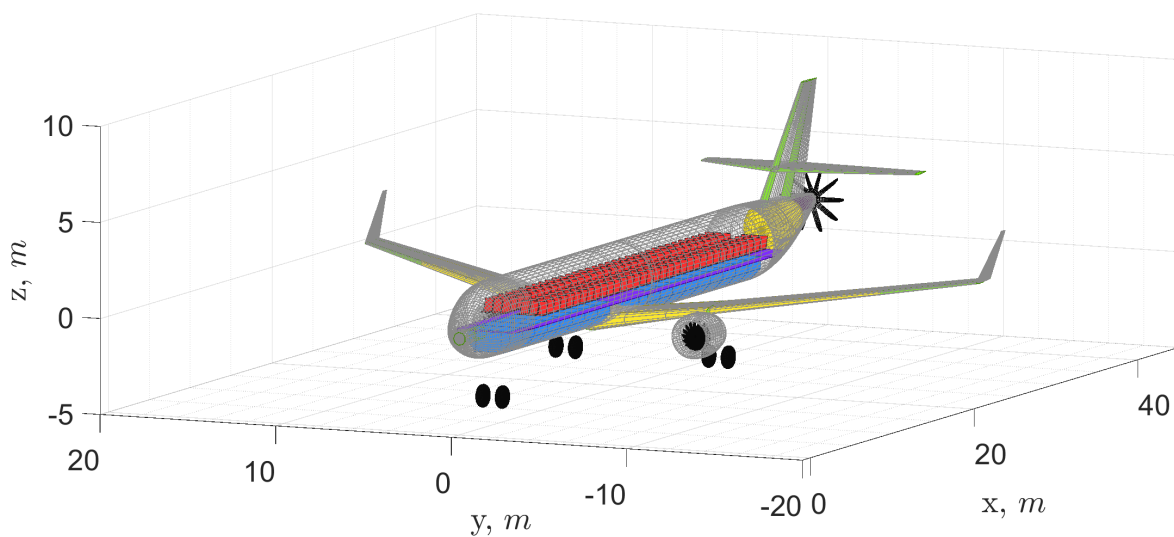


Figure 4.13: A321appu with landing gear struts extended

The weight and performance indicators for the A321appu are presented alongside those for the reference aircraft in Table 4.1. From the table it is evident that the OEM remains virtually unchanged while the MTOM decreases by 2%. The total fuel mass carried for the maximum range at maximum payload mission decreases by 7%, while the overall mission energy consumption decreases by 1.3% for the extended maximum range at maximum payload mission. The A321appu carries an additional 650 kg of liquid hydrogen, a 450 kg liquid hydrogen storage tank, and the APPU which weighs 1255 kg. The secondary fuel system results in an 89% increase in fuel system mass, while the removal of the APU saves around 740 kg. A further 550 kg is saved per main engine following a reduction in required main engine thrust of 17%. A detailed OEM breakdown and a breakdown of the system masses are presented in Figure 4.14 and Figure 4.16, respectively. From Figure 4.14 it is evident that the mass of the APPU, which comprises of the elements presented in Figure 4.15, accounts for 3% of total OEM. Figure 4.15 highlights the considerable mass of the 3.44 m propeller, which makes up 26% of the total APPU engine mass. Moreover, Figure 4.16 shows that the mass of the fuel systems is almost doubled as a result of the secondary cryogenic fuel system. The combined mass of the cryogenic fuel system and the cryogenic storage tank can be seen to make up 11% of the total systems mass. Overall the total APPU-related mass equates to 1957 kg or 4% of the total OEM.

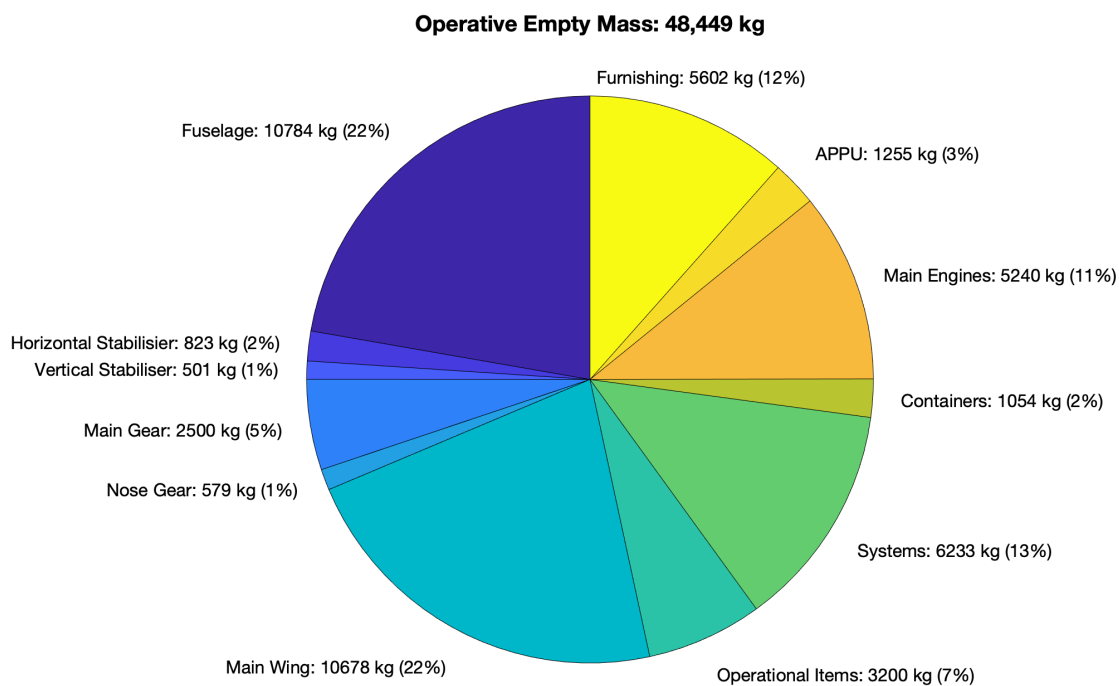


Figure 4.14: A321appu with 10% APPU shaft power share OEM breakdown

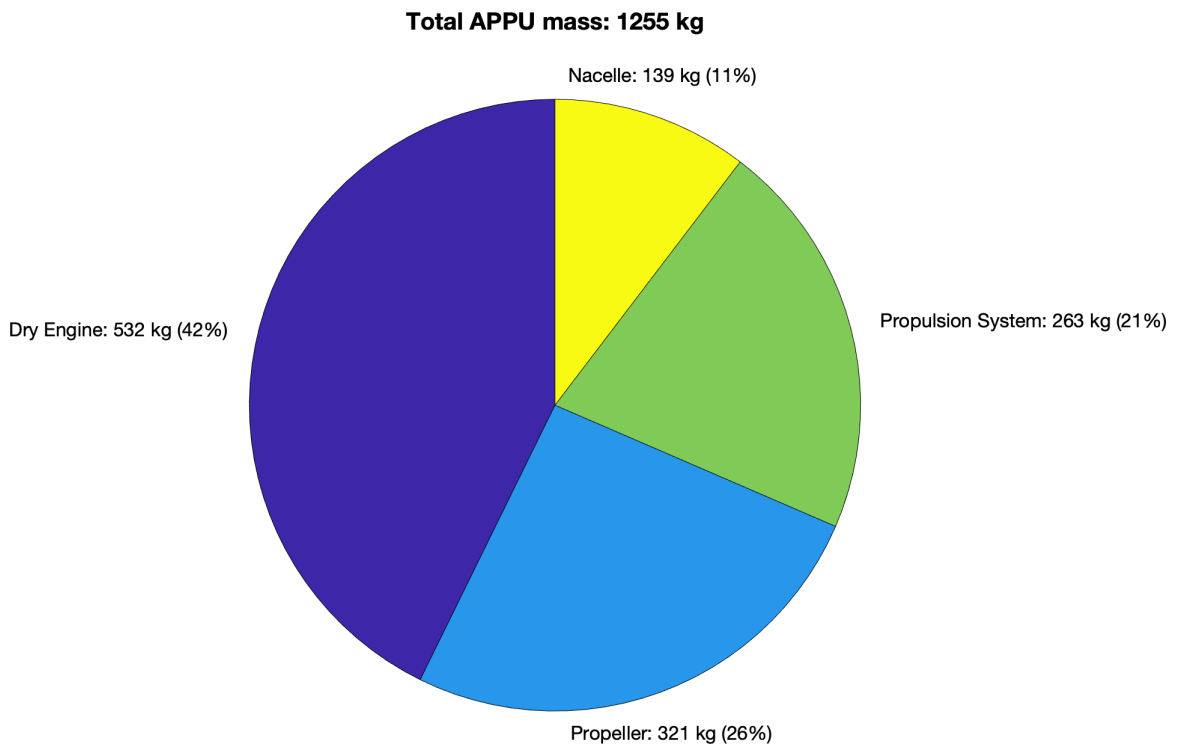


Figure 4.15: APPU engine mass breakdown for 10% shaft power share

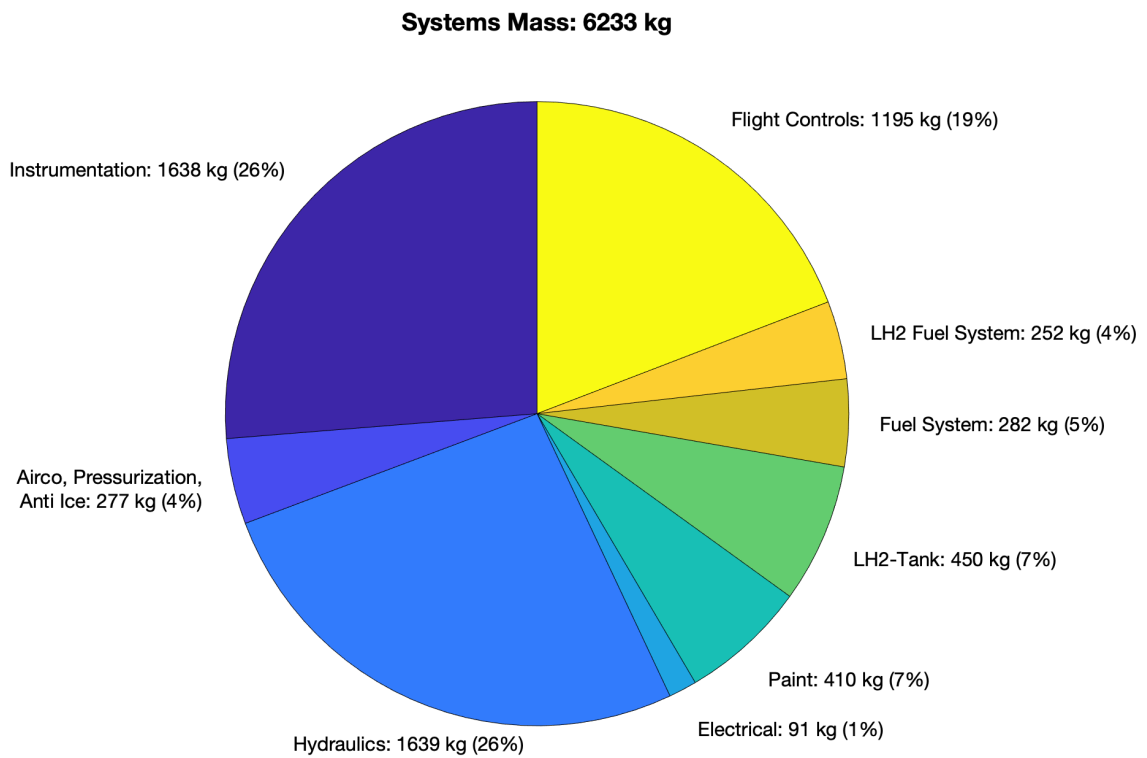


Figure 4.16: A321appu with 10% APPU shaft power share systems mass breakdown

Figure 4.17 presents a detailed overview of the aft-fuselage layout of the A321appu. In the figures it can be seen that the horizontal stabiliser has been moved upwards onto the vertical stabiliser to create space in the tailcone to house the cryogenic storage tank and the APPU engine. The horizontal stabiliser is placed just

above the APPU propulsor to avoid interference while limiting the increase in vertical tail structural mass. The propulsor has been mounted as high as possible in order to enable the required take-off rotation angle. Moreover, the figure presents the roughly 9 m^3 sheared conical liquid hydrogen storage tank in yellow and the APPU engine in purple. All APPU-related components have been mounted behind the rear pressure bulkhead and the external tailcone geometry has not been altered with respect to the reference aircraft. Finally, it can be seen that, while space is tight, there is still room available for the cryogenic fuel system and the APPU intake and exhaust ducts, as well as other support systems.

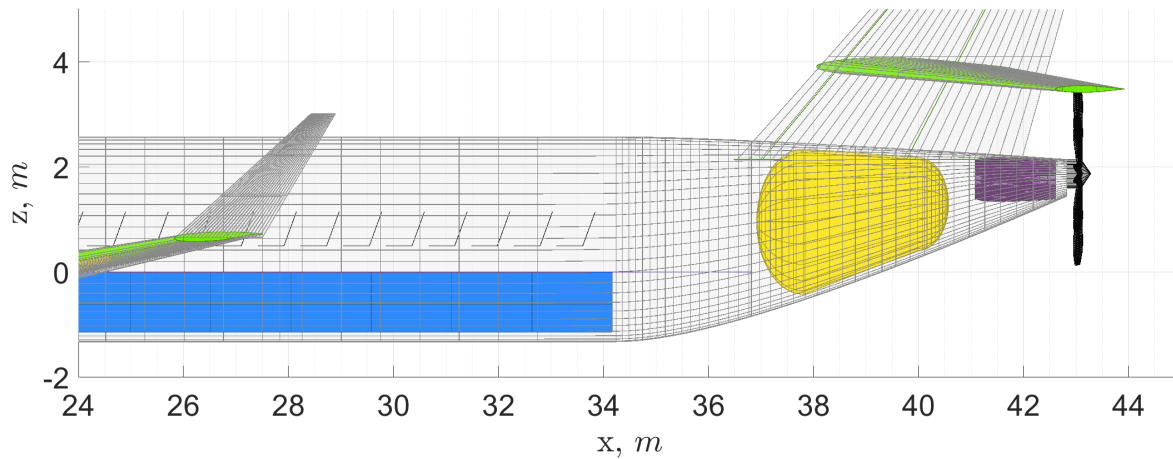


Figure 4.17: Close-up of the A321appu tailcone

A cross section of the roughly 9 m^3 cryogenic liquid hydrogen storage tank for A321appu with 10% APPU shaft power share is presented in Figure 4.18. The tank roughly follows the contour of the aft fuselage and features a 1.8 mm thick aluminium liner wrapped in a 148 mm thick insulation layer. It features a venting pressure of 2.5 bar, weighs 450 kg, and has a maximum capacity of 650 kg of liquid hydrogen. The tank end caps feature a minor-to-major axis ratio of 0.6 as this was found to lead to the highest gravimetric efficiency by Gomez and Smith [108]. The non-integral tank occupies 95% of the fuselage diameter, leaving around 10 cm between the tank and the fuselage skin for fuselage structure and APPU support systems. Furthermore, during the maximum range at maximum payload mission the tank does not require venting or external heating as the pressure slowly increases towards the venting pressure throughout the flight. The tank has a gravimetric efficiency of 59% and is accompanied by a cryogenic fuel system that is estimated to weigh 252 kg.

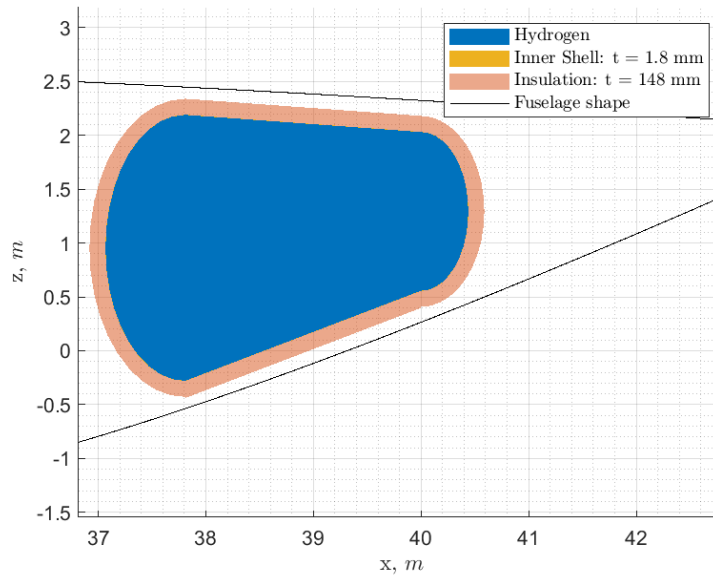


Figure 4.18: Two-dimensional layout of the liquid hydrogen storage tank for 10% APPU shaft power share

The A321appu features the same wing loading as the reference aircraft, however the slight reduction in MTOM results in a roughly 1 m^2 reduction in total main wing area. The main wing has also shifted rearwards by 0.80 m. The horizontal stabiliser is located at 30% of the span of the vertical stabiliser and, as a result has shifted rearward by 0.3 m. The vertical stabiliser sees a 2% increase in surface area and a roughly 10% increase in structural weight as a consequence of the increased structural loading from the cruciform tail arrangement.

Figure 4.19 presents the scissor plot for the A321appu. For clarity the figure only shows the sizing requirements for both the APPU-equipped aircraft and the reference aircraft. From the figure it is evident that the line with positive directional coefficient, which represents the cruise stability power-off requirement, is reduced in slope for the A321appu compared to the reference aircraft. Moreover, it can be seen that the APPU-equipped aircraft features a considerably larger c.g. shift, while the lower slope of the cruise stability line results in an overall roughly 6% decrease in required horizontal stabiliser area to main wing area ratio. Combining this with the minor decrease in main wing area results in a horizontal stabiliser area of 29.5 m^2 , a 7% reduction compared to the reference aircraft.

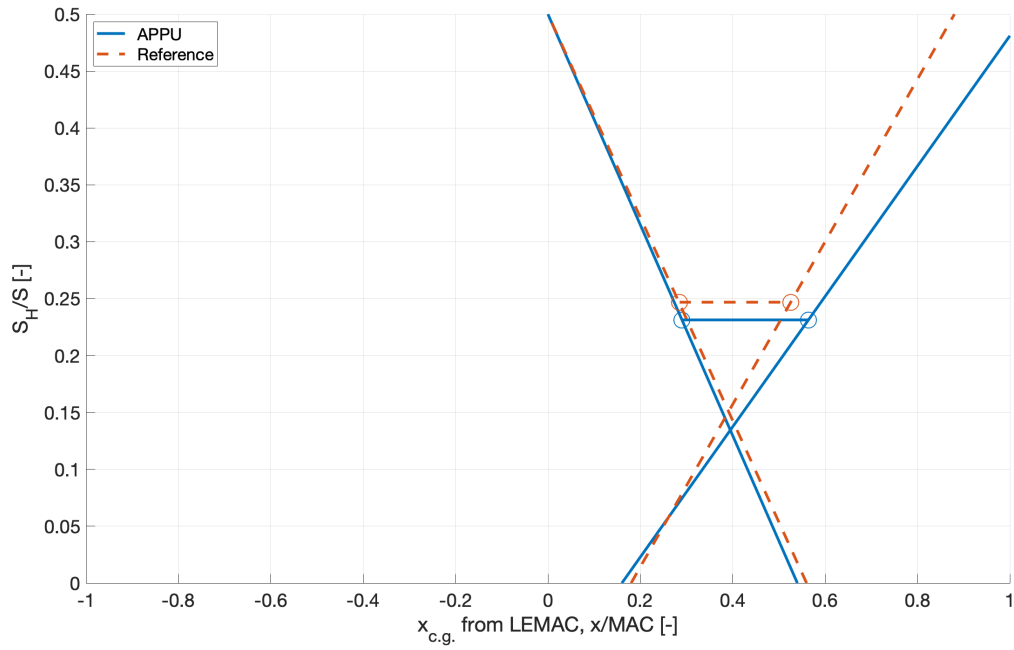


Figure 4.19: Scissor plot comparing the A321appu with 10% APPU shaft power share and the reference aircraft

Figure 4.20 presents the payload-range diagram for the A321appu and for the reference aircraft. From the figure it is most evident that the aircraft have largely the same payload-range capability, as a result of being designed to the same TLARs. It can be seen that the A321appu features a marginal increase in ferry range of 200 km compared to the reference aircraft.

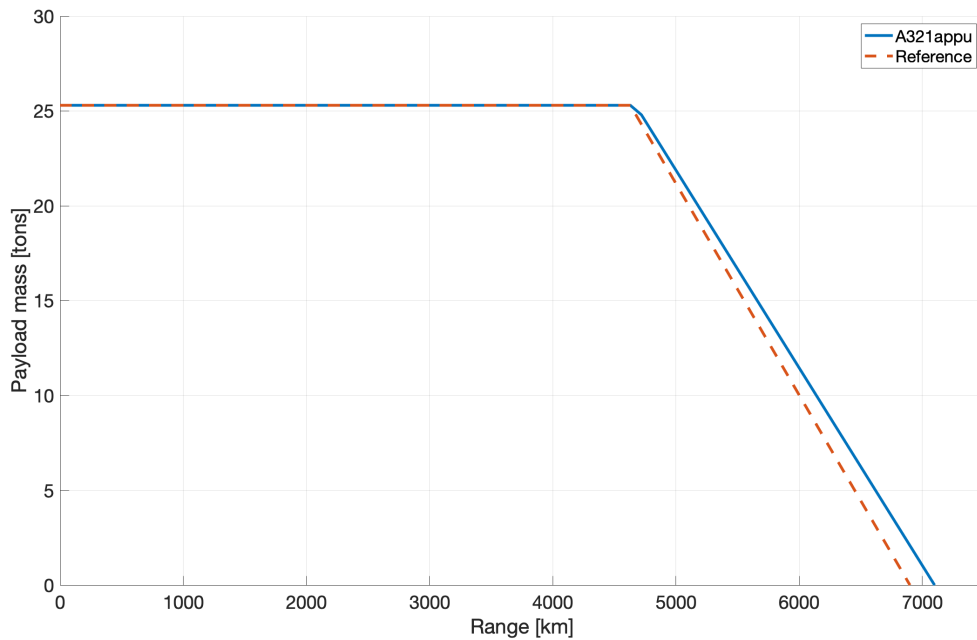


Figure 4.20: Payload-range diagram for the A321appu and the reference aircraft

Figure 4.10 presents a reduction in required mission energy for the extended maximum range at maximum payload mission at an APPU shaft power share of 10%. Figure 4.21 presents the total mission energy required for a number of extended missions and the derived linear trendline ($RMSE = 15 \times 10^{-5}$, $N = 3$). In the figure, the required energy has been normalised with the required mission energy of the reference aircraft to complete the same mission. It is evident that the mission energy savings reduce slightly with increasing range, but is in overall relatively constant. Moreover, it can be concluded that each of the missions have resulted in an energy saving compared to the reference aircraft, and that overall energy savings are around 1.4%.

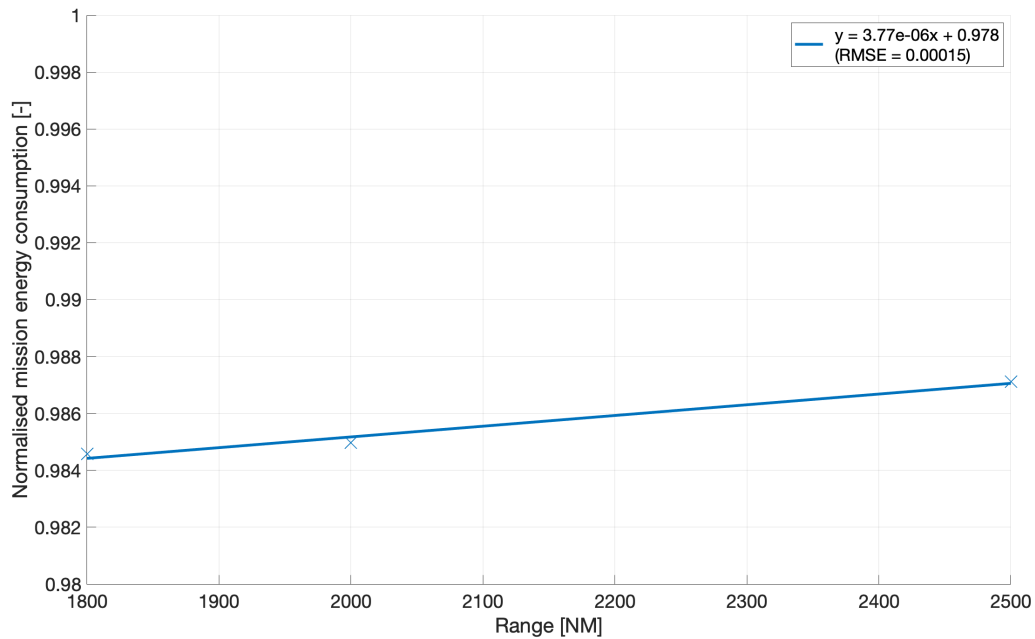


Figure 4.21: Mission energy saving with respect to the reference aircraft

The installed sea-level maximum take-off thrust is also presented in Table 4.1 for both aircraft. It is evident that the total installed thrust reduces by roughly 2% to 238 kN on the APPU-equipped aircraft. Moreover, the APPU can deliver roughly one-third of the thrust of one of the main engines. The emissions of CO_2 and H_2O are predicted to decrease by 11% and increase by 14% as a result of the APPU modification, respectively.

Table 4.1: Aircraft parameters for the APPU-equipped aircraft with 10% APPU shaft power share

Parameter	Unit	Reference	A321appu	Δ
MTOM	tons	92.5	91.1	-2%
OEM	tons	48.5	48.4	0%
Fuel mass	tons	18.8	17.4	-7%
LH2 mass	tons	0	0.7	-
Main engine mass	kg	3169	2620	-17%
APPU mass	kg	0	1255	-
APU mass	kg	739	0	-
Fuel system mass	kg	282	534	+89%
LH2 tank mass	kg	0	450	-
Wing loading	N/m^2	7038	7038	0%
Power loading	N/W	0.0506	0.0505	0%
Total thrust SL TO	kN	244	238	-2%
Main engine thrust SL TO	kN	122	101	-17%
APPU thrust SL TO	kN	0	36	-
Energy consump./RPK	MJ/km	0.87	0.86	-1%
Kerosene consump./RPK	g/km	20.1	17.9	-11%
LH2 consump./RPK	g/km	0	0.7	-
CO ₂ /RPK	g/km	60	54	-11%
H ₂ O/RPK	g/km	24.9	28.4	+14%

4.4. Propulsor Performance

This section will elaborate on the performance of the APPU propulsor. To that end, Figure 4.22 presents the propulsive efficiencies of the main engine propulsors, propulsor 1, and the APPU propulsor, propulsor 2, for various APPU shaft power shares. The main engines can be seen to have a propulsive efficiency of around 79%. The isolated APPU propeller performs between 8% and 9% better, with a propulsive efficiency around 87%. The implementation of BLI increases the APPU propulsive efficiency by a further 9% to around 96%. Note that the propulsive efficiency is defined as the loss factor over the propulsor as presented in Figure 3.3. The total propulsive efficiency of the BLI-enabled propulsor is defined as the sum of propulsive efficiency of the isolated propulsor and the additional performance due to BLI, as per Equation 3.15 [98].

For the 10% APPU shaft power share, the partial ingestion of the fuselage boundary layer results in an increase in propulsive efficiency of 8.4% over the isolated APPU propulsor efficiency of 86.7%. Resulting in a total propulsive efficiency of 95.1%. The implementation of BLI also results in a 1.5 drag counts increase in zero-lift drag. This equates to a 0.8% increase in the zero-lift drag coefficient of the full aircraft in cruise conditions. Overall, this results in a roughly 0.9% reduction total energy consumption as was presented in Figure 4.10, which constitutes the majority of the 1.3% reduction in energy consumption of the A321appu over the reference aircraft.

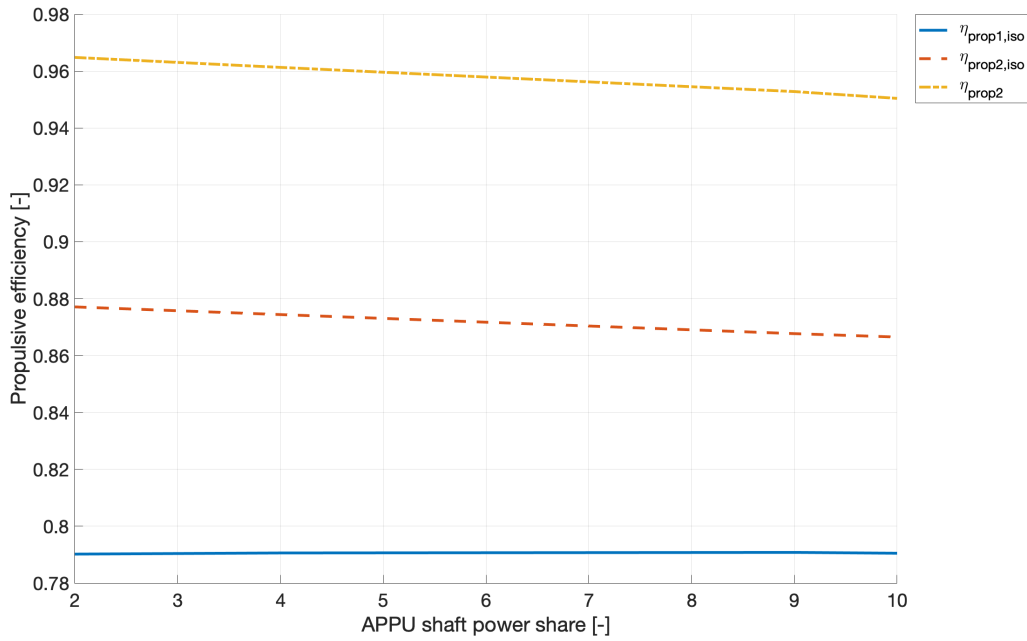


Figure 4.22: Propulsive efficiency of the propulsors for different APPU shaft power shares

During the cruise phase the boundary layer velocity profile that is ingested by the APPU propulsor can be represented by Figure 4.23. This velocity profile is the representation of the expression presented in Equation 3.19 based on the experimental work by Della Corte conducted on the setup presented by Lv et al. [101] in the framework of the CENTRELINE project [102]. During cruise the boundary layer over the rear fuselage is estimated to be 1.21 m thick, while the propulsor has a diameter of 3.44 m on the APPU-equipped aircraft with 10% APPU shaft power share.

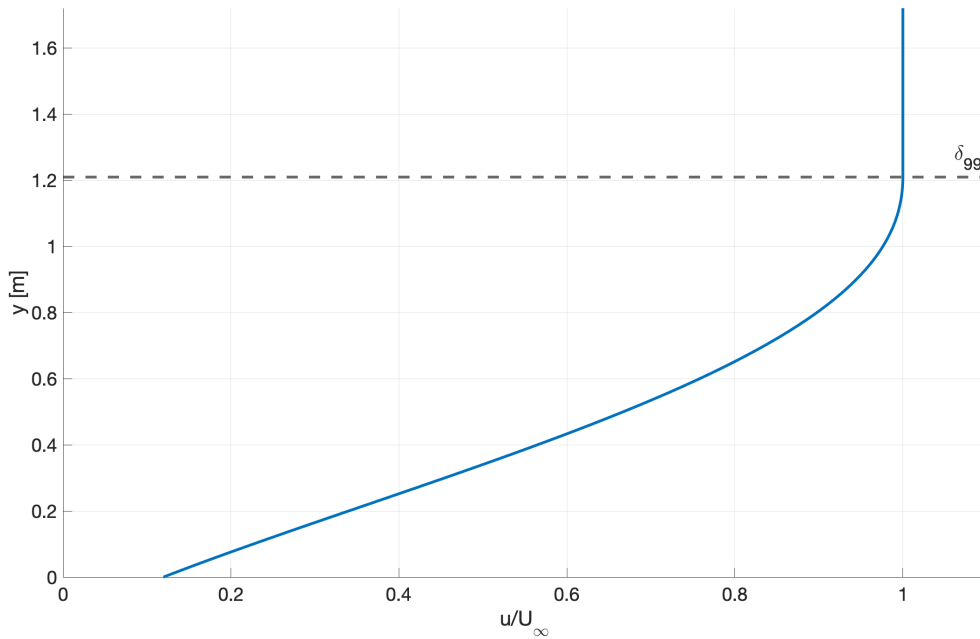


Figure 4.23: APPU propulsor inflow velocity profile

Overall the APPU propulsor features around 16% higher propulsive efficiency than the isolated primary propulsor of the main engines, meaning that the APPU is more efficient at producing thrust than the main engines. Consequently, the energy saving of the APPU-equipped aircraft is strongly dependent on the performance of the APPU-propulsor. This dependency is presented in Figure 4.24, which shows the sensitivity of the total energy consumption during the extended maximum range at maximum payload mission for scaled propulsive efficiencies at an APPU shaft power share of 8%. The scaling factor is multiplied directly with the estimated isolated propulsive efficiency.

The propulsive efficiency has been scaled by 0.98 and 1.02 to simulate a respective 2% decrease and increase. The linear trendline that has been fitted to the data points ($RMSE = 49 \times 10^{-5}$, $N = 3$) can be seen to have a slope of -1.3. This indicates that a one percent decrease in propulsive efficiency results in a 1.3% increase in energy consumption. It must be noted that for a similar decrease in propulsive efficiency would result in a liquid hydrogen storage tank volume that is too large to fit into the tailcone at 10% APPU shaft power share. In fact, a one percent decrease in propulsive efficiency for 10% APPU shaft power share results in a tank volume that exceeds the size of the tailcone.

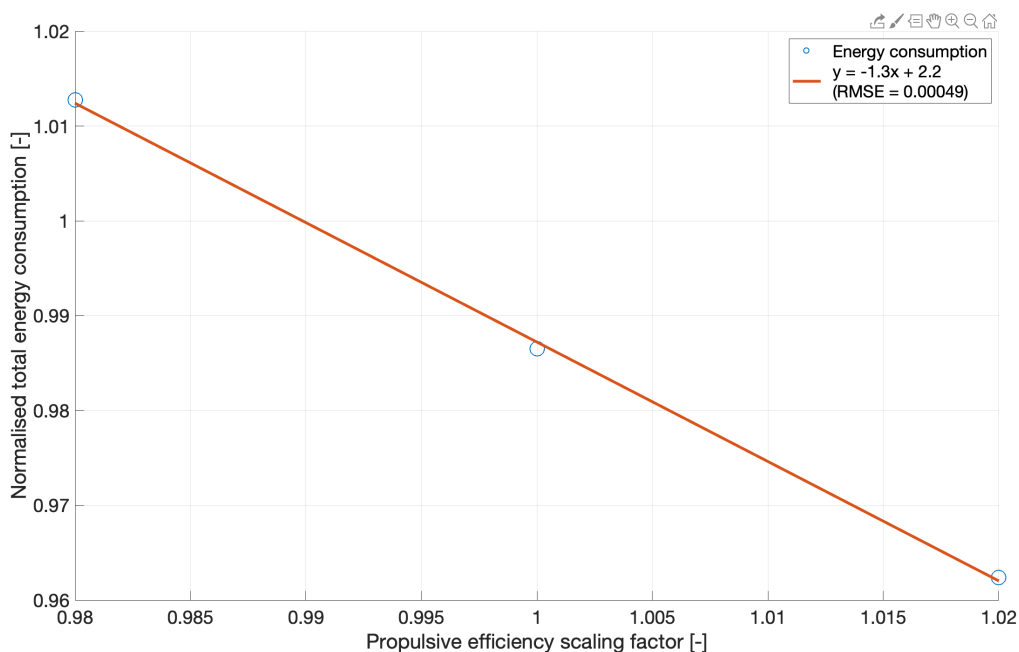


Figure 4.24: Sensitivity of total energy consumption to a change in propulsive efficiency

Figure 4.25 presents the sensitivity of the aircraft MTOM and OEM to the propulsive efficiency. The linear trendlines that have been fitted ($RMSE = 22 \times 10^{-5}$, $N = 3$ for the MTOM and $RMSE = 28 \times 10^{-4}$, $N = 3$ for the OEM) show a lower sensitivity of the mass to the propulsive efficiency when compared to the sensitivity of the energy consumption. A one percent decrease in propulsive efficiency results in a roughly 0.5% increase in MTOM and a 0.4% increase in OEM.

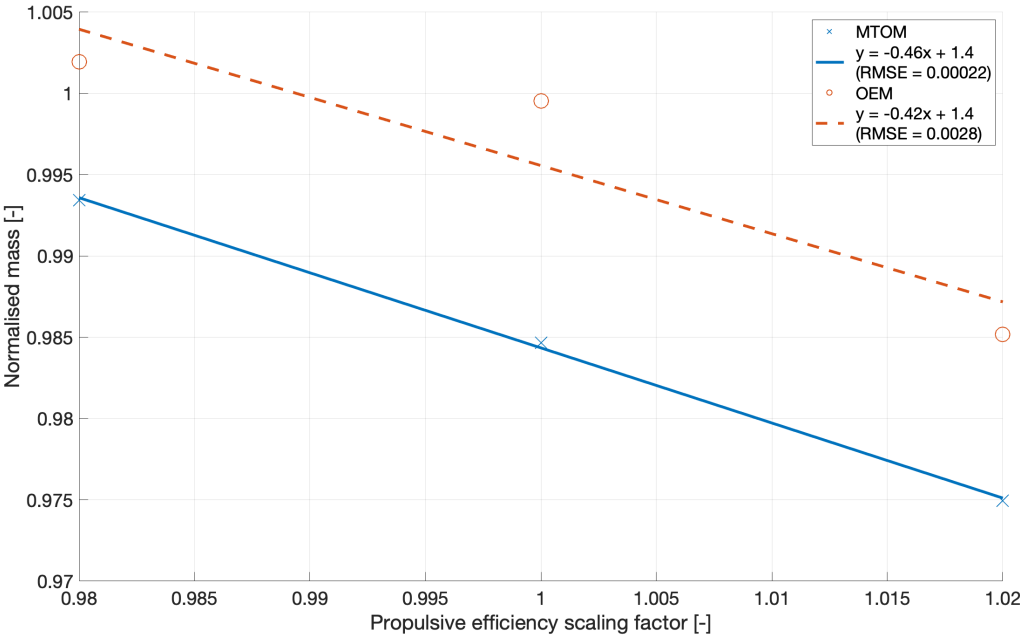


Figure 4.25: Sensitivity of aircraft to a change in propulsive efficiency

5

Discussion

The presented results are favourable towards the implementation of an APPU onto the A321neo-based reference aircraft. MTOM and total mission energy consumption are reduced through the implementation of the APPU, and CO₂-emissions can be reduced by 11%. The OEM reduces slightly, although it is effectively unchanged at 10% APPU shaft power share, and fuel mass reduces by up to 7%. Water vapour emissions are estimated to increase by up to 14%. Moreover, it was found that the liquid hydrogen storage tank, in a first order approximation, can be fitted into the unchanged tailcone up to an APPU shaft power share of 10%.

This chapter discusses the results presented in Chapter 4 and reflects critically on them. Section 5.1 dives deeper into the results and places them into context. Section 5.2 discusses the propeller performance and critically reflects on the method of estimating the isolated propeller performance, as well as on the method of predicting the effects of the implementation of BLI. The aircraft masses obtained in this study are discussed in Section 5.3, along with a discussion of the mass estimation methods used to model the A321appu. Finally, Section 5.4 combines the findings and summarises the validity and limitations of this study.

5.1. Discussion of Results

The total mission energy consumption presented in Figure 4.10 shows a reduction in energy consumed to execute the extended maximum range at maximum payload for both the BLI and the non-BLI-enabled aircraft. The non-BLI aircraft in this scenario is modelled in the same way as the BLI-enabled aircraft but augmentations to the propulsor propulsive efficiency and fuselage zero-lift drag are omitted. Moreover, the datapoints for the aircraft without BLI can be seen to have greater variance around the linear trendline ($RMSE = 15 \times 10^{-4}$, $N = 5$). This variance can be attributed to the various convergence errors of the Initiator, which can be as high as 1% on the MTOM. The error is on the order 0.2%. Consequently, conclusions drawn based on these results should be taken with caution and the observed trend is of higher value to answering the research question than the individual data points.

The BLI-equipped aircraft shows a linear trend with considerably lower variance in Figure 4.10 ($RMSE = 73 \times 10^{-5}$, $N = 5$). This trendline also shows a stronger negative slope. Meaning that, while the implementation of the APPU leads to a small reduction in energy consumption in itself, the majority of the reduction in energy consumption can be attributed to the implementation of BLI. This effect becomes more pronounced with increasing APPU shaft power share and thus with growing thrust coefficient (T_c).

The reduction in mission energy consumption for the non-BLI-enabled aircraft is largely attributed to the increased propulsive efficiency of the isolated APPU-propulsor. As presented in Figure 4.22, the isolated propulsor is roughly 8% more efficient at generating thrust than the main engines. Hence, when part of the required thrust is generated at higher propulsive efficiency, this leads to a reduction in required energy. The implementation of BLI leads to a further 8.7% increase in propulsive efficiency of the APPU propulsor and thus results in a further decrease in mission energy consumption. The overall reduction in MTOM, which is largely the result of lower fuel mass, further reduces the aircraft's energy consumption. These conclusions are supported by the reduction in energy consumption for a range of missions as presented in Figure 4.21, which shows that energy consumption decreases by around 1.4% for ranges between 1800 and 2500 NM.

Where the changes in energy consumption are small ($<1.5\%$), the accompanying changes in H_2O and CO_2 emissions are considerable. They show close to linear behaviour across the range of the shaft power shares presented in Figure 4.11 ($RMSE = 11 \times 10^{-4}$, $N = 5$). This indicates that, while the implementation of a cryogenic storage tank, a secondary fuel system, and a third BLI propulsor are not detrimental to the performance of the aircraft, the replacement of kerosene with liquid hydrogen drives the most evident difference with respect to the reference aircraft. The partial change-over in on-board energy carrier from kerosene to liquid hydrogen results in a direct decrease of CO_2 -emissions of 11% over the reference aircraft emissions. This can be attributed to the inherent carbon-free combustion of liquid hydrogen and reduces the aircraft's environmental impact [7]. The change-over also results in an increase in H_2O -emissions of around 14% over the reference aircraft emissions, following the increased formation of water vapour during the combustion of hydrogen with air. The effect of increased water vapour emissions on the environmental impact of the aircraft's operation is less evident, but it is likely to lead to increased radiative forcing especially when emitted at altitude [7, 18]. Results on NO_x -formation are not available due to its strong dependence on combustion chamber operating conditions and the current lack of a detailed APPU engine core design. However, NO_x -emissions are likely to decrease as a result of the partial introduction of hydrogen combustion when a micromix combustor is employed [42–45].

One of the most striking geometrical design changes to the aircraft is the cruciform empennage configuration. The horizontal stabiliser is moved upwards, along the span of the vertical stabiliser, to just above the APPU propulsor in order to prevent interference with the propulsor inflow and free up space in the tailcone for the APPU and cryogenic storage tank, as can be seen from Figure 4.17. The cruciform empennage is preferred over the T-tail configuration due to its reduced risk of deep stall and lower structural weight compared to a T-tail configuration [73]. The change in empennage configuration has resulted in a 7% smaller horizontal stabiliser and a 2% larger vertical stabiliser for the aircraft featuring 10% APPU shaft power share compared to the reference aircraft. Moreover, the vertical tail structure is roughly 10% heavier compared to the reference aircraft as a result of increased loads from the horizontal tail mounting, this is in line with Nicolosi et al. [109]. The 4° anhedral angle on the horizontal stabiliser increases its flutter speed and limits the increase structural mass of the vertical stabiliser [107].

The decrease in horizontal stabiliser surface area is evident from Figure 4.19. From this figure two distinct differences can be identified between the APPU-equipped aircraft and the reference aircraft. First, the APPU-equipped aircraft features a 14% larger c.g. shift, that is more biased towards the rear. This is the result of the additional 1217 kg of OEM added into the tailcone of the aircraft, in combination with the consumption of fuel housed in the tailcone. Additionally, the cruise stability constraint has decreased in slope by about 20%, which can be attributed to the higher flow velocity at the horizontal stabiliser as a result of its placement further away from the fuselage and the reduced influence of the downwash inflicted by the main wing [73, 89]. Additionally, the main wing has shifted rearward by 0.8 m and the horizontal stabiliser is shifted aft by 0.3 m following the geometry of the vertical stabiliser. The summation of these effect results in a 6% reduction in required horizontal stabiliser area to main wing area ratio, and a 7% reduction in absolute horizontal stabiliser area. This is combined with a 8% decrease in horizontal stabiliser structural mass.

From Table 4.1 it is evident that the total maximum sea-level take-off thrust of the A321 appu decreases by 2% with respect to the reference aircraft. This decrease in maximum thrust is in line with the reduction of MTOM and the nearly constant power loading across both aircraft. Consequently, it can be concluded that the implementation of BLI does not result in a reduction in required thrust but only in a reduction in the required power to generate that thrust.

Additionally, it can be seen that the implementation of an APPU that provides 10% of the required shaft power throughout the mission results in a 17% reduction in required main engine thrust compared to the reference aircraft. This can be attributed to the reduction in total thrust, and to the higher propulsive efficiency of the APPU propulsor, meaning that it can generate more thrust for the same shaft power than the main engines. The reduction in thrust is accompanied by a 17% reduction in main engines mass. Here it should be noted that the translation of shaft power to thrust, and the calculation of the thrust lapse with altitude and Mach number are both very basic in the Initiator. While the exact value of the reduction in required main engine thrust should thus be approached with caution, the general trend is in line with expectations. The exact maximum possible reduction in thrust is also subject to a number of operational and regulatory requirements,

and depends on the successful certification of the APPU as a third engine.

5.2. Discussion of Propulsor Performance

The inherent lack of carbon-based emissions from hydrogen combustion, means that a reduction in CO₂-emissions can be achieved through other hydrogen-combusting configurations as well. Consequently, to make an argument for the APPU-configuration requires a reduction in mission energy consumption, which hinges on the performance of the APPU's propulsor.

Figure 4.24 highlights the sensitivity of the aircraft energy consumption to the performance of the propulsor. From the linear trendline ($RMSE = 49 \times 10^{-5}$, $N = 3$) it can be concluded that a 1% decrease in propulsive efficiency results in a 1.3% increase in mission energy consumption for the extended maximum range at maximum payload mission. Moreover, Figure 4.25 presents the sensitivity of the aircraft MTOM and OEM to the propulsive efficiency. From the trendlines for MTOM ($RMSE = 22 \times 10^{-5}$, $N = 3$) and OEM ($RMSE = 28 \times 10^{-5}$, $N = 3$) it is evident that the masses increase by roughly 0.4% for every 1% decrease in propulsive efficiency. Consequently, the performance of the A321appu depends strongly on the propulsive efficiency of the propulsor.

The values presented for the propulsor performance in Figure 4.22 for the A321appu with 10% APPU shaft power share show that the propulsor is around 16% more efficient at generating thrust than the main engines. This is the result of the increased propulsive efficiency of propellers over turbofans engines, and the roughly 9% gain in propulsive efficiency through BLI [76]. The higher propulsive efficiency of the APPU propulsor results in decreasing energy consumption with increasing APPU shaft power share at nearly constant aircraft mass.

Problematically, the modelled propulsor was designed to operate at Mach numbers considerably lower than the operating Mach number of the A321appu [97]. Moreover, the accompanying calibrated performance estimation method by Zamboni [99] was only validated up to an advance ratio of 0.6, and does not account for the propeller resizing. At cruise conditions the APPU propulsor is estimated to operate at an advance ratio of 5.1. While the inner part of the propeller might see lower inflow Mach numbers as a result of being placed in the slower moving fuselage boundary layer, Figure 4.23 presents that the outer part of the propeller does not. The 3.44 m diameter propeller extends roughly 0.51 m beyond the 1.21 m thick boundary layer at the rear of the fuselage. The blade tips thus operate in the freestream Mach number. Moreover, the outer the part of the propeller has the highest rotational velocity component and will thus see the highest blade velocities. This means that the outer part of the propeller will suffer most from the compressibility effects and the accompanying reduced performance [75]. Furthermore, the addition of 4 extra propeller blades, which likely increase the propeller performance, have also not been accounted for [74].

No publications have been found that address the performance of a propeller or propfan with a 3.44 m diameter at an advance ratio of 5.1. Mikkelsen et al. [110] merely conclude that propeller efficiencies dropped fast beyond advance ratios of 3.8 as a result of compressibility effects in their tests. Other studies conclude that propfans, optimised for higher Mach numbers, can be operated successfully up to Mach numbers of 0.8 on commercial aircraft, and found between 20% and 25% reduction in fuel burn as a result of their implementation, though fuel consumption starts to increase rapidly beyond Mach 0.75 [75, 78, 79]. These performance benefits can largely be attributed to an increase in propulsive efficiency. Extending these general results to the APPU would mean that a 16% increase in propulsive efficiency over the main engines would be conservative considering the additional benefit of BLI, estimated at 9%, is already included. On the other hand, the modern turbofan engines fitted to the A321appu feature a bypass ratio of 11, meaning that their propulsive efficiency will have also improved considerably over the turbofan engines analysed in studies from the 1980s.

The effect of BLI is modelled using an engineering method by De Vries et al. [98] as an increase in propulsive efficiency and an increase in fuselage zero-lift drag. The method was validated for reference thrust coefficients, T_c^{ref} using fuselage wetted area as a reference area, between -0.003 and 0.016. It was shown to be less accurate at lower values of T_c^{ref} , even predicting a small increase in required shaft power, and was found to have better resemblance to the experimental data at higher thrust settings. In cruise the APPU operates up to a T_c^{ref} of 0.0012, which means the propulsive efficiency estimate might be inaccurate. This also explains

the increase in energy consumption at 2% APPU shaft power share between the BLI-enabled aircraft and the non-BLI-enabled aircraft presented in Figure 4.10. During take-off reference thrust coefficients as high as 0.017 are encountered, meaning that the method is well validated in this domain.

Additionally, the BLI performance estimation method employed for this study assumes a simplified axisymmetric fuselage tailcone geometry, which is presented in Figure 3.5, and a uniform inflow into the propulsor. Both assumptions likely lead to an overestimation of the BLI performance. From Figure 4.5 and Figure 4.17 it is evident that the actual tailcone geometry is not axisymmetric. For the actual tailcone geometry the fuselage upsweep will lead to a considerable variation in boundary layer profiles being ingested into the propulsor. Moreover, the vertical stabiliser and APPU air inlet are expected to add additional non-uniformity to the fuselage boundary layer. These non-uniformities will result in increased structural loading on the propeller, and could reduce overall performance [62, 66]. The APPU inlet and exhaust have not been considered in this study, but they might be integrated in a synergistic manner to help improve APPU performance. Overall, the uniform and axisymmetric inflow assumptions are likely major simplifications of the aft-fuselage flow field. They are expected to have resulted in an overoptimistic assessment of the propulsor performance.

Operating a large propeller at high Mach number and high advance ratio in a BLI configuration, which results in non-uniform inflow, is likely to be a challenge for designers. The results that have been presented appear conservative compared to the results of propfan research by NASA in the 1980's. Moreover, the validation of the BLI model suggest that the propulsive efficiency gain resulting from BLI during the cruise phase is likely pessimistic. However, the aircraft's performance has been shown to depend strongly on the performance of the propulsor, which is predicted with great uncertainty due to the lack of appropriate reference propeller performance data. A 1% decrease in estimated propulsive efficiency would outweigh the entire reduction in energy consumption presented for 10% APPU shaft power share. A further reduction in propulsive performance would result in an increase in aircraft energy consumption and an increase in aircraft emissions as a result of the implementation of an APPU. On the other hand, a higher propulsive efficiency than that presented in Section 4.4 directly results in a strong decrease in energy consumption and a further decrease in CO₂-emissions. Therefore, it is suggested that the propeller performance presented in this study should be interpreted as a minimal design requirement to achieving a meaningful reduction in total mission energy consumption through the implementation of the APPU.

5.3. Discussion of Aircraft Weight

Weight savings as a result of the implementation of the APPU are minor. The marginal decrease in OEM combined with a decrease in fuel weight are responsible for part of the reduction in energy consumption. While the decrease in MTOM is in line with results from other studies into the conversion of conventional aircraft to hydrogen-powered aircraft, the decrease in OEM is not. Here, it must be noted that these studies focused solely on the conversion from kerosene-powered to fully hydrogen-powered aircraft. Their results are thus not directly applicable. However, it is believed that the addition of a cryogenic storage tank and a heavier cryogenic fuel system results in increased OEM [19, 26, 31].

A considerable contributor to the reduction in OEM is the removal of the conventional APU. Especially for the aircraft featuring less than 4% APPU shaft power share, the APPU mass is lower than the mass of the APU it replaces. This is the direct result of the two different mass estimation methods implemented for the two power generators. The mass of the APU is estimated using a fixed percentage of the MTOM based on reference aircraft data, while the mass of the APPU is determined based on the required shaft power using turboprop engine sizing rules and reference engines [89].

The mass of the installed APU on the reference aircraft is estimated to be 740 kg. The actual dry mass of the APU used on Airbus A320-200 is 140 kg [111]. Following the overall similarity between the Airbus A320-200 and the A321neo, it is likely that the mass of the APU fitted to the A321neo will be similar. Though the exact build-up of the installed APU mass is ambiguous, an installed APU mass of 740 kg for the reference aircraft is likely an overestimation, which can be attributed to a biased and underpopulated reference database of APU masses.

The estimated mass of the APPU is not augmented with an additional component to account for the delivery of the required auxiliary power, because the APPU shaft power requirement far exceeds the auxiliary power requirement [112]. Moreover, the engine sizing relations used for the main engines and the APPU already account for the engines developing auxiliary power during flight, when the APU is switched off. The mass of the cabin support and electrical systems has been accounted for separately in the systems mass breakdown presented in Figure 4.16. Consequently, it has been assumed that the conventional Class II sizing of the main engines and the APPU would sufficiently account for the delivery of auxiliary power. However, this assumption leads to overoptimistic OEM estimations for low APPU shaft power shares.

The overestimation of the APU mass on the reference aircraft has likely resulted in an overoptimistic representation of the effect of adding an APPU to the reference aircraft. It is expected that using a more representative APU mass on the reference aircraft results in a mass reduction of several hundred kilograms in the tailcone, leading to a slightly lower OEM, MTOM and energy consumption. Considering the minor differences between the reference aircraft and the APPU-equipped aircraft, the correction of the APU mass could result in an overall minor increase in OEM, combined with a less optimistic reduction in MTOM and energy consumption as a result of the implementation of an APPU.

A second major component to the change in OEM is the mass of the liquid hydrogen storage tank. The masses of the various tanks increase with increasing APPU shaft power share as a result of having to store greater quantities of liquid hydrogen. Moreover, the gravimetric efficiency of the tank, which structurally is modelled as an equivalent cylinder with a diameter equal to the major diameter of the cone, is presented in Figure 4.12. It can be seen to increase as the required tank volume increases, peaking at around 59%. The increasing and subsequent decreasing of the tank gravimetric efficiency is in line with expectations set by Winnefeld et al. [49]. At low APPU shaft power shares, the tank already has a maximum outer diameter equal to 95% of the fuselage diameter. This means that the tank features relatively large end caps and is very short. Increasing the required storage volume leads to an increase in tank length, coupled with a decrease in surface-area-to-volume ratio. This leads to reduced insulation mass. As the tank grows further, the minor diameter decrease and the surface-area-to-volume ratio starts to increase, which results in a peak in tank gravimetric efficiency.

It should be noted that the structural modelling of a sheared conical tank as an equivalent cylinder with a diameter equal to the major diameter of the cone likely results in an overoptimistic tank mass. The structural design of a sheared conical tank is likely to yield higher structural mass than a cylindrical tank. Moreover, the novelty of a sheared conical tank mounted within the fuselage could lead to high safety margins on the tank structure. These might drive up the tank structural mass further. This, coupled with a tank sizing methodology that was designed for larger tanks, means that its mass estimation is subject to errors. On the other hand, the use composite materials or an integral tank might reduce the overall tank mass. In the end the tank mass is likely to be subject to inaccuracies and should be taken as a first order estimate. Furthermore, a doubling of the tank mass would result in a minor ($\sim 1\%$) increase in OEM and is therefore not expected to affect the performance of the final aircraft greatly.

A greater challenge regarding the cryogenic storage tank lies in the maximum tank volume. In the current modelling of the aircraft geometry, the tank size limit is reached around 10% APPU shaft power share, or roughly 650 kg of liquid hydrogen. A further increase in required liquid hydrogen mass, as a result of reduced APPU performance or disappointing insulation performance, would cause the tank volume to grow beyond the geometrical limitations of the tailcone. This could warrant costly and potentially heavy structural redesigns or a reduction in APPU shaft power share.

The insulation performance chosen for this study is optimistic and surpasses currently available insulation solutions. Consequently, the maximum available tailcone volume for the tank sets a technical target for designers of the insulation system. On the other hand, the tank insulation is sized such that no venting of gaseous hydrogen is required during the maximum range at maximum payload mission. If this requirement relaxed, the insulation thickness and mass can be reduced.

Moreover, the chosen tank volume is subject to operational requirements. For this study to APPU is assumed to contribute equally to the delivered power during each of the flight phases. Varying operational requirements and objectives might result in different APPU requirements and accompanying cryogenic storage tank volumes.

Summarising, the mass performance of the APPU installation as a whole is believed to be strongly dependent on the APPU operational requirements and the structural design of the tailcone including the cryogenic storage tank. Operational requirements will determine the required tank volume, while the specifics of the structural design would determine the final mass of the installation. For this study the tailcone structure, tank structure, and the accompanying aircraft mass results are based on conceptual design methods. They should thus be interpreted with appropriate caution. Moreover, the reduction in aircraft mass resulting from the removal of the APU is overestimated, this could result in an overall increase in OEM of the APPU-equipped aircraft over reference aircraft by as much as 0.5%.

5.4. Discussion of Study Limitations

Overall, the results presented in this study show that the implementation of the APPU into an A321neo-based reference aircraft results in small differences in total mission energy consumption and aircraft weight performance. The uncertainty of these results is hard to quantify due to a lack of aircraft design studies into similar concepts. The results are based on a collection of individually validated conceptual design methods with a range of accompanying limitations. They are also subject to the design convergence of the Initiator, which in the outer loop can have an error of up to 1% on the MTOM. The discrepancies and uncertainties in the methods presented in this study for estimating the APPU installation mass and the propulsor performance are likely larger than the reported saved energy fraction or change in aircraft mass. Consequently, conclusions regarding mission energy consumption and aircraft mass should be approached with caution.

The presented changes in aircraft emissions, resulting largely from the partial change-over from kerosene to liquid hydrogen, can be met with greater certainty following the inherent lack of carbon-based emissions from hydrogen combustion, accompanied by an undisputed increase in water vapour emissions. Simply put, replacing kerosene with liquid hydrogen as on-board energy carrier results in reduced carbon-based emissions and increased water vapour emissions during aircraft operations.

6

Conclusion

The implementation of the APPU on an A321neo-based reference aircraft reduces the total mission energy consumption and results in marginally lower MTOM and OEM. For increasing APPU shaft power share the required energy is found to decrease further, while the OEM increases as a result of the higher liquid hydrogen storage tank mass and APPU engine mass. A higher APPU shaft power share also results in a lower fuel mass, however the increasing OEM results in an overall growing MTOM. The reduced energy consumption in combination with the greater use of liquid hydrogen and reduced consumption of kerosene, results in reducing CO₂-emissions and increasing water vapour emissions with growing APPU shaft power share. The strongest reduction in energy consumption can be found for an APPU shaft power share of 10%, beyond which the cryogenic storage tank grows outside the geometrical limits of the tailcone as a result of increased hydrogen consumption.

For this highest APPU shaft power share, the propulsive efficiency of the BLI propulsor is 16% higher than that of the main turbofan engines. The majority of this reduction can be attributed to the implementation of BLI, which results in a 9% increase in propulsive efficiency and a fuselage zero-lift drag increase of 1.5 counts. The aircraft has a roughly 1% lower MTOM at similar OEM compared to the reference aircraft. Overall the mission energy consumption is reduced across a spread of different mission ranges by about 1.4%. Roughly 0.9% of this reduction is attributed directly to the implementation of BLI.

Besides the reduction in mission energy consumption, the implementation of an APPU providing 10% of the required shaft power throughout the mission results in an 11% reduction in CO₂-emissions and a 14% increase in water vapour emissions. This is likely accompanied by a considerable reduction in NO_x-emissions through the use of a micromix combustor. Seeing that hydrogen combustion is inherently free of carbon-based emissions and results in increased water emissions compared to kerosene combustion, the change in emissions profile is largely attributed to the partial change-over from kerosene to liquid hydrogen.

On the APPU-equipped aircraft the horizontal stabiliser is moved onto the vertical stabiliser in a cruciform empennage configuration to free up space in the tailcone. This has resulted in a 7% increase in horizontal stabiliser area and a 10% increase vertical stabiliser mass. The resulting available space in the tailcone is used to house a 9 m³ cryogenic storage tank and fuel system, and the APPU. These changes have added around 1200 kg of mass to tailcone and have resulted in a rearward shift of the main wing by about 0.8 m. Additionally, the main engines have been reduced in mass by 17% following a reduction in their required thrust.

The reduced energy consumption and lower aircraft mass as a result of the APPU-implementation should be considered with caution following the uncertainties in the various conceptual design methods employed, in combination with the convergence error of the Aircraft Design Initiator itself. The results regarding greenhouse gas emissions can be taken with greater certainty considering the undisputed reduction in carbon-based emissions and increase in water vapour emissions from the combustion of hydrogen.

All in all, it can be concluded that the implementation of the APPU does not strongly affect the performance of the aircraft but does change the emissions profile considerably. This hinges strongly on the detailed design implementation of the APPU and the performance of the BLI propulsor. The structural design of the tailcone, including the secondary fuel system, cryogenic fuel tank, APPU engine with accompanying intake and exhaust, and the propulsor will be a considerable design challenge, upon which the weight performance of the

A321appu depends. The total energy consumption will be strongly influenced by the effectiveness of the BLI propulsor.

It is suggested that future research should be focused on understanding the flow field surrounding the tailcone at high Mach number. Moreover, a detailed assessment of propulsor performance at high advance ratios in BLI configuration is needed to provide greater insight into the performance of an APPU. The propulsor structural design, and its ability to cope with the non-uniform inflow at the tip of the tailcone, is also key to the success of the APPU concept. Future research efforts might also be focused on cryogenic storage tank insulation systems and the accompanying certification process. The presented cryogenic tank insulation performance and the performance of the APPU propulsor are suggested as minimal design requirement for the further development of the APPU. Finally, a multitude of operational factors can influence the effective use of the concept.

Bibliography

- [1] Airbus. Airbus Global Market Forecast 2021-2040, 2021.
- [2] Airbus. Global Market Forecast: Cities, Airports & Aircraft 2019-2038, 2019.
- [3] Boeing. Commercial Market Outlook 2020-2039, 2020.
- [4] Boeing. Commercial Market Outlook 2021-2040, 2021.
- [5] B. Pearce. Covid-19 Outlook for air travel in the next 5 years. Technical report, IATA, 5 2020.
- [6] D. S. Lee, D. W. Fahey, P. M. Forster, P. J. Newton, R. C.N. Wit, L. L. Lim, B. Owen, and R. Sausen. Aviation and global climate change in the 21st century. *Atmospheric Environment*, 43(22-23):3520–3537, 7 2009. ISSN 13522310. doi: 10.1016/j.atmosenv.2009.04.024.
- [7] D. S. Lee, D. W. Fahey, A. Skowron, M. R. Allen, U. Burkhardt, Q. Chen, S. J. Doherty, S. Freeman, P. M. Forster, J. Fuglestvedt, A. Gettelman, R. R. De León, L. L. Lim, M. T. Lund, R. J. Millar, B. Owen, J. E. Penner, G. Pitari, M. J. Prather, R. Sausen, and L. J. Wilcox. The contribution of global aviation to anthropogenic climate forcing for 2000 to 2018. *Atmospheric Environment*, 244, 1 2021. ISSN 18732844. doi: 10.1016/j.atmosenv.2020.117834.
- [8] ACARE. Flightpath 2050 Europe's Vision for Aviation. Technical report, European Commission, 2011.
- [9] ATAG. Blueprint for a green recovery, 9 2020. URL www.aviationbenefits.org.
- [10] D. C. Acevedo, T. van Cranenburgh, J. Exalto, L. Halsema, B. van der Heijden, Y. Hoogterp, E. Jahilo, A. M. Jorge, Y. Naäman, M. van Schie, and M. van der Zwan. Final Report A320 Auxiliary Propulsion and Power Unit. Technical report, Delft University of Technology, Delft, The Netherlands, 2020.
- [11] A. Gangoli Rao, F. Yin, and H. G. C. Werij. Energy transition in aviation: The role of cryogenic fuels. *Aerospace*, 7(12):1–24, 12 2020. ISSN 22264310. doi: 10.3390/aerospace7120181.
- [12] A. Gangoli Rao and F. Yin. Energy transition in aviation: The role of cryogenic fuels. *Abstract from 3rd ECATS Conference, Making Aviation Environmentally Sustainable*, 1:221–226, 6 2020.
- [13] A. Seitz, A. L. Habermann, F. Peter, F. Troeltsch, A. Castillo Pardo, B. Della Corte, M. Van Sluis, Z. Goraj, M. Kowalski, X. Zhao, T. Grönstedt, J. Bijewitz, and G. Wortmann. Proof of concept study for fuselage boundary layer ingesting propulsion. *Aerospace*, 8(1):1–65, 1 2021. ISSN 22264310. doi: 10.3390/aerospace8010016.
- [14] K. W. Burger. Emissions of an Airbus A321 with Auxiliary Power and Propulsion Unit - Literature Study. Technical report, Delft University of Technology, Delft, 6 2021. URL repository.tudelft.nl.
- [15] C. B. Meher-Homji and E. Prisell. Pioneering Turbojet Developments of Dr. Hans Von Ohain-From the HeS 1 to the HeS 011. *Journal of Engineering for Gas Turbines and Power*, 122:191–201, 4 2000. URL http://asmedigitalcollection.asme.org/gasturbinespower/article-pdf/122/2/191/5636828/191_1.pdf.
- [16] J. L. Sloop. *LIQUID HYDROGEN AS A PROPULSION FUEL, 1945-1959*. National Aeronautics and Space Administration, 1978.
- [17] G. D. Brewer. THE PROSPECTS FOR LIQUID HYDROGEN FUELED AIRCRAFT. *Int. J. Hydrogen Energy*, 7(1):21–41, 1982.
- [18] D. Cecere, E. Giacomazzi, and A. Ingenito. A review on hydrogen industrial aerospace applications. *International Journal of Hydrogen Energy*, 39(20):10731–10747, 7 2014. ISSN 03603199. doi: 10.1016/j.ijhydene.2014.04.126.

- [19] D. Verstraete. On the energy efficiency of hydrogen-fuelled transport aircraft. *International Journal of Hydrogen Energy*, 40(23):7388–7394, 6 2015. ISSN 03603199. doi: 10.1016/j.ijhydene.2015.04.055.
- [20] Airbus. Airbus reveals new zero-emission concept aircraft, 9 2020. URL <https://www.airbus.com/newsroom/press-releases/en/2020/09/airbus-reveals-new-zeroemission-concept-aircraft.html>.
- [21] I. Yilmaz, M. Ilbaş, M. Taştan, and C. Tarhan. Investigation of hydrogen usage in aviation industry. In *Energy Conversion and Management*, volume 63, pages 63–69, 11 2012. doi: 10.1016/j.enconman.2011.12.032.
- [22] J. Clarkin. Hydrogen: Opportunities and challenges. In *AIAAVCAS International Air and Space Symposium and Exposition: The Next 100 Years*, pages 2881–2886, Dayton, Ohio, 2003. American Institute of Aeronautics and Astronautics Inc. doi: 10.2514/6.2003-2881.
- [23] M. Prewitz, A. Bardenhagen, and R. Beck. Hydrogen as the fuel of the future in aircrafts – Challenges and opportunities. *International Journal of Hydrogen Energy*, 45(46):25378–25385, 9 2020. ISSN 03603199. doi: 10.1016/j.ijhydene.2020.06.238.
- [24] P. Rompokos, A. Rolt, D. Nalianda, A. T. Isikveren, C. Senné, T. Gronstedt, and H. Abedi. Synergistic Technology Combinations for Future Commercial Aircraft Using Liquid Hydrogen. *Journal of Engineering for Gas Turbines and Power*, 143(7):1–8, 7 2021. ISSN 0742-4795. doi: 10.1115/1.4049694.
- [25] G. D. Brewer, R. E. Morris, G. W. Davis, E. F. Versaw, G. R. Jr. Cunningham, J. C. Ripple, C. F. Baerst, and G. Garmong. FINAL REPORT-Volume II STUDY OF FUEL SYSTEMS FOR LH2-FUELED SUBSONIC TRANSPORT AIRCRAFT. Technical report, National Aeronautics and Space Administration, 7 1978. URL <https://ntrs.nasa.gov/search.jsp?R=19780023143>.
- [26] G. D. Brewer and R. E. Morris. Tank and Fuel Systems Considerations for Hydrogen Fueled Aircraft. Technical report, Lockheed California Company, Burbank, 2 1985.
- [27] G. D. Brewer and R. E. Morris. STUDY OF LH2 FUELED SUBSONIC PASSENGER TRANSPORT AIRCRAFT. Technical report, Lockheed California Compnay, Burbank, 1 1976.
- [28] G. D. Brewer, R. E. Morris, R. H. Lange, and J. W. Moore. VOLUME II FINAL REPORT: STUDY OF THE APPLICATION OF HYDROGEN FUEL TO LONG-RANGE SUBSONIC TRANSPORT AIRCRAFT. Technical report, NASA, 1 1975.
- [29] G. D. Brewer. *Hydrogen Aircraft Technology*. CRC Press, first edition, 6 1991.
- [30] V. Sosounov and V. Orlov. Experimental turbofan using liquid hydrogen and liquid natural gas as fuel. In *AIAA/SAE/ASME/ASEE 26th Joint Propulsion Conference*, pages 2421–2433, Orlando, Florida, 7 1990. American Institute of Aeronautics and Astronautics (AIAA). doi: 10.2514/6.1990-2421.
- [31] A. Westenberger. Liquid Hydrogen Fuelled Aircraft - System Analysis, CRYOPLANE. Final Technical Report (Publishable Version). Technical report, Airbus Deutschland GmbH, 9 2003.
- [32] G. Dahl and F. Suttrop. Engine Control and Low-NOx Combustion for Hydrogen Fuelled Aircraft Gas Turbines. *Hydrogen Energy*, 23(8):695–704, 1998. doi: 10.1016/S0360-3199(97)00115-8.
- [33] Boeing. Boeing Phantom Eye Completes 1st Autonomous Flight, 6 2012. URL <https://boeing.mediaroom.com/2012-06-04-Boeing-Phantom-Eye-Completes-1st-Autonomous-Flight>.
- [34] ZeroAvia. ZeroAvia Conducts UK’s First Commercial-Scale Electric Flight, 6 2020. URL <https://www.zeroavia.com/press-release-23-06-2020>.
- [35] A. Karakurt, B. Khandelwal, V. Sethi, and R. Singh. Evaluation of hydrogen combustors for gas turbines. In *10th Annual International Energy Conversion Engineering Conference, IECEC 2012*, pages 4227–4247, Atlanta, Georgia, 7 2012. American Institute of Aeronautics and Astronautics Inc. ISBN 9781624101908. doi: 10.2514/6.2012-4227.
- [36] P. Chiesa, G. Lozza, and L. Mazzocchi. Using hydrogen as gas turbine fuel. *Journal of Engineering for Gas Turbines and Power*, 127(1):73–80, 1 2005. ISSN 07424795. doi: 10.1115/1.1787513.

- [37] J. Davies and A. Prakash. An investigation into the feasibility of alternative aviation fuels. In *AIAA Scitech 2020 Forum*, volume 1 PartF, pages 642–662, Orlando, Florida, 1 2020. American Institute of Aeronautics and Astronautics Inc, AIAA. ISBN 9781624105951. doi: 10.2514/6.2020-0642.
- [38] Y. B. Zeldovich. The oxidation of nitrogen in combustion and explosions. *Acta Physicochimica URSS*, 21:577–628, 1946.
- [39] J. Brand, S. Sampath, F. Shum, R. L. Bayt, and J. Cohen. Potential use of hydrogen in air propulsion. In *AIAA/CAS International Air and Space Symposium and Exposition: The Next 100 Years*, pages 2879–2891, Dayton, Ohio, 2003. American Institute of Aeronautics and Astronautics Inc. doi: 10.2514/6.2003-2879.
- [40] A. Cappelletti and F. Martelli. Investigation of a pure hydrogen fueled gas turbine burner. *International Journal of Hydrogen Energy*, 42(15):10513–10523, 4 2017. ISSN 03603199. doi: 10.1016/j.ijhydene.2017.02.104.
- [41] P. F. Ghali and B. Khandelwal. Design and simulation of a hydrogen micromix combustor. In *AIAA Scitech 2021 Forum*, pages 1–13. American Institute of Aeronautics and Astronautics Inc, AIAA, 2021. ISBN 9781624106095. doi: 10.2514/6.2021-1984.
- [42] P. Agarwal, X. Sun, P. Q. Gauthier, and V. Sethi. Injector design space exploration for an ultra-low NOx hydrogen micromix combustion system. In *Proceedings of the ASME Turbo Expo 2019*, volume 3, pages 90833–90846, Phoenix, Arizona, USA, 2019. American Society of Mechanical Engineers (ASME). ISBN 9780791858608. doi: 10.1115/GT2019-90833.
- [43] G. Babazzi, P. Q. Gauthier, P. Agarwal, J. McClure, and V. Sethi. NOx emissions predictions for a hydrogen micromix combustion system. In *Proceedings of the ASME Turbo Expo*, volume 3, pages 90532–90544, Phoenix, Arizona, USA, 6 2019. American Society of Mechanical Engineers (ASME). ISBN 9780791858608. doi: 10.1115/GT2019-90532.
- [44] R. Ben Abdallah, V. Sethi, P. Q. Gauthier, A. M. Rolt, and D. Abbott. A DETAILED ANALYTICAL STUDY OF HYDROGEN REACTION IN A NOVEL MICROMIX COMBUSTION SYSTEM. In *Proceedings of ASME Turbo Expo 2018 Turbomachinery Technical Conference and Exposition*, pages 76568–76597, Oslo, Norway, 6 2018. ASME. doi: 10.1115/GT2018-76586. URL <https://proceedings.asmedigitalcollection.asme.org>.
- [45] H. Lei and B. Khandelwal. Investigation of novel configuration of hydrogen micromix combustor for low nox emission. In *AIAA Scitech 2020 Forum*, volume 1 PartF. American Institute of Aeronautics and Astronautics Inc, AIAA, 2020. ISBN 9781624105951. doi: 10.2514/6.2020-1933.
- [46] A. Haj Ayed, K. Kusterer, H. H.W. Funke, J. Keinz, C. Striegan, and D. Bohn. Improvement study for the dry-low-NOx hydrogen micromix combustion technology. *Propulsion and Power Research*, 4(3): 132–140, 9 2015. ISSN 2212540X. doi: 10.1016/j.jprr.2015.07.003.
- [47] D. R. Noble, Q. Zhang, A. Shareef, J. Tootle, A. Meyers, and T. Lieuwen. Syngas mixture composition effects upon flashback and blowout. In *Proceedings of the ASME Turbo Expo*, volume 1, pages 357–368, 2006. ISBN 0791842363. doi: 10.1115/GT2006-90470.
- [48] H. Nojoudi, I. Dincer, and G. F. Naterer. Greenhouse gas emissions assessment of hydrogen and kerosene-fueled aircraft propulsion. *International Journal of Hydrogen Energy*, 34(3):1363–1369, 2 2009. ISSN 03603199. doi: 10.1016/j.ijhydene.2008.11.017.
- [49] C. Winnefeld, T. Kadyk, B. Bensmann, U. Krewer, and R. Hanke-Rauschenbach. Modelling and designing cryogenic hydrogen tanks for future aircraft applications. *Energies*, 11(105):1–23, 1 2018. ISSN 19961073. doi: 10.3390/en11010105.
- [50] R. O. Stroman, M. W. Schuette, K. Swider-Lyons, J. A. Rodgers, and D. J. Edwards. Liquid hydrogen fuel system design and demonstration in a small long endurance air vehicle. *International Journal of Hydrogen Energy*, 39(21):11279–11290, 7 2014. ISSN 03603199. doi: 10.1016/j.ijhydene.2014.05.065.

- [51] D. Verstraete, P. Hendrick, P. Pilidis, and K. Ramsden. Hydrogen fuel tanks for subsonic transport aircraft. *International Journal of Hydrogen Energy*, 35(20):11085–11098, 10 2010. ISSN 03603199. doi: 10.1016/j.ijhydene.2010.06.060.
- [52] S. K. Mital, J. Z. Gyekenyesi, S. M. Arnold, R. M. Sullivan, J. M. Manderscheid, and P. L. N. Murthy. Review of Current State of the Art and Key Design Issues With Potential Solutions for Liquid Hydrogen Cryogenic Storage Tank Structures for Aircraft Applications. Technical report, NASA, Cleveland USA, 10 2006. URL <http://www.sti.nasa.gov>.
- [53] M. J. Robinson, J. D. Eichinger, and S. E. Johnson. Hydrogen permeability requirements and testing for reusable launch vehicle tanks. In *Collection of Technical Papers - AIAA/ASME/ASCE/AHS/ASC Structures, Structural Dynamics and Materials Conference*, volume 3, pages 1708–1717. American Inst. Aeronautics and Astronautics Inc., 2002. doi: 10.2514/6.2002-1418.
- [54] D. Verstraete. *The Potential of Liquid Hydrogen for long range aircraft propulsion*. PhD thesis, Cranfield University, Cranfield, 4 2009.
- [55] R. Begag, S. White, J. E. Fesmire, and W. L. Johnson. Hybrid aerogel-MLI insulation system performance studies for cryogenic storage in space applications. In *Materials Research Society Symposium Proceedings*, volume 1306, pages 13–18, 2011. ISBN 9781618395139. doi: 10.1557/opl.2011.88.
- [56] J. E. Fesmire and W. L. Johnson. Cylindrical cryogenic calorimeter testing of six types of multilayer insulation systems. *Cryogenics*, 89:58–75, 1 2018. ISSN 00112275. doi: 10.1016/j.cryogenics.2017.11.004.
- [57] F. Yin and A. Gangoli Rao. Performance assessment of a Multi-fuel Hybrid Engine for Future Aircraft. *Greener Aviation*, (57):1–11, 2016. doi: 10.1016/j.ast.2018.03.005.
- [58] G. Onorato. Fuel Tank Integration for Hydrogen Airliners. Technical report, Delft University of Technology, Delft, 8 2021. URL <http://repository.tudelft.nl/>.
- [59] L. H. Smith. Wake ingestion propulsion benefit. *Journal of Propulsion and Power*, 9(1):74–82, 1993. ISSN 07484658. doi: 10.2514/3.11487.
- [60] A. M. O. Smith and H. E. Roberts. The Jet Airplane Utilizing Boundary Layer Air for Propulsion. *Journal of the Aeronautical Sciences*, 14(2):97–109, 2 1947. doi: 10.2514/8.1273.
- [61] A. Lundbladh and T. Grönstedt. Distributed Propulsion and Turbofan Scale Effects. *ISABE*, 2005.
- [62] T. V. Marien, J. R. Welstead, and S. M. Jones. Vehicle-level system impact of boundary layer ingestion for the NASA D8 concept aircraft. In *AIAA Aerospace Sciences Meeting, 2018*, number 210059. American Institute of Aeronautics and Astronautics Inc, AIAA, 2018. ISBN 9781624105241. doi: 10.2514/6.2018-0271.
- [63] A. M. Fernández and H. Smith. Effect of a fuselage boundary layer ingesting propulsor on airframe forces and moments. *Aerospace Science and Technology*, 100, 5 2020. ISSN 12709638. doi: 10.1016/j.ast.2020.105808.
- [64] T. S. Tse and C. A. Hall. Flow field and power balance of a distributed aft-fuselage boundary layer ingesting aircraft. In *AIAA Propulsion and Energy 2020 Forum*, pages 1–20. American Institute of Aeronautics and Astronautics Inc, AIAA, 2020. ISBN 9781624106026. doi: 10.2514/6.2020-3779.
- [65] A. Seitz and C. Gologan. Parametric design studies for propulsive fuselage aircraft concepts. *CEAS Aeronautical Journal*, 6(1):69–82, 3 2015. ISSN 18695590. doi: 10.1007/s13272-014-0130-3.
- [66] D. K. Hall, A. C. Huang, A. Uranga, E. M. Greitzer, M. Drela, and S. Sato. Boundary layer ingestion propulsion benefit for transport aircraft. *Journal of Propulsion and Power*, 33(5):1118–1129, 2017. ISSN 15333876. doi: 10.2514/1.B36321.
- [67] A. Seitz. *Advanced Methods for Propulsion System Integration in Aircraft Conceptual Design*. PhD thesis, Technischen Universität München, Munich, Germany, 6 2012.

- [68] P. Lv, A. G. Rao, D. Ragni, and L. Veldhuis. Performance analysis of wake and boundary-layer ingestion for aircraft design. *Journal of Aircraft*, 53(5):1517–1526, 2016. ISSN 15333868. doi: 10.2514/1.C033395.
- [69] A. L. Habermann, J. Bijewitz, A. Seitz, and M. Hornung. Performance bookkeeping for aircraft configurations with fuselage wake-filling propulsion integration. *CEAS Aeronautical Journal*, 11(2):529–551, 6 2020. ISSN 18695590. doi: 10.1007/s13272-019-00434-w.
- [70] J. Ahuja and D. N. Mavris. A method for modeling the aero-propulsive coupling characteristics of BLI aircraft in conceptual design. In *AIAA Scitech 2021 Forum*, pages 1–34. American Institute of Aeronautics and Astronautics Inc, AIAA, 2021. ISBN 9781624106095. doi: 10.2514/6.2021-0112.
- [71] S. Samuelsson and T. Grönstedt. Performance analysis of turbo-electric propulsion system with fuselage boundary layer ingestion. *Aerospace Science and Technology*, 109, 2 2021. ISSN 12709638. doi: 10.1016/j.ast.2020.106412.
- [72] E. Torenbeek. *Advanced Aircraft Design: Conceptual Design, Analysis and Optimization of Subsonic Civil Airplanes*. John Wiley and Sons, Ltd., 2013. ISBN 9781119969303.
- [73] D. P. Raymer. *Aircraft Design: A Conceptual Approach*. American Institute of Aeronautics and Astronautics, second edition, 1992. ISBN 0930403517.
- [74] J. Roskam. *Airplane Design Part III: Layout Design of Cockpit, Fuselage, Wing and Empennage: Cut-aways and Inboard Profiles*. DARcorporation, third printing edition, 2002. ISBN 188488556x.
- [75] H. I. H. Saravanamuttoo. MODERN TURBOPROP ENGINES. *Prog. Aerospace Sci.*, 24:225–248, 1987.
- [76] S. Langmaak, J. Scanlan, and A. Sobester. Robust gas turbine and airframe system design in light of uncertain fuel and CO₂ prices. In *Journal of Aircraft*, volume 53, pages 1372–1390. American Institute of Aeronautics and Astronautics Inc., 2016. doi: 10.2514/1.C033610.
- [77] M. D. Guynn, J. J. Berton, E. S. Hendricks, M. T. Tong, W. J. Haller, and D. R. Thurman. Initial assessment of open rotor propulsion applied to an advanced single-aisle aircraft. In *11th AIAA Aviation Technology, Integration, and Operations (ATIO) Conference, Including the AIA*, pages 7058–7075, Virginia Beach, Virginia, 9 2011. AIAA. ISBN 9781600869419. doi: 10.2514/6.2011-7058.
- [78] C. N. Reynolds. Advanced Prop-Fan Engine Technology (APET) Single- and Counter Rotation Gearbox/Pitch Change Mechanism. Technical report, National Aeronautics and Space Administration, 7 1985.
- [79] I. M. Goldsmith and J. V. Bowles. POTENTIAL BENEFITS FOR PROPFAN TECHNOLOGY ON DERIVATIVES OF FUTURE SHORT- TO MEDIUM-RANGE TRANSPORT AIRCRAFT. In *AIAA/SAE/ASME 16th Joint Propulsion Conference*, pages 1–9, Hartford Connecticut, 6 1980. AIAA. doi: 10.2514/6.1980-1090.
- [80] R. Elmendorp, R. Vos, and G. La Rocca. A Conceptual Design and Analysis Method for Conventional and Unconventional Airplanes. In *ICAS 2014*, pages 1–12, St. Petersburg, 2014. Delft University of Technology.
- [81] G. La Rocca and M. J. L. Van Tooren. Enabling distributed multi-disciplinary design of complex products: a knowledge based engineering approach. *J. Design Research*, 5(3):333–352, 2007. ISSN 1748-3050.
- [82] G. La Rocca, T. H. M. Langen, and Y. H. A. Brouwers. The design and engineering engine. Towards a modular system for collaborative aircraft design. In *ICAS 2012*, 1 2012. URL <https://www.researchgate.net/publication/259266306>.
- [83] J. Van Dommelen and R. Vos. Conceptual design and analysis of blended-wing-body aircraft. *Proceedings of the Institution of Mechanical Engineers, Part G: Journal of Aerospace Engineering*, 228(13): 2452–2474, 11 2014. ISSN 20413025. doi: 10.1177/0954410013518696.
- [84] European Aviation Safety Agency. Certification Specifications for Large Aeroplanes CS-25, 9 2007.
- [85] J. Roskam. *Airplane design, Part I: Preliminary Sizing of Airplanes*. DARcorporation, Lawrence, Kansas, fourth printing edition, 2005. ISBN 9781884885426.

- [86] A. Elham, G. La Rocca, and M. J.L. Van Tooren. Development and implementation of an advanced, design-sensitive method for wing weight estimation. *Aerospace Science and Technology*, 29(1):100–113, 8 2013. ISSN 12709638. doi: 10.1016/j.ast.2013.01.012.
- [87] R. De Vries, M. T. Brown, and R. Vos. A preliminary sizing method for hybrid-electric aircraft including aero-propulsive interaction effects. In *2018 Aviation Technology, Integration, and Operations Conference*. American Institute of Aeronautics and Astronautics Inc, AIAA, 2018. ISBN 9781624105562. doi: 10.2514/6.2018-4228.
- [88] M. E.M. Hoogreef, R. de Vries, T. Sinnige, and R. Vos. Synthesis of aero-propulsive interaction studies applied to conceptual hybrid-electric aircraft design. In *AIAA Scitech 2020 Forum*, volume 1 PartF. American Institute of Aeronautics and Astronautics Inc, AIAA, 2020. ISBN 9781624105951. doi: 10.2514/6.2020-0503.
- [89] E. Torenbeek. Development and Application of a Comprehensive, Design-sensitive Weight Prediction Method for Wing Structures of Transport Category Aircraft. Technical report, Delft University of Technology, Delft, The Netherlands, 9 1992.
- [90] J. L. Felder. NASA Electric Propulsion System Studies. In *EnergyTech 2015*, Cleveland, OH, USA, 11 2015. URL www.nasa.gov.
- [91] The National Academies of Sciences. *Commercial aircraft propulsion and energy systems research: Reducing global carbon emissions*. National Academies Press, 9 2016. ISBN 0309440963. doi: 10.17226/23490.
- [92] J. Roskam. *Airplane Design Part I : Preliminary Sizing of Airplanes*. Design, Analysis and Research Corporation (DARcorporation), Lawrence, Kansas, U.S.A., sixth edition, 9 2015. ISBN 978-1884885426.
- [93] C. S. Lin, N. T. Van Dresar, and M. M. Hasan. Pressure control analysis of cryogenic storage systems. *Journal of Propulsion and Power*, 20(3):480–485, 2004. ISSN 15333876. doi: 10.2514/1.10387.
- [94] J. Huete and P. Pilidis. Parametric study on tank integration for hydrogen civil aviation propulsion. *International Journal of Hydrogen Energy*, 46(74):37049–37062, 2021. doi: 10.1016/j.ijhydene.2021.08.194.
- [95] Aspen Aerogels. Flexible Aerogel Insulation for Sub-Ambient and Cryogenic Applications, 7 2019. URL www.aerogel.com/pat.
- [96] D. Silberhorn, G. Atanasov, J Walther, and T. Zill. Assessment of Hydrogen Fuel Tank Integration at Aircraft Level. In *Deutscher Luft- und Raumfahrtkongress 2019*, Darmstadt, Deutschland, 9 2019. Deutsche Gesellschaft für Luft- und Raumfahrt. URL <https://elib.dlr.de/129643/>.
- [97] A. Filippone. *ADVANCED AIRCRAFT FLIGHT PERFORMANCE*. Cambridge University Press, first edition, 2012. ISBN 978-1-107-02400-7.
- [98] R. De Vries, M. E.M. Hoogreef, and R. Vos. Preliminary sizing of a hybrid-electric passenger aircraft featuring over-the-wing distributed-propulsion. In *AIAA Scitech 2019 Forum*. American Institute of Aeronautics and Astronautics Inc, AIAA, 2019. ISBN 9781624105784. doi: 10.2514/6.2019-1811.
- [99] J. Zamboni. A method for the conceptual design of hybrid electric aircraft. Technical report, Delft University of Technology, Delft, 2018. URL <http://repository.tudelft.nl/>.
- [100] R. De Vries. Low-speed fuselage boundary-layer ingestion in conceptual aircraft design, 11 2019.
- [101] P. Lv, D. Ragni, T. Hartuc, L. Veldhuis, and A. G. Rao. Experimental investigation of the flow mechanisms associated with a wake-ingesting propulsor. *AIAA Journal*, 55(4):1332–1342, 2017. ISSN 00011452. doi: 10.2514/1.J055292.
- [102] A. Seitz, F. Peter, J. Bijewitz, A. Habermann, Z. Goraj, M. Kowalski, A. C. Pardo, C. Hall, F. Meller, R. Merkler, O. Petit, S. Samuelsson, B. Della Corte, M. van Sluis, G. Wortmann, and M. Dietz. CONCEPT VALIDATION STUDY FOR FUSELAGE WAKE-FILLING PROPULSION INTEGRATION. In *31st Congress of the International Council of the Aeronautical Sciences*, pages 1–21, Belo Horizonte, Brazil, 9 2018. ICAS.

- [103] ESDU. *The influence of body geometry and flow conditions on axisymmetric velocity distributions at subcritical Mach numbers*, volume ESDU 78037. 1978.
- [104] ESDU. *The influence of body geometry and flow conditions on axisymmetric boundary layers at subcritical Mach numbers*, volume ESDU 79020. 1979.
- [105] W.F. Durand, M.M. Munk, K. Arnstein, W. Klemperer, E.G. Barillon, and H.L. Dryden. *Aerodynamic Theory*. Julius Springer, Berlin, 1 edition, 1935.
- [106] Airbus S.A.S. AIRBUS A321 Aircraft Characteristics Airport and Maintenance Planning. Technical report, Blagnac, France, 2005.
- [107] A. L. Byrnes, W. E. Hensleigh, and L. A. Tolve. Effect of horizontal stabilizer vertical location on the design of large transport aircraft. *Journal of Aircraft*, 3(2):97–104, 1966. ISSN 15333868. doi: 10.2514/3.43712.
- [108] A. Gomez and H. Smith. Liquid hydrogen fuel tanks for commercial aviation: Structural sizing and stress analysis. *Aerospace Science and Technology*, 95, 12 2019. ISSN 12709638. doi: 10.1016/j.ast.2019.105438.
- [109] F. Nicolosi, P. Della Vecchia, D. Ciliberti, and V. Cusati. DEVELOPMENT OF NEW PRELIMINARY DESIGN METHODOLOGIES FOR REGIONAL TURBOPROP AIRCRAFT BY CFD ANALYSES. In *29th Congress of the International Council of the Aeronautical Sciences*, St. Petersburg, Russia, 9 2014. ICAS. doi: 10.13140/2.1.5147.0721. URL www.scope.unina.it.
- [110] D. C. Mikkelson, G. A. Mitchell, and L. J. Bober. Summary of Recent NASA Propeller Research. Technical report, 1984.
- [111] P. M. Sforza. *Commercial Airplane Design Principles*. Butterworth-Heinemann, Oxford, UK, first edition, 2014. ISBN 978-0-12-419953-8.
- [112] X. Xia. *Dynamic Power Distribution Management for All Electric Aircraft* SCHOOL OF ENGINEERING. PhD thesis, Cranfield University, 2 2011.

A

Reference Aircraft XML Input File

```
1 <?xml version="1.0" encoding="utf-8"?>
2 <initiator xmlns:xsi="http://www.w3.org/2001/XMLSchema-instance" xsi:noNamespaceSchemaLocation="initiator
  .xsd">
3   <aircraft>
4     <name>A321-NEO-Reference</name>
5     <description>Airbus A321-NEO reference aircraft for APPU project</description>
6     <missions default="Harmonic">
7       <mission name="Harmonic">
8         <requirement>
9           <name>Pax</name>
10          <value>202</value>
11        </requirement>
12        <requirement>
13          <name>PayloadMass</name>
14          <value>25300</value>
15        </requirement>
16        <requirement>
17          <name>CruiseMach</name>
18          <value>0.78</value>
19        </requirement>
20        <requirement>
21          <name>Altitude</name>
22          <value>11278</value>
23        </requirement>
24        <requirement>
25          <name>Range</name>
26          <value>4630</value>
27        </requirement>
28        <requirement>
29          <name>TakeOffDistance</name>
30          <value>2330</value>
31        </requirement>
32        <requirement>
33          <name>LandingDistance</name>
34          <value>1577</value>
35        </requirement>
36        <requirement>
37          <name>ApproachSpeed</name>
38          <value>70</value>
39        </requirement>
40        <requirement>
41          <name>NumberOfFlights</name>
42          <value>100000</value>
43        </requirement>
44        <requirement>
45          <name>AirworthinessRegulations</name>
46          <value>FAR-25</value>
47        </requirement>
48        <requirement>
49          <name>TimeToClimb</name>
50          <!-- Time to climb to a specified altitude -->
51          <value mapType="vector">13.3;7300</value>
52          <!-- Time [minutes] ; Altitude [meter] -->
```

```

53     </requirement>
54     <requirement>
55       <name>LoiterTime</name>
56       <value>30</value>
57     </requirement>
58     <requirement>
59       <name>DivRange</name>
60       <value>370</value>
61     </requirement>
62     <requirement>
63       <name>AirportClassification</name>
64       <value>FAA-IV</value>
65     </requirement>
66     <requirement>
67       <name>OEICeiling</name>
68       <value>6000</value>
69     </requirement>
70   </mission>
71   <mission name="Design">
72     <requirement>
73       <name>Pax</name>
74       <value>182</value>
75     </requirement>
76     <requirement>
77       <name>PayloadMass</name>
78       <value>22700</value>
79     </requirement>
80     <requirement>
81       <name>Range</name>
82       <value>3704</value>
83     </requirement>
84     <requirement>
85       <name>CruiseMach</name>
86       <value>0.78</value>
87     </requirement>
88     <requirement>
89       <name>Altitude</name>
90       <value>11278</value>
91     </requirement>
92   </mission>
93   <mission name="Design2">
94     <requirement>
95       <name>Pax</name>
96       <value>202</value>
97     </requirement>
98     <requirement>
99       <name>PayloadMass</name>
100      <value>25300</value>
101    </requirement>
102    <requirement>
103      <name>Range</name>
104      <value>3333.6</value>
105    </requirement>
106    <requirement>
107      <name>CruiseMach</name>
108      <value>0.78</value>
109    </requirement>
110    <requirement>
111      <name>Altitude</name>
112      <value>11278</value>
113    </requirement>
114  </mission>
115 </missions>
116 <performance>
117   <parameter>
118     <name>LDmax</name>
119     <value>18</value>
120   </parameter>
121   <parameter>
122     <name>SFC</name>
123     <value>0.56</value>

```

```

124     </parameter>
125     <parameter>
126       <name>FFStartUp</name>
127       <value>0.990</value>
128     </parameter>
129     <parameter>
130       <name>FFTaxi</name>
131       <value>0.990</value>
132     </parameter>
133     <parameter>
134       <name>CLmaxLanding</name>
135       <value>3.2</value>
136     </parameter>
137     <parameter>
138       <name>CLmaxTakeOff</name>
139       <value>2.6</value>
140     </parameter>
141     <parameter>
142       <name>CLmaxClean</name>
143       <value>1.6</value>
144     </parameter>
145   </performance>
146   <configuration>
147     <parameter>
148       <name>HybridConfiguration</name>
149       <value>conventional</value>
150     </parameter>
151     <parameter>
152       <name>DistributedSpanFrac</name>
153       <value>0</value>
154     </parameter>
155     <parameter>
156       <name>DistributedChordFrac</name>
157       <value>inf</value>
158     <!-- value should agree with engine location frac later on, inf if no effect -->
159     </parameter>
160     <parameter>
161       <name>WingAspectRatio</name>
162       <value>9.5</value>
163     </parameter>
164     <parameter>
165       <name>WingLocation</name>
166       <value>Low</value>
167     </parameter>
168     <parameter>
169       <name>HasKink</name>
170       <value>1</value>
171     </parameter>
172     <parameter>
173       <name>TEinboardSweep</name>
174       <value>0</value>
175     </parameter>
176     <parameter>
177       <name>TailType</name>
178       <value>Standard</value>
179     </parameter>
180     <parameter>
181       <name>RootAirfoil</name>
182       <value>SC20414</value>
183     </parameter>
184     <parameter>
185       <name>KinkAirfoil</name>
186       <value>SC20412</value>
187     </parameter>
188     <parameter>
189       <name>KinkTwist</name>
190     <!-- twist angle at kink, code will consider wing incidence-->
191     <value>-3</value>
192     </parameter>
193     <parameter>
194       <name>TipAirfoil</name>

```

```

195     <value>SC20410</value>
196 </parameter>
197 <parameter>
198   <name>TipTwist</name>
199   <!-- twist angle at tip, code will consider wing incidence and possible kink twist-->
200   <value>-1.2</value>
201 </parameter>
202 <parameter>
203   <name>SupercriticalAirfoil</name>
204   <value>1.1</value>
205 </parameter>
206 <parameter>
207   <name>Freight</name>
208   <value>>false</value>
209 </parameter>
210 <parameter>
211   <name>FuselageTank</name>
212   <value>>false</value>
213 </parameter>
214 <parameter>
215   <name>CompositeStructures</name>
216   <!-- Fuselage,Wing,Empennage-->
217   <value mapType="vector">0;0;1</value>
218 </parameter>
219 <parameter>
220   <name>Winglets</name>
221   <value>>true</value>
222   <!-- this should be true but winglet geometry is still wrong in settings -->
223 </parameter>
224 </configuration>
225 <parts mainPart="Fuselage">
226   <fuselage name="Fuselage" type="Conventional">
227     <paxDivision mapType="vector">1</paxDivision>
228     <!-- should sum to 1 -->
229     <!-- Based on A320 Europe, Lufthansa (SeatGuru) -->
230     <!-- http://www.seatguru.com/airlines/Lufthansa/Lufthansa\_Airbus\_A320-200\_NEK.php -->
231     <!-- Dimensions: Seat width, arm rest width, seat pitch, seatbackspace, legspace (last 2 unused) -->
232     <cabins>
233       <cabin name="Cabin1">
234         <class>
235           <name>EC</name>
236           <seatingArr mapType="vector">3;3</seatingArr>
237           <seatingDim mapType="vector">0.46;0.048;0.813;0.8;0.3</seatingDim>
238         </class>
239         <classDistribution mapType="vector">0;0;0;1</classDistribution>
240       </cabin>
241     </cabins>
242   </fuselage>
243   <wing name="Main Wing" type="MainWing"/>
244   <wing name="Horizontal Stabiliser" type="HorizontalTail"/>
245   <wing name="Vertical Stabiliser" type="VerticalTail"/>
246   <engine name="Engine-1" type="TurboFan" distributed="false">
247     <location>Main Wing</location>
248     <Fuel>standard</Fuel>
249     <!-- engine x location, fraction of fuselage length for fuselage mounted; spanwise fraction for
250        wing/tail mounted, negative for other wing; -->
251     <!-- offset from wing in x fraction of engine length;offset in z fraction of engine diameter-->
252     <LocationFrac mapType="vector">0;0.32;-0.75;-0.45</LocationFrac>
253     <bypassRatio>11</bypassRatio>
254     <motor name="Turbine-1" type="Turbine"/>
255     <fan name="Fan-1" type="Fan"/>
256   </engine>
257   <engine name="Engine-2" type="TurboFan" distributed="false">
258     <location>Main Wing</location>
259     <Fuel>standard</Fuel>
260     <!-- engine x location, fraction of fuselage length for fuselage mounted; spanwise fraction for
261        wing/tail mounted, negative for other wing; -->
262     <!-- offset from wing in x fraction of engine length;offset in z fraction of engine diameter-->
263     <LocationFrac mapType="vector">0;-0.32;-0.75;-0.45</LocationFrac>
264     <bypassRatio>11</bypassRatio>

```

```

263     <motor name="Turbine-2" type="Turbine"/>
264     <fan name="Fan-2" type="Fan"/>
265   </engine>
266 </parts>
267 </aircraft>
268 <runList>DesignConvergence,ReportWriter,PlotTool</runList>
269 <settings>
270   <include source="defaultSettings.xml" priority="102"/>
271   <include source="hybridSettings.xml" priority="101"/>
272   <include source="turbopropSettings.xml" priority="101"/>
273   <setting>
274     <name>MissionDiversionMach</name>
275     <value>0.6</value>
276   </setting>
277   <setting>
278     <name>MissionDiversionAltitude</name>
279     <value>4572</value>
280   </setting>
281   <setting>
282     <name>AftMinToMaj1</name>
283     <value>0.5</value>
284   </setting>
285   <setting>
286     <name>AftMinToMaj2</name>
287     <value>1</value>
288   </setting>
289   <setting>
290     <name>FwdMinToMaj1</name>
291     <value>0.5</value>
292   </setting>
293   <setting>
294     <name>FwdMinToMaj2</name>
295     <value>0.5</value>
296   </setting>
297   <setting>
298     <name>AeroPropModel</name>
299     <value>none</value>
300     <!-- % Aero-propulsive interaction model: 'none','LEDP','OTW','BLI','LLM' -->
301   </setting>
302   <setting>
303     <name>RunHSE</name>
304     <value>1</value>
305   </setting>
306   <setting>
307     <name>missionCruiseSettings</name>
308     <!-- [xi, phi, Phi (throttle setting, supplied power ratio ,shaft power ratio)] -->
309     <value mapType="vector">0.9;0;0</value>
310     <!-- settings for hybrid class 1 sizing per mission segment -->
311   </setting>
312   <setting>
313     <name>missionLandingSettings</name>
314     <!-- [xi, phi, Phi (throttle setting, supplied power ratio ,shaft power ratio)] -->
315     <value mapType="vector">0.5;0;0</value>
316     <!-- settings for hybrid class 1 sizing per mission segment -->
317   </setting>
318   <setting>
319     <name>missionTakeoffSettings</name>
320     <!-- [xi, phi, Phi (throttle setting, supplied power ratio ,shaft power ratio)] -->
321     <value mapType="vector">1.0;0;0</value>
322     <!-- settings for hybrid class 1 sizing per mission segment -->
323   </setting>
324   <setting>
325     <name>missionBalkedLandingSettings</name>
326     <!-- [xi, phi, Phi (throttle setting, supplied power ratio ,shaft power ratio)] -->
327     <value mapType="vector">1.0;0;0</value>
328     <!-- settings for hybrid class 1 sizing per mission segment -->
329   </setting>
330   <setting>
331     <name>missionOEICeilingSettings</name>
332     <!-- [xi, phi, Phi (throttle setting, supplied power ratio ,shaft power ratio)] -->
333     <value mapType="vector">1.0;0;0</value>

```

```

334 <!-- settings for hybrid class 1 sizing per mission segment -->
335 </setting>
336 <setting>
337 <name>missionOEISecondSegmentSettings</name>
338 <!-- [xi, phi, Phi (throttle setting, supplied power ratio ,shaft power ratio)] -->
339 <value mapType="vector">1.0;0;0</value>
340 <!-- settings for hybrid class 1 sizing per mission segment -->
341 </setting>
342 <setting>
343 <name>missionOEIInitialSettings</name>
344 <!-- [xi, phi, Phi (throttle setting, supplied power ratio ,shaft power ratio)] -->
345 <value mapType="vector">1.0;0;0</value>
346 <!-- settings for hybrid class 1 sizing per mission segment -->
347 </setting>
348 <setting>
349 <name>missionOEITransitionSettings</name>
350 <!-- [xi, phi, Phi (throttle setting, supplied power ratio ,shaft power ratio)] -->
351 <value mapType="vector">1.0;0;0</value>
352 <!-- settings for hybrid class 1 sizing per mission segment -->
353 </setting>
354 <setting>
355 <name>missionROC_AEOSettings</name>
356 <!-- [xi, phi, Phi (throttle setting, supplied power ratio ,shaft power ratio)] -->
357 <value mapType="vector">1.0;0;0</value>
358 <!-- settings for hybrid class 1 sizing per mission segment -->
359 </setting>
360 <setting>
361 <name>missionAnalysisClimbSettings</name>
362 <!-- [xi [start, end], phi [start, end], Phi [start, end] (throttle setting, supplied power ratio ,
363 shaft power ratio)] -->
364 <value mapType="vector">1;1;0;0;0</value>
365 <!-- settings for hybrid class 1 sizing per mission segment -->
366 </setting>
367 <setting>
368 <name>missionAnalysisCruiseSettings</name>
369 <!-- [xi [start, end], phi [start, end], Phi [start, end] (throttle setting, supplied power ratio ,
370 shaft power ratio)] -->
371 <value mapType="vector">0.8;0.7;0;0;0</value>
372 <!-- settings for hybrid class 1 sizing per mission segment -->
373 </setting>
374 <setting>
375 <name>missionAnalysisDescentSettings</name>
376 <!-- [xi [start, end], phi [start, end], Phi [start, end] (throttle setting, supplied power ratio ,
377 shaft power ratio)] -->
378 <value mapType="vector">0.035;0.035;0;0;0</value>
379 <!-- settings for hybrid class 1 sizing per mission segment -->
380 </setting>
381 <setting>
382 <name>missionAnalysisDiversionClimbSettings</name>
383 <!-- [xi [start, end], phi [start, end], Phi [start, end] (throttle setting, supplied power ratio ,
384 shaft power ratio)] -->
385 <value mapType="vector">0.7;0.9;0;0;0</value>
386 <!-- settings for hybrid class 1 sizing per mission segment -->
387 </setting>
388 <setting>
389 <name>missionAnalysisDiversionCruiseSettings</name>
390 <!-- [xi [start, end], phi [start, end], Phi [start, end] (throttle setting, supplied power ratio ,
391 shaft power ratio)] -->
392 <value mapType="vector">0;0;0;0;0</value>
393 <!-- settings for hybrid class 1 sizing per mission segment -->
394 </setting>
395 <setting>
396 <name>missionAnalysisDiversionDescentSettings</name>
397 <!-- [xi [start, end], phi [start, end], Phi [start, end] (throttle setting, supplied power ratio ,
398 shaft power ratio)] -->
399 <value mapType="vector">0.035;0.035;0;0;0</value>
400 <!-- settings for hybrid class 1 sizing per mission segment -->
401 </setting>
402 <setting>
403 <name>missionAnalysisLoiterSettings</name>
404 <!-- [xi [start, end], phi [start, end], Phi [start, end] (throttle setting, supplied power ratio ,
405 shaft power ratio)] -->
406 <value mapType="vector">0.035;0.035;0;0;0</value>
407 <!-- settings for hybrid class 1 sizing per mission segment -->
408 </setting>

```

```

    shaft power ratio)] -->
399   <value mapType="vector">0;0;0;0</value>
400   <!-- settings for hybrid class 1 sizing per mission segment -->
401 </setting>
402 <setting>
403   <name>CruiseSettings</name>
404   <!-- [etap primary,etap secondary,thrust vectoring angle] -->
405   <value mapType="vector">0.80;0;0</value>
406   <!-- settings for hybrid class 1 sizing per mission segment -->
407 </setting>
408 <setting>
409   <name>LandingSettings</name>
410   <!-- [etap primary,etap secondary,thrust vectoring angle] -->
411   <value mapType="vector">0.52;0;0</value>
412   <!-- settings for hybrid class 1 sizing per mission segment -->
413 </setting>
414 <setting>
415   <name>DescentSettings</name>
416   <!-- [etap primary,etap secondary,thrust vectoring angle] -->
417   <value mapType="vector">0.52;0;0</value>
418   <!-- settings for hybrid class 1 sizing per mission segment -->
419 </setting>
420 <setting>
421   <name>TakeoffSettings</name>
422   <!-- [etap primary,etap secondary,thrust vectoring angle] -->
423   <value mapType="vector">0.53;0;0</value>
424   <!-- settings for hybrid class 1 sizing per mission segment -->
425 </setting>
426 <setting>
427   <name>BalkedLandingSettings</name>
428   <!-- [etap primary,etap secondary,thrust vectoring angle] -->
429   <value mapType="vector">0.67;0;0</value>
430   <!-- settings for hybrid class 1 sizing per mission segment -->
431 </setting>
432 <setting>
433   <name>OEICeilingSettings</name>
434   <!-- [etap primary,etap secondary,thrust vectoring angle] -->
435   <value mapType="vector">0.76;0;0</value>
436   <!-- settings for hybrid class 1 sizing per mission segment -->
437 </setting>
438 <setting>
439   <name>OEISecondSegmentSettings</name>
440   <!-- [etap primary,etap secondary,thrust vectoring angle] -->
441   <value mapType="vector">0.64;0;0</value>
442   <!-- settings for hybrid class 1 sizing per mission segment -->
443 </setting>
444 <setting>
445   <name>AEOCeilingSettings</name>
446   <!-- [etap primary,etap secondary,thrust vectoring angle] -->
447   <value mapType="vector">0.61;0;0</value>
448   <!-- settings for hybrid class 1 sizing per mission segment -->
449 </setting>
450 <setting>
451   <name>ROC_AEOSettings</name>
452   <!-- [etap primary,etap secondary,thrust vectoring angle] -->
453   <value mapType="vector">0.61;0;0</value>
454   <!-- settings for hybrid class 1 sizing per mission segment -->
455 </setting>
456 <setting>
457   <name>ROC_OEISettings</name>
458   <!-- [etap primary,etap secondary,thrust vectoring angle] -->
459   <value mapType="vector">0.61;0;0</value>
460   <!-- settings for hybrid class 1 sizing per mission segment -->
461 </setting>
462 <setting>
463   <name>ClimbSettings</name>
464   <!-- [etap primary,etap secondary,thrust vectoring angle] -->
465   <value mapType="vector">0.76;0;0</value>
466   <!-- settings for hybrid class 1 sizing per mission segment -->
467 </setting>
468 <setting>

```

```

469     <name>EnRoute_OEI_Gradient_Settings</name>
470     <!-- [etap primary,etap secondary,thrust vectoring angle] -->
471     <value mapType="vector">0.8;0;0</value>
472     <!-- settings for hybrid class 1 sizing per mission segment -->
473 </setting>
474 <setting>
475     <name>Transition_OEI_Gradient_Settings</name>
476     <!-- [etap primary,etap secondary,thrust vectoring angle] -->
477     <value mapType="vector">0.67;0;0</value>
478     <!-- settings for hybrid class 1 sizing per mission segment -->
479 </setting>
480 <setting>
481     <name>Initial_OEI_Gradient_Settings</name>
482     <!-- [etap primary,etap secondary,thrust vectoring angle] -->
483     <value mapType="vector">0.64;0;0</value>
484     <!-- settings for hybrid class 1 sizing per mission segment -->
485 </setting>
486 <setting>
487     <name>EnergyFractionTaxiOut</name>
488     <value>0.01</value>
489 </setting>
490 <setting>
491     <name>EnergyFractionTakeOff</name>
492     <value>0.02</value>
493 </setting>
494 <setting>
495     <name>EnergyFractionLanding</name>
496     <value>0.015</value>
497 </setting>
498 <setting>
499     <name>EnergyFractionTaxiIn</name>
500     <value>0.01</value>
501 </setting>
502 <setting>
503     <name>suppliedPowerTakeOff</name>
504     <value>0</value>
505     <!-- [-] -->
506 </setting>
507 <setting>
508     <name>MissionDiversionMach</name>
509     <value>0.65</value>
510 </setting>
511 <setting>
512     <name>suppliedPowerLanding</name>
513     <value>0</value>
514     <!-- [-] -->
515 </setting>
516 <setting>
517     <name>ComputeEtap</name>
518     <value>0 </value>
519     <!-- [-] -->
520 </setting>
521 <setting>
522     <name>ComputeEtaGt</name>
523     <value>1</value>
524 </setting>
525 <setting>
526     <name>GTPowerDensity</name>
527     <value>0.75</value>
528 </setting>
529 <setting>
530     <name>EtaGTScale</name>
531     <value>1.05</value>
532 </setting>
533 <setting>
534     <name>MaxLandingMassRatio</name>
535     <value>0.84</value>
536 </setting>
537 <setting>
538     <name>LuggageMass</name>
539     <!-- Luggage Mass per Passenger - ACAPS are for 95kg per PAX!-->

```

```

540     <value>18</value>
541     <!-- [kg] -->
542 </setting>
543 <!-- Wing design settings -->
544 <setting>
545     <name>SparPositions</name>
546     <value mapType="vector">0.10;0.6</value>
547 </setting>
548 <setting>
549     <name>UseAuxiliarySparForFuelTank</name>
550     <value>false</value>
551 </setting>
552 <setting>
553     <name>UsableFuelVolume</name>
554     <!-- Fraction of fuel tank volume usable for fuel storage -->
555     <value>1</value>
556 </setting>
557 <!-- HT and VT design settings -->
558 <setting>
559     <name>VerticalTailVolumeCoefficient</name>
560     <value>0.115</value>
561 </setting>
562 <setting>
563     <name>VerticalTailAspectRatio</name>
564     <value>1.6</value>
565 </setting>
566 <setting>
567     <name>VerticalTailTaper</name>
568     <value>0.34</value>
569 </setting>
570 <setting>
571     <name>HTVerticalOffset</name>
572     <!-- Shift if negative Z-direction of the HT from the root of the VT
573     as a fraction of fuselage diameter. Only for standard tail types.
574     (defined in positionHorizontalTail.m)-->
575     <value>0.2</value>
576 </setting>
577 <setting>
578     <name>HorizontalTailVolumeCoefficient</name>
579     <value>1.0</value>
580 </setting>
581 <setting>
582     <name>HorizontalTailAspectRatio</name>
583     <value>5</value>
584 </setting>
585 <setting>
586     <name>HorizontalTailTaper</name>
587     <value>0.37</value>
588 </setting>
589 <setting>
590     <name>TailControl</name>
591     <value>full moving</value>
592 </setting>
593 <!-- Class 2.5 settings -->
594 <setting>
595     <name>runWingClass25</name>
596     <value>true</value>
597 </setting>
598 <setting>
599     <name>runFuselageClass25</name>
600     <value>false</value>
601 </setting>
602 <setting>
603     <name>UseFemWingWeight</name>
604     <value>true</value>
605 </setting>
606 <setting>
607     <name>FemWingWeightCorrectionFactor</name>
608     <value>1.35</value>
609     <!-- composite structures! -->
610 </setting>

```

```

611 <!-- Fuselage design settings -->
612 <setting>
613   <name>FuselageFractions</name>
614   <value mapType="vector">0;0.1;0.82;1</value>
615 </setting>
616 <setting>
617   <name>NLF</name>
618   <!-- Nose (cockpit) length to nosecone length -->
619   <value>0.6</value>
620   <!-- [-] -->
621 </setting>
622 <setting>
623   <name>fixNL</name>
624   <value>>false</value>
625 </setting>
626 <setting>
627   <name>TLF</name>
628   <!-- Tail length to tailcone length -->
629   <value>0.7</value>
630   <!-- [-] -->
631 </setting>
632 <setting>
633   <name>DefaultNoseShapeFactor</name>
634   <!-- Fraction of fuselage diameter for nose shaping -->
635   <value>1.3</value>
636 </setting>
637 <setting>
638   <name>DefaultTailShapeFactor</name>
639   <!-- Fraction of fuselage diameter for tail shaping -->
640   <value>2.2</value>
641 </setting>
642 <setting>
643   <name>DefaultAftRatioHeight</name>
644   <!-- Fraction of diameter for width of tail tip -->
645   <value>0.18</value>
646 </setting>
647 <setting>
648   <name>DefaultAftRatioWidth</name>
649   <value>0.18</value>
650 </setting>
651 <setting>
652   <name>ScrapeAngleLOF</name>
653   <value>12</value>
654 </setting>
655 <!-- Winglet settings -->
656 <setting>
657   <name>WingletAspectRatio</name>
658   <value>2.2</value>
659 </setting>
660 <setting>
661   <name>WingletTaper</name>
662   <value>0.28</value>
663 </setting>
664 <setting>
665   <name>WingletAngle</name>
666   <value>85</value>
667 </setting>
668 <setting>
669   <name>WingletToeInAngle</name>
670   <value>0</value>
671 </setting>
672 <setting>
673   <name>WingletTwist</name>
674   <value>0</value>
675 </setting>
676 <!-- end of settings -->
677 </settings>
678 <moduleInputs>
679   <input module="PlotTool">
680     <plotModules>Geometry,DesignConvergence</plotModules>
681   </input>

```

```
682 </moduleInputs>  
683 </initiator>
```

Code/A321-NEO-Reference.xml

B

A321appu XML Input File

```
1 <?xml version="1.0" encoding="utf-8"?>
2 <initiator xmlns:xsi="http://www.w3.org/2001/XMLSchema-instance" xsi:noNamespaceSchemaLocation="initiator
3   .xsd">
4   <aircraft>
5     <name>A321-appu</name>
6     <description>Airbus A321-appu input file</description>
7     <missions default="Harmonic">
8       <mission name="Harmonic">
9         <requirement>
10          <name>Pax</name>
11          <value>202</value>
12        </requirement>
13        <requirement>
14          <name>PayloadMass</name>
15          <value>25300</value>
16        </requirement>
17        <requirement>
18          <name>CruiseMach</name>
19          <value>0.78</value>
20        </requirement>
21        <requirement>
22          <name>Altitude</name>
23          <value>11278</value>
24        </requirement>
25        <requirement>
26          <name>Range</name>
27          <value>4630</value>
28        </requirement>
29        <requirement>
30          <name>TakeOffDistance</name>
31          <value>2330</value>
32        </requirement>
33        <requirement>
34          <name>LandingDistance</name>
35          <value>1577</value>
36        </requirement>
37        <requirement>
38          <name>ApproachSpeed</name>
39          <value>70</value>
40        </requirement>
41        <requirement>
42          <name>NumberOfFlights</name>
43          <value>100000</value>
44        </requirement>
45        <requirement>
46          <name>AirworthinessRegulations</name>
47          <value>FAR-25</value>
48        </requirement>
49        <requirement>
50          <name>TimeToClimb</name>
51          <!-- Time to climb to a specified altitude -->
52          <value mapType="vector">13.3;7300</value>
53          <!-- Time [minutes] ; Altitude [meter] -->
```

```
53     </requirement>
54     <requirement>
55       <name>LoiterTime</name>
56       <value>30</value>
57     </requirement>
58     <requirement>
59       <name>DivRange</name>
60       <value>370</value>
61     </requirement>
62     <requirement>
63       <name>AirportClassification</name>
64       <value>FAA-IV</value>
65     </requirement>
66     <requirement>
67       <name>OEICeiling</name>
68       <value>6000</value>
69     </requirement>
70   </mission>
71 </missions>
72 <performance>
73   <parameter>
74     <name>LDmax</name>
75     <value>18</value>
76   </parameter>
77   <parameter>
78     <name>SFC</name>
79     <value>0.56</value>
80   </parameter>
81   <parameter>
82     <name>CLmaxLanding</name>
83     <value>3.2</value>
84   </parameter>
85   <parameter>
86     <name>CLmaxTakeOff</name>
87     <value>2.6</value>
88   </parameter>
89   <parameter>
90     <name>CLmaxClean</name>
91     <value>1.6</value>
92   </parameter>
93   <parameter>
94     <name>FuelType</name>
95     <value>standard</value>
96   </parameter>
97   <parameter>
98     <name>FuelType2</name>
99     <value>LH2</value>
100  </parameter>
101  <parameter>
102    <name>Fuel2SE</name>
103    <value>120000000</value>
104  </parameter>
105  <parameter>
106    <name>Fuel2Density</name>
107    <value>71</value>
108  </parameter>
109  <parameter>
110    <name>FFStartUp</name>
111    <value>0.990</value>
112  </parameter>
113  <parameter>
114    <name>FFTaxi</name>
115    <value>0.990</value>
116  </parameter>
117 </performance>
118 <configuration>
119   <parameter>
120     <name>WingAspectRatio</name>
121     <value>9.5</value>
122   </parameter>
123   <parameter>
```

```

124     <name>WingLocation</name>
125     <value>Low</value>
126 </parameter>
127 <parameter>
128     <name>HasKink</name>
129     <value>1</value>
130 </parameter>
131 <parameter>
132     <name>TEinboardSweep</name>
133     <value>0</value>
134 </parameter>
135 <parameter>
136     <name>TailType</name>
137     <value>Cruciform</value>
138 </parameter>
139 <parameter>
140     <name>RootAirfoil</name>
141     <value>SC20414</value>
142 </parameter>
143 <parameter>
144     <name>KinkAirfoil</name>
145     <value>SC20412</value>
146 </parameter>
147 <parameter>
148     <name>KinkTwist</name>
149     <!-- twist angle at kink, code will consider wing incidence-->
150     <value>-3</value>
151 </parameter>
152 <parameter>
153     <name>TipAirfoil</name>
154     <value>SC20410</value>
155 </parameter>
156 <parameter>
157     <name>TipTwist</name>
158     <!-- twist angle at tip, code will consider wing incidence and possible kink twist-->
159     <value>-1.2</value>
160 </parameter>
161 <parameter>
162     <name>SupercriticalAirfoil</name>
163     <value>1.1</value>
164 </parameter>
165 <parameter>
166     <name>Freight</name>
167     <value>>false</value>
168 </parameter>
169 <parameter>
170     <name>FuselageTank</name>
171     <value>>false</value>
172 </parameter>
173 <parameter>
174     <name>CompositeStructures</name>
175     <!-- Fuselage,Wing,Empennage-->
176     <value mapType="vector">0;0;1</value>
177 </parameter>
178 <parameter>
179     <name>HybridConfiguration</name>
180     <value>dual-fuel</value>
181 </parameter>
182 <parameter>
183     <name>DistributedSpanFrac</name>
184     <value>0.1</value>
185 </parameter>
186 <parameter>
187     <name>DistributedChordFrac</name>
188     <value>inf</value>
189 </parameter>
190 <parameter>
191     <name>TankLayout</name>
192     <value>aft</value>
193 </parameter>
194 <parameter>

```

```

195     <name>SphericalTank</name>
196     <value>>false</value>
197 </parameter>
198 <parameter>
199     <name>IntegralTank</name>
200     <value>>false</value>
201 </parameter>
202 <parameter>
203     <name>Winglets</name>
204     <value>>true</value>
205     <!-- this should be true but winglet geometry is still wrong in settings -->
206 </parameter>
207 </configuration>
208 <parts mainPart="Fuselage">
209     <fuselage name="Fuselage" type="Conventional">
210         <paxDivision mapType="vector">1</paxDivision>
211         <!-- should sum to 1 -->
212         <!-- Based on A320 Europe, Lufthansa (SeatGuru) -->
213         <!-- http://www.seatguru.com/airlines/Lufthansa/Lufthansa_Airbus_A320-200_NEK.php -->
214         <!-- Dimensions: Seat width, arm rest width, seat pitch, seatbackspace, legspace (last 2 unused)
                -->
215         <cabins>
216             <cabin name="Cabin1">
217                 <class>
218                     <name>EC</name>
219                     <seatingArr mapType="vector">3;3</seatingArr>
220                     <seatingDim mapType="vector">0.46;0.048;0.813;0.8;0.3</seatingDim>
221                 </class>
222                 <classDistribution mapType="vector">0;0;0;1</classDistribution>
223             </cabin>
224         </cabins>
225     </fuselage>
226     <wing name="Main Wing" type="MainWing"/>
227     <wing name="Horizontal Stabiliser" type="HorizontalTail"/>
228     <wing name="Vertical Stabiliser" type="VerticalTail"/>
229     <engine name="Engine-1" type="TurboFan" distributed="false">
230         <location>Main Wing</location>
231         <Fuel>standard</Fuel>
232         <!-- engine x location, fraction of fuselage length for fuselage mounted; spanwise fraction for
                wing/tail mounted, negative for other wing; -->
233         <!-- offset from wing in x fraction of engine length;offset in z fraction of engine diameter-->
234         <LocationFracs mapType="vector">0;0.32;-0.75;-0.45</LocationFracs>
235         <bypassRatio>11</bypassRatio>
236         <motor name="Turbine-1" type="Turbine"/>
237         <fan name="Fan-1" type="Fan"/>
238     </engine>
239     <engine name="Engine-2" type="TurboFan" distributed="false">
240         <location>Main Wing</location>
241         <Fuel>standard</Fuel>
242         <!-- engine x location, fraction of fuselage length for fuselage mounted; spanwise fraction for
                wing/tail mounted, negative for other wing; -->
243         <!-- offset from wing in x fraction of engine length;offset in z fraction of engine diameter-->
244         <LocationFracs mapType="vector">0;-0.32;-0.75;-0.45</LocationFracs>
245         <bypassRatio>11</bypassRatio>
246         <motor name="Turbine-2" type="Turbine"/>
247         <fan name="Fan-2" type="Fan"/>
248     </engine>
249     <engine name="Engine-3" type="TurboProp" distributed="true">
250         <location>Fuselage</location>
251         <Fuel>LH2</Fuel>
252         <LocationFracs mapType="vector">0.99;0;0;0</LocationFracs>
253         <motor name="Turbine-3" type="Turbine">
254             <RPM>1200</RPM>
255         </motor>
256         <fan name="Prop-3" type="Propeller">
257             <bladeName>F568</bladeName>
258             <NoBlades>10</NoBlades>
259             <RPM>850</RPM>
260         </fan>
261     </engine>
262     <tank name="AftTank" type="aft">

```

```

263     <location>Fuselage</location>
264 </tank>
265 <tank name="FwdTank" type="fwd">
266     <location>Fuselage</location>
267 </tank>
268 </parts>
269 </aircraft>
270 <runList>DesignConvergence,ReportWriter,PlotTool</runList>
271 <settings>
272 <include source="defaultSettings.xml" priority="102"/>
273 <include source="turbopropSettings.xml" priority="101"/>
274 <include source="hybridSettings.xml" priority="101"/>
275 <setting>
276 <name>MissionDiversioMach</name>
277 <value>0.6</value>
278 </setting>
279 <setting>
280 <name>MissionDiversioAltitude</name>
281 <value>4572</value>
282 </setting>
283 <setting>
284 <!-- Based on Gomez and Smith 2019 -->
285 <name>AftMinToMaj1</name>
286 <value>0.6</value>
287 </setting>
288 <setting>
289 <name>AftMinToMaj2</name>
290 <!-- Based on Gomez and Smith 2019 -->
291 <value>0.6</value>
292 </setting>
293 <setting>
294 <name>FwdMinToMaj1</name>
295 <value>0.5</value>
296 </setting>
297 <setting>
298 <name>FwdMinToMaj2</name>
299 <value>0.5</value>
300 </setting>
301 <setting>
302 <name>AeroPropModel</name>
303 <value>BLI</value>
304 </setting>
305 <setting>
306 <name>RunHSE</name>
307 <value>1</value>
308 </setting>
309 <setting>
310 <name>missionCruiseSettings</name>
311 <!-- [xi, phi, Phi (throttle setting, supplied power ratio ,shaft power ratio)] -->
312 <value mapType="vector">0.9;NaN;0.1</value>
313 <!-- settings for hybrid class 1 sizing per mission segment -->
314 </setting>
315 <setting>
316 <name>missionLandingSettings</name>
317 <!-- [xi, phi, Phi (throttle setting, supplied power ratio ,shaft power ratio)] -->
318 <value mapType="vector">0.5;NaN;0.1</value>
319 <!-- settings for hybrid class 1 sizing per mission segment -->
320 </setting>
321 <setting>
322 <name>missionTakeoffSettings</name>
323 <!-- [xi, phi, Phi (throttle setting, supplied power ratio ,shaft power ratio)] -->
324 <value mapType="vector">1.0;NaN;0.1</value>
325 <!-- settings for hybrid class 1 sizing per mission segment -->
326 </setting>
327 <setting>
328 <name>missionBalkedLandingSettings</name>
329 <!-- [xi, phi, Phi (throttle setting, supplied power ratio ,shaft power ratio)] -->
330 <value mapType="vector">1.0;NaN;0.1</value>
331 <!-- settings for hybrid class 1 sizing per mission segment -->
332 </setting>
333 <setting>

```

```

334     <name>missionOEICeilingSettings</name>
335     <!-- [xi, phi, Phi (throttle setting, supplied power ratio ,shaft power ratio)] -->
336     <value mapType="vector">1.0;NaN;0.1</value>
337     <!-- settings for hybrid class 1 sizing per mission segment -->
338 </setting>
339 <setting>
340     <name>missionOEISecondSegmentSettings</name>
341     <!-- [xi, phi, Phi (throttle setting, supplied power ratio ,shaft power ratio)] -->
342     <value mapType="vector">1.0;NaN;0.1</value>
343     <!-- settings for hybrid class 1 sizing per mission segment -->
344 </setting>
345 <setting>
346     <name>missionOEIInitialSettings</name>
347     <!-- [xi, phi, Phi (throttle setting, supplied power ratio ,shaft power ratio)] -->
348     <value mapType="vector">1.0;NaN;0.1</value>
349     <!-- settings for hybrid class 1 sizing per mission segment -->
350 </setting>
351 <setting>
352     <name>missionOEITransitionSettings</name>
353     <!-- [xi, phi, Phi (throttle setting, supplied power ratio ,shaft power ratio)] -->
354     <value mapType="vector">1.0;NaN;0.1</value>
355     <!-- settings for hybrid class 1 sizing per mission segment -->
356 </setting>
357 <setting>
358     <name>missionROC_AEOSettings</name>
359     <!-- [xi, phi, Phi (throttle setting, supplied power ratio ,shaft power ratio)] -->
360     <value mapType="vector">1.0;NaN;0.1</value>
361     <!-- settings for hybrid class 1 sizing per mission segment -->
362 </setting>
363 <setting>
364     <name>missionAnalysisClimbSettings</name>
365     <!-- [xi [start, end], phi [start, end], Phi [start, end] (throttle setting, supplied power ratio ,
366         shaft power ratio)] -->
367     <value mapType="vector">1;1;NaN;NaN;0.1;0.1</value>
368     <!-- settings for hybrid class 1 sizing per mission segment -->
369 </setting>
370 <setting>
371     <name>missionAnalysisCruiseSettings</name>
372     <!-- [xi [start, end], phi [start, end], Phi [start, end] (throttle setting, supplied power ratio ,
373         shaft power ratio)] -->
374     <value mapType="vector">NaN;NaN;NaN;NaN;0.1;0.1</value>
375     <!-- settings for hybrid class 1 sizing per mission segment -->
376 </setting>
377 <setting>
378     <name>missionAnalysisDescentSettings</name>
379     <!-- [xi [start, end], phi [start, end], Phi [start, end] (throttle setting, supplied power ratio ,
380         shaft power ratio)] -->
381     <value mapType="vector">0.035;0.035;NaN;NaN;0.1;0.1</value>
382     <!-- settings for hybrid class 1 sizing per mission segment -->
383 </setting>
384 <setting>
385     <name>missionAnalysisDiversionClimbSettings</name>
386     <!-- [xi [start, end], phi [start, end], Phi [start, end] (throttle setting, supplied power ratio ,
387         shaft power ratio)] -->
388     <value mapType="vector">0.7;0.9;NaN;NaN;0.1;0.1</value>
389     <!-- settings for hybrid class 1 sizing per mission segment -->
390 </setting>
391 <setting>
392     <name>missionAnalysisDiversionCruiseSettings</name>
393     <!-- [xi [start, end], phi [start, end], Phi [start, end] (throttle setting, supplied power ratio ,
394         shaft power ratio)] -->
395     <value mapType="vector">NaN;NaN;NaN;NaN;0.1;0.1</value>
396     <!-- settings for hybrid class 1 sizing per mission segment -->
397 </setting>
398 <setting>
399     <name>missionAnalysisDiversionDescentSettings</name>
400     <!-- [xi [start, end], phi [start, end], Phi [start, end] (throttle setting, supplied power ratio ,
401         shaft power ratio)] -->
402     <value mapType="vector">0.035;0.035;NaN;NaN;0.1;0.1</value>
403     <!-- settings for hybrid class 1 sizing per mission segment -->
404 </setting>

```

```

399 <setting>
400 <name>missionAnalysisLoiterSettings</name>
401 <!-- [xi [start, end], phi [start, end], Phi [start, end] (throttle setting, supplied power ratio ,
      shaft power ratio)] -->
402 <value mapType="vector">NaN;NaN;NaN;NaN;0.1;0.1</value>
403 <!-- settings for hybrid class 1 sizing per mission segment -->
404 </setting>
405 <setting>
406 <name>EnergyFractionTaxiOut</name>
407 <value>0.01</value>
408 </setting>
409 <setting>
410 <name>EnergyFractionTakeOff</name>
411 <value>0.02</value>
412 </setting>
413 <setting>
414 <name>EnergyFractionLanding</name>
415 <value>0.015</value>
416 </setting>
417 <setting>
418 <name>EnergyFractionTaxiIn</name>
419 <value>0.01</value>
420 </setting>
421 <setting>
422 <name>suppliedPowerTakeOff</name>
423 <value>0.1</value>
424 <!-- [-] -->
425 </setting>
426 <setting>
427 <name>MissionDiversionMach</name>
428 <value>0.65</value>
429 </setting>
430 <setting>
431 <name>suppliedPowerLanding</name>
432 <value>0.1</value>
433 <!-- [-] -->
434 </setting>
435 <setting>
436 <name>ElectricTaxi</name>
437 <value>0.1</value>
438 </setting>
439 <setting>
440 <name>ComputeEtap</name>
441 <value>1</value>
442 <!-- [-] -->
443 </setting>
444 <setting>
445 <name>AeroPropEffectPropulsionSystem</name>
446 <value>2</value>
447 </setting>
448 <setting>
449 <name>GTpowerDensity</name>
450 <value>0.75</value>
451 </setting>
452 <setting>
453 <name>ComputeEtaGt</name>
454 <value>1</value>
455 </setting>
456 <setting>
457 <name>EtaGTScale</name>
458 <value>1.05</value>
459 </setting>
460 <setting>
461 <name>SparPositions</name>
462 <value mapType="vector">0.10;0.6</value>
463 </setting>
464 <setting>
465 <name>LuggageMass</name>
466 <!-- Luggage Mass per Passenger - ACAPS are for 95kg per PAX!-->
467 <value>18</value>
468 <!-- [kg] -->

```

```

469 </setting>
470 <setting>
471   <name>UseAuxiliarySparForFuelTank</name>
472   <value>>false</value>
473 </setting>
474 <setting>
475   <name>MaxLandingMassRatio</name>
476   <value>0.84</value>
477 </setting>
478 <setting>
479   <name>UseFemWingWeight</name>
480   <value>>true</value>
481 </setting>
482 <setting>
483   <name>FemWingWeightCorrectionFactor</name>
484   <value>1.35</value>
485   <!-- composite structures! -->
486 </setting>
487 <setting>
488   <name>FuselageFractions</name>
489   <value mapType="vector">0;0.1;0.82;1</value>
490 </setting>
491 <setting>
492   <name>UsableFuelVolume</name>
493   <!-- Fraction of fuel tank volume usable for fuel storage -->
494   <value>1.0</value>
495 </setting>
496 <setting>
497   <name>ventingPressure</name>
498   <!-- venting pressure of the LH2 tank [Pa] -->
499   <value>250000</value>
500 </setting>
501 <setting>
502   <name>fuelFracAft</name>
503   <!-- Fraction of LH2 stored in the aft tank in case of a fwd and aft tank configuration -->
504   <value>1</value>
505 </setting>
506 <setting>
507   <name>thermalCond</name>
508   <!-- Thermal conductivity of the LH2 tank insulation material [W/mK] per meter of thickness -->
509   <value>0.01</value>
510 </setting>
511 <setting>
512   <name>sigmainnershell</name>
513   <!-- Young's modulus of the LH2 tank inner wall material -->
514   <value>172E6</value>
515 </setting>
516 <setting>
517   <name>directVenting</name>
518   <!-- mass flow rate of direct gas venting in flight phases [kg/s] (from gate2 backward) -->
519   <value mapType="vector">0;0;0;0;0;0</value>
520   <!-- [Pa] -->
521 </setting>
522 <setting>
523   <name>HybridSystems</name>
524   <!-- This removes the APU and reduces the weight of the controls because they can be electrified.
525       For further explanation, see getFixedEquipmentWeight.m line 230-->
526   <value>>false</value>
527 </setting>
528 <setting>
529   <name>deltaTISA</name>
530   <!-- temperature offset to standard atmospheric temperature (The maximum MIL 210 hot day temperature
531       is 312.6 K (39.5 deg C) at sea level.) -->
532   <value>24.5</value>
533   <!-- [K] -->
534 </setting>
535 <setting>
536   <name>deltatambground</name>
537   <!-- temperature offset to standard atmospheric temperature -->
538   <value>20</value>
539   <!-- [K] -->

```

```

538 </setting>
539 <setting>
540   <name>forceAftTankBehindPressureBulkhead</name>
541   <!-- place aft tank aft of the aft pressure bulkhead (used by APPU Project) -->
542   <value>true</value>
543   <!-- [-] -->
544 </setting>
545 <setting>
546   <name>cabinendsAllowance</name>
547   <!-- space to be left for firewall between cabin and tanks -->
548   <value>0.1</value>
549   <!-- [m] -->
550 </setting>
551 <setting>
552   <name>VerticalTailVolumeCoefficient</name>
553   <value>0.115</value>
554 </setting>
555 <setting>
556   <name>VerticalTailAspectRatio</name>
557   <value>1.6</value>
558 </setting>
559 <setting>
560   <name>VerticalTailTaper</name>
561   <value>0.34</value>
562 </setting>
563 <setting>
564   <name>HTailVTailFraction</name>
565   <!-- MainPart fraction -->
566   <value>0.3</value>
567   <!-- height of cruciform horizontal tail -->
568 </setting>
569 <setting>
570   <name>HorizontalTailVolumeCoefficient</name>
571   <value>1.0</value>
572 </setting>
573 <setting>
574   <name>HorizontalTailAspectRatio</name>
575   <value>5</value>
576 </setting>
577 <setting>
578   <name>HorizontalTailTaper</name>
579   <value>0.37</value>
580 </setting>
581 <setting>
582   <name>HTdihedral</name>
583   <value>-4</value>
584 </setting>
585 <setting>
586   <name>NLF</name>
587   <!-- Nose (cockpit) length to nosecone length -->
588   <value>0.6</value>
589   <!-- [-] -->
590 </setting>
591 <setting>
592   <name>fixNL</name>
593   <value>false</value>
594 </setting>
595 <setting>
596   <name>runWingClass25</name>
597   <value>true</value>
598 </setting>
599 <setting>
600   <name>runFuselageClass25</name>
601   <value>false</value>
602 </setting>
603 <setting>
604   <name>TLF</name>
605   <!-- Tail length to tailcone length -->
606   <value>0.7</value>
607   <!-- [-] -->
608 </setting>

```

```

609 <setting>
610 <name>DefaultNoseShapeFactor</name>
611 <!-- Fraction of fuselage diameter for nose shaping -->
612 <value>1.3</value>
613 </setting>
614 <setting>
615 <name>DefaultTailShapeFactor</name>
616 <!-- Fraction of fuselage diameter for tail shaping -->
617 <value>2.2</value>
618 </setting>
619 <setting>
620 <name>DefaultAftRatioHeight</name>
621 <!-- Fraction of diameter for width of tail tip -->
622 <value>0.18</value>
623 </setting>
624 <setting>
625 <name>DefaultAftRatioWidth</name>
626 <value>0.18</value>
627 </setting>
628 <!-- Winglet settings -->
629 <setting>
630 <name>WingletAspectRatio</name>
631 <value>2.2</value>
632 </setting>
633 <setting>
634 <name>WingletTaper</name>
635 <value>0.28</value>
636 </setting>
637 <setting>
638 <name>WingletAngle</name>
639 <value>85</value>
640 </setting>
641 <setting>
642 <name>WingletToeInAngle</name>
643 <value>0</value>
644 </setting>
645 <setting>
646 <name>WingletTwist</name>
647 <value>0</value>
648 </setting>
649 <setting>
650 <name>RemoveAPU</name>
651 <value>true</value>
652 </setting>
653 <setting>
654 <name>ScrapeAngleLOF</name>
655 <value>12</value>
656 </setting>
657 <!-- end of settings -->
658 </settings>
659 <moduleInputs>
660 <input module="PlotTool">
661 <plotModules>Geometry,DesignConvergence</plotModules>
662 </input>
663 </moduleInputs>
664 </initiator>

```

Code/A321-appu.xml